Doctoral Dissertation

Colloid Chemical Approach to Fabricate Nanostructured Cu-Fe-S Thermoelectric Materials

Maninder Singh

Supervisor: Professor Shinya Maenosono

School of Materials Science

Japan Advanced Institute of Science and Technology

March, 2019

Abstract

The research reported in this dissertation work is focused on the synthesis and characterization of the sustainable thermoelectric materials consisting of elements such as copper, iron and sulfur. These elements are earth abundant, less toxic, and inexpensive and acts as building blocks for the fabrication of copper sulfide, iron sulfide, and Cu-Fe-S nanobulk materials for thermoelectric use. These nanoparticles are fabricated using bottom-up/ wet chemical approach which offers the most versatility in terms of control over size, shape, composition and structure of the nanoparticles. Moreover, the bottom-up synthetic technique can be adequately scaled up to create large amount of nanoparticles or nanobulk material for the subsequent thermoelectric measurement. Research work presented in the thesis is based on the synthesis and characterization of chalcogenide, and Cu-Fe-S nanobulk thermoelectric materials.

In chapter 1, I have described background and information about thermoelectricity and choice of thermoelectric materials. A brief review of current status of various thermoelectric materials is given. Research objective will provide the brief information of the work done in this dissertation.

In chapter 2, I have discussed the fabrication of copper iron sulfide nanoparticles by a bottom-up chemical approach. Varying amounts of copper and iron were used to synthesize copper iron sulfide nanoparticles and these nanoparticles with varying composition of copper and iron were fabricated into nanobulk pellet by cold pressed method without applying any special techniques such as pulsed electric current sintering or thermal treatment. Subesquently, their thermoelectric properties were mapped as a function of composition at room temperature and it was observed that on increasing iron content, the power factor decreased. The Seebeck coefficient of the materials reveals p-type conductivity with a maximum value of 203 μV/K at room temperature for Cu/Fe (mol % =30:70).

Chapter 3, I have discussed the fabrication of sustainable Cu-Fe-S nanobulk system for thermoelectrics using Cu_2S and FeS nanoparticles as building blocks. Bottom-up/ wet chemical approach was followed to synthesize Cu_2S and FeS nanoparticles. Varying volume fraction of Cu_2S and FeS nanoparticles were used to obtain different crystal structure of Cu-Fe-S nanobulk material with readily tunable p- to n- type conductivity. Nanobulk material leads to low lattice thermal conductivity ranging from 0.3 to 1.0 $W\ m^{-1}\ K^{-1}$. Blend of 9:1 volume fraction of Cu_2S and FeS NPs gave nanocomposite consisting of bornite Cu_5FeS_4 as the main phase and other minor phases, including nukundamite, digenite, roxbyite, and CuO. This nanocomposite has a maximum dimensionless figure

of merit (*ZT*) of 0.55 at 663 K, which is 45% higher than that of pristine bornite Cu_5FeS_4 because of the enhanced power factor and low lattice thermal conductivity (κ_{lat}, 0.3 W m^{-1} K^{-1}).

Chapter 4 describes the structural and thermoelectric property relationship of different Cu-Fe-S system and chapter 5 gives overall general conclusion, and future prospects of the presented research.

Keywords: Thermoelectric, Colloid Chemical Method, Nanoparticles, Sulfides, Sustainable

Acknowledgements

I find immense pleasure in thanking all those people without whom this thesis could not be completed. First, I would like to thank my supervisor Prof. Shinya Maenosono to supervise my research. His constant encouragement, guidance and immense support in finding direction to my research theme is highly appreciated. He puts lots of efforts in creating a good research environment in the laboratory. Moreover, I really like his curiosity and enthusiasm in every aspect of life whether it is research or sports. It really would not have been possible without him.

Second, I would like to extend my heartiest thanks to Assist. Prof. Derrick Mott in the Maenosono laboratory. His support towards my research is truly appreciable. He brings up new things for me every time I get a chance to meet him whether it is group meetings or in person. He has really helped me in giving good guidance towards writing scientific papers. His visions towards new ideas in the field of research is truly commendable.

Third, I would like to thank Prof. Mikio Koyano for guiding me in the subtheme research. His ideas and thoughts has helped me to groom my ideas and basic knowledge in the field of thermoelectric to larger extent. He has really helped in guiding me to operate PPMS machine for the measurement of thermoelectric properties for my sample.

I would like to thank Assist. Prof. Masanobu Miyata in Koyano lab for helping in carrying out the measurements, helping me in operating hot press machine and the analysis of the results. And, I would like to thank Dr. Shunsuke Nishino for helping me in the Seebeck measurements of my samples which helped a lot to understand my samples. I would like to thank Dr. Pham Xam Thi for helping me during the subtheme research. I would like to acknowledge Prof. Koichiro Suekuni as well.

Fourth, my sincere gratitude to Prof. Tatsuo Kaneko and Dr. Maiko Okajima for helping me during difficult time. Their mental support helped me a lot during my doctoral course journey. I am immensely happy to be working under his guidance as a post-doctoral researcher.

I express my sincere gratitude to the former students in Maenosono laboratory, Mr. Satoru Kodaira, Mr. Hiroyuki Shimose, Mr. Daisuke Hotta, Mrs. Sandhya Verma, Ms. Aparna Wadhwa, Ms. Dipali Ahuja, Ms. Rishika Rastogi, Ms. Kanika Gupta, Dr. Ian Godfrey, Dr. Aziliz Hervault, Mr. Simone Famiani, Dr. Priyank Mohan, Dr. Mari Takahashi, and current students Ms. Wei Zhou, Mr. Yujin Wang, Mr. Masahito Hatsukano, Mr. Takeshi Nakada, Ms. Pratibha Dwivedi, and former researchers Dr. Buhe Bateer, Mrs. Chiko Shijimaya. Immense mental support from all these people has been of great help. Thank you so much for having me amongst you.

I would also like to thank Dr. Takeo Akatsuka from Nippon Shokubai in helping me in sintering of the pellets using pulsed electric current sintering (PECS) and Dr. Michihiro Ohta and Mr. Fujimoto from AIST for helping me in taking thermoelectric properties measurements for my samples at higher temperatures.

I express my sincere happiness for my dear friends Dr. Manjit Singh Grewal, Dr. Priyank Mohan, Dr. Akanksha Matta, Dr. NG Lightson, Dr. Sumant Dwivedi, Dr, Asif Ali, Ms. Gargi Joshi, Mr. Anniruddha Nag for being in difficulties with me all the time.

Last but not the least, my family, I really want to thank you from my heart for keeping patience for all these years. Your patience is finally going to get paid off. Thank you for understanding for all hard and happy moments of my life.

Maninder Singh

Table of Contents

Chapter 1: Introduction

1.1 Energy Harvesting Materials and History of Thermoelectrics

With growing population, energy consumption has also accelerated which presents one of the most critical challenges in the current time. The energy from coal, petroleum, natural gas etc. is expected to deplete at faster rates at the current demand for the energy. It has been reported that 34 % of the energy from the utilization of coal, petroleum, natural gas is consumed by the factories, nuclear power plant, automobiles etc. and rest of the energy is wasted as heat and this waste heat is under 400 ^{o}C. If this waste heat can be captured and utilized, it will represent a significant energy savings.[1] Thermoelectric (TE) materials can be the promising candidate to utilize this waste heat. TE materials re-capture lost waste heat because they possess the ability to convert a heat gradient to an electric current. Such energy efficiency enhancing properties has sparked attention amongst researchers to create high performance TE materials which can help in improving energy usage efficiency and also can be used in supplemental energy generation for clean fuel.[2,3] Moreover, TE materials has beneficial properties, such as light weight, no moving parts, and low noise.[4,5] Before going further in TE materials, a brief history about TEs and underlying principle for the development of TE material is required. Underlying physics on which TE materials work are studied since early stage of 19th century. TE materials work on the principle of Seebeck effect.[6] In 1821, Thomas Johann Seebeck found that, on imposing a temperature gradient onto the dissimilar metals or semiconductors, a voltage gradient develops which can be observed in the form of the Seebeck effect. This effect arises due to the free movement of charge carriers (electrons or holes) in metals and semiconductors carrying charge as well as heat. Therefore, in the presence of temperature or heat gradient across the material, mobile charge carriers can diffuse from the hot end to the cold end of the material giving rise to the potential difference which can be expressed in the form of equation 1.1.

$$S = \Delta V / \Delta T \tag{1.1}$$

S is Seebeck coefficient (μV/K), ΔV is voltage difference (V), ΔT is temperature gradient (K). In 1909, Edmund Altenkirch[7] mathematically derived the relationship between parameters which includes S, thermal conductivity (κ) and electrical conductivity (σ) of TE generators which later integrated in 1949-1956 by scientist Abram F. Ioffe[8] into quantity known as the thermoelectric figure of merit (ZT) given by following equation 1.2.

$$ZT = \sigma S^2 T / \kappa \tag{1.2}$$

where σ is the electrical conductivity (S/m); T is the temperature (K); κ is the combination of electronic thermal conductivity due to charge carriers (κ_e), and lattice thermal conductivity due to phonons (κ_{lat}). κ_e is dependent on the σ according to the Weidemann-Franz law as shown in equation 1.3.[9,10]

$$\kappa_e = L\sigma T \tag{1.3}$$

Where L is the Lorenz number (2.44×10^{-8} WΩK^{-2}). The maximum power of TE material is proportional to the $S^2\sigma$ or known as power factor (PF, μW/mK^2). All these parameters are interrelated to each other. Change of one parameter will certainly effects the TE efficiency of the material. Therefore, choice of materials for TE applications should be made keeping the interrelation of these parameters to achieve high ZT value.

To make a choice of materials for TE applications it is really important for the materials to satisfy the condition of high S and σ and κ, to achieve high ZT[11] as per equation 1.1. But S and

σ are interrelated to each other in a reverse manner as per Mott's formula as shown in equation 1.4.[12,13]

$$S = \frac{8\pi^2 k_B^{\ 2}}{3eh^2} m^* T \left(\pi / 3n\right)^{2/3} \tag{1.4}$$

where m^* is the effective mass of the carrier, h is the Planck's constant, k_B is the Boltzmann constant. This relation shows S value decreases with increase in n and n is related to the σ as per equation 1.5.

$$\sigma = n\mu e \tag{1.5}$$

where n is the number of charge carriers, μ is the mobility of charge carriers, e is the electronic charge. So it is difficult task to decouple these two parameters from each other but both these parameters can be optimized to get high PF with low κ. In case of κ, as we know it is combination of both κ_e and κ_{lat}. And it is difficult task as well to decouple the κ_e from σ as both are interrelated in a direct manner. Only κ_{lat} component is beneficial in the reduction of κ[14] which will be discussed later in this chapter. Hence, for bulk materials these requirements become fundamental challenge to search for good TE materials.

It can be better understood from the qualitative behavior shown in Figure 1.1 where Metals have large σ and low S[15], thus low PF. Metals also have high thermal conductivity because of high charge carrier concentration. Thus, overall ZT of the metals becomes very low which makes them unsuitable for the TE applications. It is opposite in case of insulators, where S is very high but has low or no mobility of charge carriers. While in case of semiconductors both S and σ values are in between of metals and insulators. At low temperature semiconductors behave as insulator and on increasing temperature σ increases, thus electrical conductivity start

to increase. Both *S* and σ values can be optimized by varying charge carrier concentration to achieve maximum PF.[16] Thus, this property of semiconductors makes them useful for TE applications.

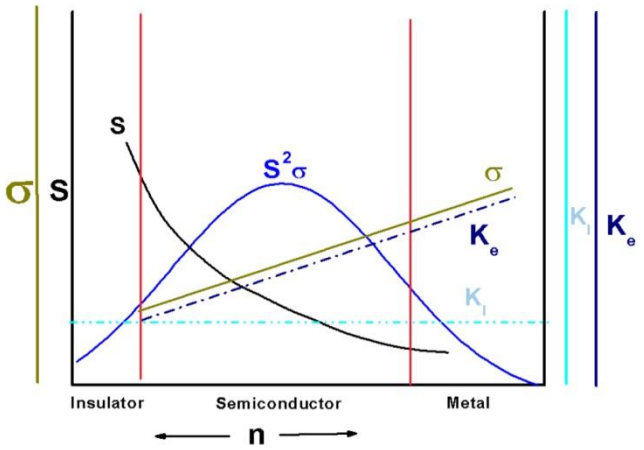

Figure 1.1. Interrelation between σ, *S*, PF, κ_e, κ_l (κ_{lat}).[16]

Since we know that semiconductors can be best for TE applications. Therefore early TE works were based on semiconductors which are chalcogenides based materials. Out of the various TE materials chalcogenides emerges as the promising candidates because of tunable band gap.

1.2. Chalcogenide based Thermoelectric Materials

Chalcogenides are chemical compounds composed of at least one chalcogen ion from group VI of the periodic table.[17,18] Chalcogenides are stable in air and have high melting points which makes the chalcogenide based material promising for TE applications.[19] Out of various chalcogenide based materials which has gained milestone for TE applications are Bi_2Te_3 and PbTe. TE performance of both Bi_2Te_3 and PbTe are described below.

Bi_2Te_3 is currently the finest TE material with efficient TE performance. It is binary chalcogenide semiconductor with narrow band gap of 0.15 eV.[20] Because of low band gap

values Bi_2Te_3 material was chosen for TE applications. In the late 1950's, Goldsmid and coworkers[21] had reported the TE properties of n- and p-type Bi_2Te_3 material with *ZT* value of 0.76 at 290 K and these both n-type and p-type materials could be operated at room temperature. Researchers thought to enhance the *ZT* of Bi_2Te_3 further to make it commercially more attractive. At the end of the 1960's, pace of research on these materials slowed down with several discussions among TE community that upper limit of *ZT* is around 1 and cannot be increased further. Thus, many research programs for TE materials were discontinued. After 1970, many parameters have been discussed among scientist and concept of low dimensional TE materials was introduced by Dresselhaus and coworkers[22-24] which kept the hope for enhancement of *ZT* alive. Some examples with enhanced TE performance of Bi_2Te_3 and PbTe is discussed below.

Yan and coworkers have successfully fabricated n-type $Bi_{2.0}Te_{2.7}Se_{0.3}$ bulk material using ball milling to introduce microstructures and hot pressing to achieve lower κ of 1.06 W/mK with κ_{lat} of 0.7 W/mK. It was established that the increase in the grain boundaries acted as a scattering center for the heat carrying phonons resulting into lower κ values.[25] Kim and coworkers fabricated material with composition $Bi_{0.4}Sb_{1.6}Te_{3.4}$ having excess of Te with impressive *ZT* value of 1.41 at 417 K which is suitable for low temperature applications.[26]

Now talking about PbTe and PbTe based materials are extensively studied and found interesting electronic properties. Maximum *ZT*= 1.8 at 850 K has been reported for Na doped $PbTe_{1-x}Se_x$.[27] Heremans and coworkers have known to report maximum *ZT* for the Tl for doped PbTe.[28] They obtained *ZT* of 1.5 for $Tl_{0.02}Pb_{0.98}Te$ thin film TE materials at 773 K. There increase in the carrier concentration and σ which leads to increase in the TE performance of the material to achieve maximum *ZT*.

Both Bi_2Te_3 and PbTe based TE materials have achieved *ZT* value greater than 1 (threshold value for materials to be used commercially) near room temperature and intermediate

temperature range (400-600 ºC) and are already employed for power generation applications. Despite of *ZT* value over 1, these material remain unsustainable in terms of toxicity, scarcity in earth's crust and expensive.[29,30] Te is known as one of the rarest elements which is only 0.001 ppm with respect to other elements in the earth's crust[31-35] which is even lower than rare earth elements like Ag and Au. Usage of Te for fabrication of TE materials, leads to increase in the market price. Thus, looking for an alternative material is a must.

Sulfur received the greatest attention of in TE materials because of its price is one-tenth of the price of Te. Thus, metal sulfides can be promising TE materials.[36]

Toxicity is also a major concern towards choosing environmentally compatible materials for TE applications. Even if the material possesses excellent TE properties but is highly toxic, it would not be possible to use it for TE applications in the future due to personal and environmental safety. Since Te, Pb and Sb have very low lethal dose-50 (LD_{50}) values, thus high toxicity. Thus, it is very important to look for environmentally benign TE materials.[37-39]

Because of all these limitations researchers are now investigating more environmentally benign material such as sulfide based TE materials which will be discussed in following sections.

Sulfide based Thermoelectric Materials

Since long, metal sulfides had been of great interest and were intensively studied as TE materials.[40-44] Binary metal sulfides such as $Cu_{2-x}S$ ($0<x<1$) are attractive to researchers to use them for TE applications as copper sulfide materials have low toxicity, low cost, earth abundance as shown in Figure 1.2 and have semiconducting properties which makes them useful to use in TE applications.[45,46]

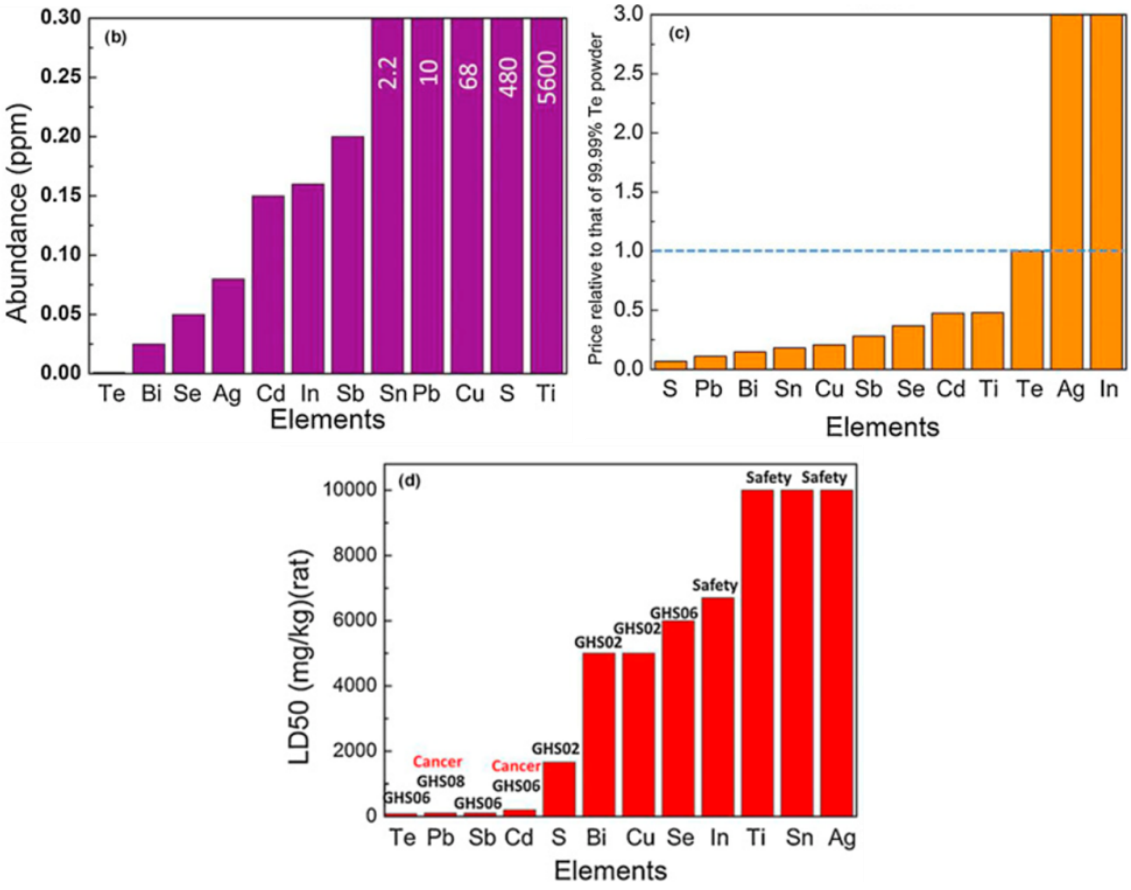

Figure 1.2. (b) The abundance of various elements employed in thermoelectric materials. (c) The price of elements compared with that of 99.99% Te powder (−200 mesh), where all price data were obtained from the Alfa Aesar Co. website. (d) The LD_{50} values and the GHS values of elements normally employed in thermoelectric materials. The GHS values run from 01 to 08, and very safe elements such as Ag and In have no GHS value.[45]

Copper Sulfide

Lately, good TE performance has been reported for materials such as $Cu_{1.96}S$ (djurelite, *dj*) and $Cu_{1.8}S$ (digenite, *di*)[47] because of superionic behavior of copper sulfide materials. In superionic behavior of copper sulfide materials, Cu ions become mobile and move in the crystal lattice when copper sulfide material is subjected to heat treatment. This movement of Cu ions affects the electrical and thermal properties of the copper sulfide material. Mobile Cu ions may help in enhancing the σ and reduce the κ because of glassy behavior of mobile Cu ions. This phenomenon is known as phonon liquid electron crystal (PLEC)[48] behavior in which the combination of liquid like κ and electronic properties like crystal and thus, involved

phenomenon makes the electrical and thermal properties of the copper sulfide system interesting. Thus, electrical and thermal transport properties of the copper sulfide materials were investigated because of their superionic behavior which attracted the researchers to explore this advantage further.[47] Combination of both $Cu_{1.96}S$ and $Cu_{1.8}S$ achieved *ZT* value of 0.5 at 673 K.[49] But still there are some problems associated with copper sulfide system which are discussed in the following sections.

Challenges for Copper Sulfides as Thermoelectric Material and Solution

From the above discussion, it can be inferred that copper sulfide can be promising material for TE applications but still there are some issues associated with copper sulfide material. There are thermal instability issues with this material and shows phase transitions when subjected to high temperatures as can be seen from Figure 1.3. Such frequent phase transitionsare restricting it's use in the practical applications.[50-51]

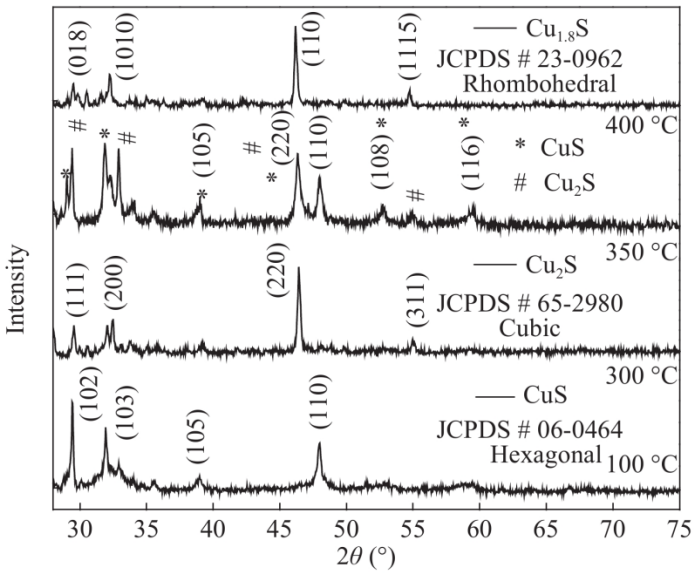

Figure 1.3. XRD patterns for the samples synthesized by annealing at 100, 300, 350, and 400 °C. The standard reference is also displayed. It is observed that the transition from one phase to another can be obtained by annealing.[51]

These thermal stability issues certainly affects the resulting *ZT* value of copper sulfide material[52] as can be seen in Figure 1.4, where the phase transition is evident with change in temperature.

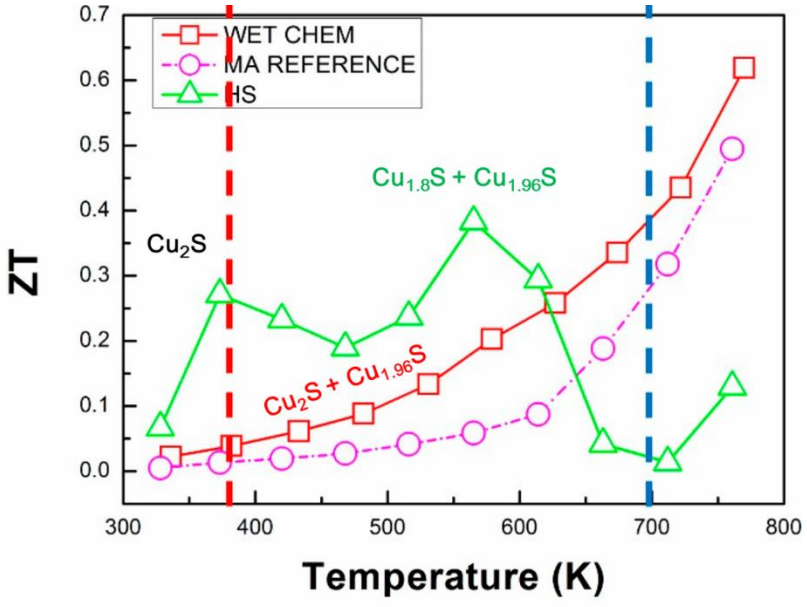

Figure 1.4. Temperature dependence of *ZT* of two bulk samples and reference.[52]

For this reason, we thought to enhance the thermal stability of Cu-S system by incorporating third element which is earth abundant, less toxic and inexpensive as well. Thus, we have investigated other sulfides like natural minerals which have been known for many years like Cu-Fe-S system which meets all the sustainability criteria.

So my research is focused on synthesis of Cu-Fe-S system to be used as TE material which is discussed in the following section.

Cu-Fe-S system as Thermoelectric Material

Various Cu-Fe-S systems can be fabricated as TE materials. In the literature it has been reported that chalcopyrite ($CuFeS_2$, *cp*)[53-57], isocubanite ($CuFe_2S_3$, *cb*)[58-60], and Bornite

(Cu_5FeS_4, *bn*)[61-63] are the sulfide materials which have semiconductor properties and can be explored for TE applications. Presence of Fe in the Cu-S system provides extra stability to the Cu-S system. Immobile Fe atoms are substituted at copper sites and thus, hamper the movement of Cu atoms in the lattice. This provides structural stability for the Cu-S system.[62] Other elements can be chosen over Fe such as Zn, Mn, Co but firstly we focused on Fe as third element.

In addition, the Cu–Fe–S system can be either a p- or n-type semiconductor depending on the composition.[54,59,62] Cu-Fe-S systems have been extensively studied individually and various approaches have been devised to enhance the *ZT* value of the materials. Some of the examples with brief information about Cu-Fe-S materials along with their TE properties are discussed below which helps us to understand the Cu-Fe-S materials in a better way.

Bornite

bn is a copper sulfide based mineral which is widely spread in variety of ore deposits under various geological conditions[64] and and its high cubic crystal structure with five Cu atoms, one Fe atom and two vacancies randomly occupy the center of eight sulfur tetrahedrons is shown in Figure 1.5. This material is comparatively stable than copper sulfide material from room temperature to above 1373 K.[65] *bn* has a completely disordered crystal structure due which results in ultra-low κ_{lat} of this material because mean free path (MFP) in *bn* is 0.23 nm[61] and has band gap of 0.27 eV which results in tunable electrical properties. Usually sulfides have high κ because of light atomic mass of sulfur but it is interesting to know that this material has lower κ_{lat} values observed at wide temperatures. Thus *bn* had been explored as TE material.

Qiu and co-workers[61] have fabricated stoichiometric *bn* using top-down approach and found that *ZT* of stoichiometric *bn*, Cu_5FeS_4 is 0.38 at 663 K. They also fabricated off stoichiometric $Cu_{5.02}Fe_{0.98}S_4$, and $Cu_{5.04}Fe_{0.96}S_4$ showing higher *ZT* value of 0.5 at 663 K because off-

stoichiometric *bn* materials can provide more hole carriers and thus result into enhanced σ. which means that this if this material becomes slightly copper rich, its TE properties can be easily tuned. Thus, this material holds better stability than copper sulfides.

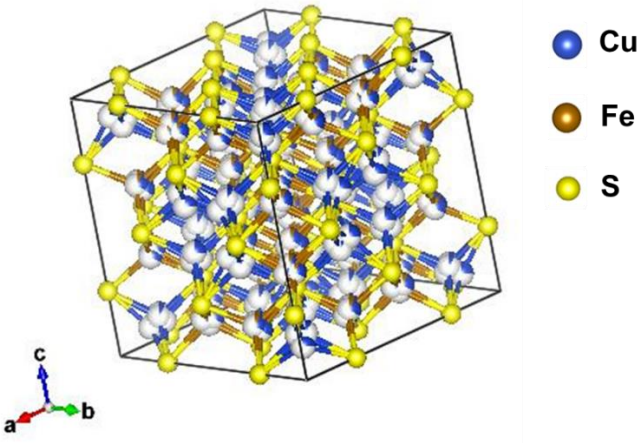

Figure 1.5. Crystal structure of *bn*.

Chalcopyrite

cp is the most abundant and inexpensive naturally occurring copper mineral. It crystallizes into tetragonal system as shown in Figure 1.6. Its crystal structure is closely related to the zinc blend but unit cell of *cp* is twice as large as zinc blend unit cell. Being most sustainable among other materials *cp* can be considered for TE application having a band gap of 0.53 eV.[66] In the literature, *cp* is mostly synthesized using top down approach such as mechanical alloying, spark plasma sintering for fabricating TE materials.

It has been reported that the carrier concentration of $Cu_{1-x}Fe_{1+x}S_2$ can be tuned within a wide range by varying *x*. For example, $n = 0.34 \times 10^{20}$ cm^{-3} when $x = 0$, while $n = 7.02 \times 10^{20}$ cm^{-3} when $x = 0.1$.[55] Due to change in *n*, both *S* and σ values can vary widely even if the XRD pattern remains same as of *cp*. In a wet chemical approach for the synthesis of *cp* material

particle of size 6.4 nm was reported[67] to give p-type conductivity and *ZT* of 0.264 at 500 K which is 77 times greater than *cp* synthesized by solid state methods.

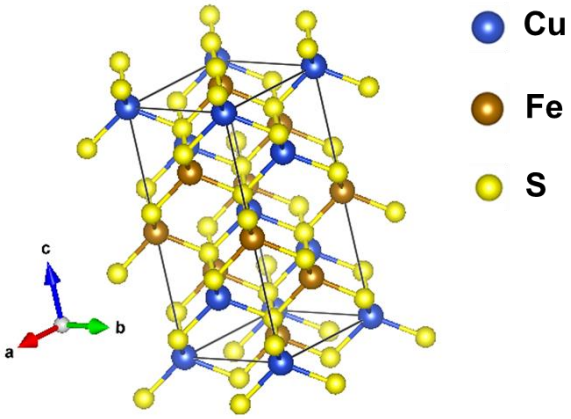

Figure 1.6. Crystal structure of *cp*.

Isocubanite

cb is also a natural mineral which is not available in the pure form but coexist with *cp* and pyrrhotite (*po)*.[58] and meets all the sustainability criteria. It is also a semiconductor material with n-type conductivity and has not been extensively studied as TE material. Its crystal structure is shown in Figure 1.7.

Only one research article has been reported where *cb* has been studies as TE material. In this, *cb* was fabricated using top-down approach and it shows the *ZT* value of 0.13 at 650 K.[58]

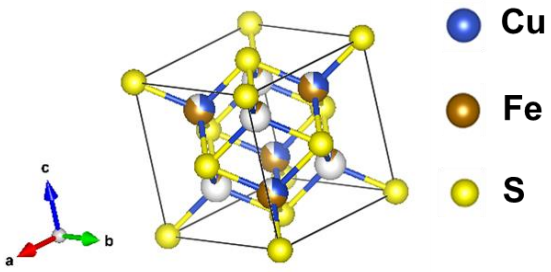

Figure 1.7. Crystal structure of *cb*.

Research work included in this dissertation is focused on the synthesis and characterization of Cu-Fe-S type system. Objective of the research work done is briefly described in the research objective section.

All these three systems have been fabricated by using top down approaches such as vacuum melting method or mechanical alloying method. This top down approach is much time and energy consuming processes which is why energy and time efficient bottom-up/ wet / colloid chemical approach was used to fabricate Cu-Fe-S TE material. Quantitative analysis of both approaches are mentioned below

To synthesize *cp* samples melting-annealing-sintering process is employed in which high purity elements Cu, Fe and S in stoichiometric proportions were sealed in evacuated quartz tubes and heated slowly upto 1400 K for 36 hours. After which it is allowed to cool down naturally to room temperature. Obtained ingots were ground into fine powders and cold pressed before resealing in quartz tube. Sealed tubes were annealed at 800-900 K for 7 days and obtained material is again ground to fine powder before subjecting it to spark plasma sintering at 800-820 K at 60 MPa pressure.[55] In case of *bn*, high purity elements Cu, Fe, S were taken in stoichiometric atomic ratio and sealed in evacuated quartz ampoules and heated to 1273 K slowly for 20 hours. Ingots obtained were annealed at 873 K for 5 days and then ground into

fine powder before subjecting to spark plasma sintering at 773 K for 5 minutes.[61] Thus, overall fabrication process looks very time and energy consuming.

On the other hand, fabrication process of Cu-Fe-S TE material using wet / colloid chemical approach is much time and energy efficient. Because, if we follow through the fabrication process in colloid chemical approach. Sample preparation involves use of precursors. But precursors are dissolved in suitable solvent and kept under Ar atmosphere for 5-10 minutes which is much time and energy efficient as compared to fabrication using vacuum melting method. Then synthesis of the material usually takes less synthesis time (about 1-2 hours) and washing and ligand exchange of material obtained takes about 4-6 hours. By comparing above two approaches in quantitative manner, colloid chemical approach is way much time and energy efficient.

1.3. Role of Nanotechnology to Enhance Thermoelectric Efficiency

To achieve higher *ZT*, it is necessary to fabricate materials having high *PF* than κ as per equation 1.2. It can be done by reducing κ_{lat}, which will have positive effect on reduction of κ because κ_e and σ are interdependent to each other according to the Weidemann- Franz law. Thus, reducing the κ_{lat} can be one of the possible solution to enhance the *ZT*. The κ_{lat} can be given by following equation 1.6.

$$\kappa_{lat} = \frac{1}{3} C_v v l \tag{1.6}$$

where C_v is the heat capacity at constant volume; v is the phonon velocity; l is the MFP, where C_v , v are constant, so the κ_{lat} is governed by the MFP.[68] Altering C_v and v is difficult as both these quantities are constant for solids. Main focus is to reduce the MFP of long wavelength

phonons because heat is carried by long wavelength phonons.[69] The MFP of phonons can be reduced by many methods such as nanostructuring[69,70]

Nanostructured materials can be easily synthesizes by means of a wet chemical approach which allows the scale up of the reaction from molecular precursors to create large scale TE materials. This solution based synthetic approach allows the ability to tune the shape, size and electronic properties of the material effectively which is challenging in the case of solid state synthesis approach or top-down approach to bring down the material from micro scale to nanoscale.[71]

1.4 Research Objective

For last many years, TE materials with high *ZT* values such as PbTe, Bi_2Te_3 have been studied which consists of toxic Pb and rare Te earth elements. Toxicity and scarcity of these elements in the earth's crust make these elements not suitable for commercial use. So, the investigation for new class of sustainable materials have been started which could meet the sustainability requirements and can match upto the efficiency of the state of the art unsustainable bulk materials. Moreover, at the same time research was going on to further enhance the *ZT* value of the state of the art bulk material by means of nanostructuring (one of the solution to enhance the *ZT*).

Objective of this research is to do fundamental study for the alternative TE materials by fabricating Cu-Fe-S NPs by colloid chemical or bottom-up approach. Idea of use of both sustainable system and nanostructuring is employed in this dissertation work to design new class of sustainable nanostructured TE material.

Bottom-up/ wet chemical approach has been used to fabricate copper sulfide, iron sulfide and Cu-Fe-S nanobulk TEs. This synthetic approach enables direct control over shape, size and crystal phase. Since, we know that tuning the size of the NPs depends on the scattering length

of phonons and thus, can reduce the lattice thermal conductivity. We targeted this phenomenon of nanostructuring as one of the solution to our materials composed of copper, iron, and sulfur and successfully demonstrated the enhancement in the *ZT* value. Copper sulfide, iron sulfide and Cu-Fe-S systems are widely studied semiconducting materials. Thus, these material have great potential to be studied for TE materials. Research work presented in this dissertation is designed by keeping the main objective in mind and will give more insight about designing of new class sustainable TE nanomaterial.

In chapter 2, colloid chemical approach was employed to fabricate different types copper iron sulfide NPs using Cu-Fe-S NPs as building block and samples were processed into a solid pellet for further TE measurements at room temperature. Thiourea was used as the sulfur source in the fabrication of Cu-Fe-S NPs because thiourea has very small chain length as compared to dodecanethiol which gives advantage of shorter interparticle distance. Thus, no ligand exchange was done and no thermal treatment was given to the pellets. Seebeck measurements of all the pelletized samples were done at room temperature. Fabrication and fundamental studies of Cu-Fe-S NPs with modest TE properties at room temperature gives curiosity to explore such materials more at higher temperatures.

In chapter 3, research work was designed to make use of copper sulfide, iron sulfide NPs as building blocks for the synthesis of Cu-Fe-S nanobulk material. These building blocks were blended into liquid state and sintered to give dense bulk materials. Inter grown minor phases acting as nanoprecipitate or nanoinclusons along with the main Cu-Fe-S phases can be highly beneficial to effectively enhance the electrical conductivity of the fabricated Cu-Fe-S TE material as intergrown nanopahases have high electrical conductivity which increases the electrical conductivity of the fabricated samples. Moreover, these phases can act as scattering centers for phonon. Thus, reducing the κ_{lat} and provides more support in the enhancement of overall TE performance of the fabricated nanomaterial. In chapter 4, TE properties on the basis

of crystal structure will be thoroughly discussed and chapter 5 will give the general conclusions for the dissertation work.

Many researchers have reported the fabrication of Cu-Fe-S system using top down and bottom up approaches using different fabrication protocols but fabrication of Cu-Fe-S nanobulk system have not been tried using dual nanoparticle system method and using the same synthetic protocol which is the originality and novelty of this research. In all the reported articles, two different nanoparticles system were not used to create Cu-Fe-S nanobulk material. In this protocol Cu-Fe-S nanobulk material was prepared by mixing Cu_2S and FeS in different volume ratios followed by pulsed electric current sintering (PECS).

References

(1) Jacobson, M. Z.; Delucchi, M. A. Providing all Global Energy with Wind, Water, and Solar Power, Part I: Technologies, Energy Resources, Quantities and Areas of Infrastructure, and Materials. *Energy Policy* **2011**, 1154-1169.

(2) Minnich, A. J.; Dresselhaus, M. S.; Ren, Z. F.; Chen, G. Bulk Nanostructured Thermoelectric Materials: Current Research and Future Prospects. *Energy Environ. Sci.* **2009**, *2*, 466-479.

(3) Zhang, X.; Zhao, L.-D. Thermoelectric Materials: Energy Conversion between Heat and Electricity. *J. Materiomics* **2015**, *1*, 92-105.

(4) Zheng, X. F.; Liu, C. X.; Yan, Y. Y. A Review of Thermoelectric Research-Recent Developments and Potentials for Sustainable and Renewable Energy Applications. *Renew. Sustain. Energy Rev.* **2014**, *32*, 486-503.

(5) LeBlanc, S. Thermoelectric Generators: Linking Material Properties and Systems Engineering for Waste Heat Recovery Applications. *Sustain. Mater. Technol.* **2014**, *1*, 26-35.

(6) Velmre, E. Thomas Johann Seebeck. *Proc.Estonian Acad. Sci. Eng.* **2007**, *13*, 276-282.

(7) Altenkirch, E. Über den Nutzeffekt der Thermosäule. *Physikalische Zeitschrift* **1909**, *10*, 560-580.

(8) Vedernikov, M. V.; and Iordanishvili, E. K. A. F. Ioffe and Origin of Modern Semiconductor Thermoelectric Energy Conversion. *17th Int. Conf. on Thermoelectrics* 1998, *1*, 37-42.

(9) William, J.; Norman, H. M. Theoretical Solid State Physics. Courier Dover Publications **1985**.

(10) Franz. R.; Wiedemann G. Ueber die Wärme-Leitungsfähigkeit der Metalle *Ann. Phys. Lpz.* **1853**, *165*, 497-531.

(11) Park, J.; Xia, Y.; Ozoliņš, V. High n-Type Thermoelectric Power Factor and Efficiency in Ba_2BiAu from a Highly Dispersive Band. *Cond-Mat. Mtrl-Sci.* **2018**, *1*.

(12) Cutler, M.; Mott, N. Observation of Anderson Localization in an Electron Gas. *Phys. Rev.* **1969**, *181*, 1336-1340.

(13) Cutler, M.; Leavy, J. F.; Fitzpatrick, R. L. Electronic Transport in Semimetallic Cerium Sulfide. *Phys. Rev.* **1964**, *133*, A1143.

(14) Hwang, J.-Y.; Kim, E. S.; Hasan, S. W.; Choi, S.-M.; Lee, K. H.; Kim, S. W. Reduction of Lattice Thermal Conductivity in PbTe Induced by Artificially Generated Pores. *Adv. Cond. Matter Phys.* **2015**, 1-6.

(15) Batal, M. A.; Nashed, G.; Jneed, F. H. Conductivity and Thermoelectric Properties of Nanostructure Tin Oxide Thin Films. *J. Assoc. Arab Univ. Basic Appl. Sci.***2014**, *15*, 15-20.

(16) Masood, K. B.; Kumar, P.; Singh, R. A.; Singh, J. Odyssey of Thermoelectric Materials: Foundation of the Complex Structure. *J. Phys. Commun.* **2018**, *2*, 062001.

(17) Sousa, V. Chalcogenide Materials and Their Application to Non-Volatile Memories. *Microelectron. Eng.* **2011**, *88*, 807-813.

(18) Greenwood, N. N.; Earnshaw, A. Chemistry of the Elements. *Oxford: Butterworth-Heinemann.* **1997.**

(19) Rosi, F. D. Thermoelectricity and thermoelectric power generation. *Solid. State. Electron.* **1968**, *11*, 833–848.

(20) Heikes, R. R.; Ure, R. W. Thermoelectricity: Science and Engineering. (Interscience, **1961**).

(21) Goldsmid H. J.; Douglas, R. W. The use of Semiconductors in Thermoelectric Refrigeration. *British J. Appl. Phys.* **1954**, *5*, 386.

(22) Hicks, L. D.; Dresselhaus, M. S. Thermoelectric Figure of Merit of a One-Dimensional Conductor. *Phys. Rev. B* **1993**, *47*, 16631-16634.

(23) Hicks, L. D.; Dresselhaus, M. S. Effect of Quantum-Well Structures on the Thermoelectric Figure of Merit. *Phys. Rev. B* **1993**, *47*, 12727-12731.

(24) Heremans, J. P.; Dresselhaus, M. S.; Bell, L. E.; Morelli, D. T. When Thermoelectrics Reached the Nanoscale. *Nat. Nanotechnol.* **2013**, *8*, 471-473.

(25) Yan, X.; Poudel, B.; Ma, Y.; Liu, W. S.; Joshi, G.; Wang, H.; Lan, Y.; Wang, D.; Chen, G.; Ren, Z. F. Experimental Studies on Anisotropic Thermoelectric Properties and Structures of n-Type $Bi_2Te_{2.7}Se_{0.3}$. *Nano Lett.* **2010**, *10*, 3373-3378.

(26) Kim, Y. M.; Lydia, R.; Kim, J.-H.; Lin, C.-C.; Ahn, K.; Rhyee, J.-S. Enhancement of Thermoelectric Properties in Liquid-Phase Sintered Te-Excess Bismuth Antimony Tellurides Prepared by Hot Press Sintering. *Acta Mater.* **2017**, *135*, 297-303.

(27) Pei, Y.; Shi, X.; LaLonde, A.; Wang, H.; Chen, L.; Snyder, G. J. Convergence of Electronic Bands for High Performance Bulk Thermoelectrics. *Nature* **2011**, *473*, 66.

(28) Heremans, J. P.; Jovovic, V.; Toberer, E. S.; Saramat, A.; Kurosaki, K.; Charoenphakdee, A.; Yamanaka, S.; Snyder, G. J. Enhancement of Thermoelectric Efficiency in PbTe by Distortion of the Electronic Density of States. *Science* **2008**, *321*, 554.

(29) Hébert, S.; Berthebaud, D.; Daou, R.; Bréard, Y.; Pelloquin, D.; Guilmeau, E.; Gascoin, F.; Lebedev, O.; Maignan, A. Searching for New Thermoelectric Materials: Some Examples Among Oxides, Sulfides And Selenides. *J Phys. Cond. Matter* **2015**, *28*, 013001.

(30) Yang, Q.; Hu, C.; Wang, S.; Xi, Y.; Zhang, K. Tunable Synthesis and Thermoelectric Property of Bi_2S_3 Nanowires. *J. Phys. Chem. C* **2013**, *117*, 5515-5520.

(31) LeBlanc, S. Thermoelectric Generators: Linking Material Properties and Systems Engineering for Waste Heat Recovery Applications. *Sustain. Mater. Technol.* **2014**, *1*, 26-35.

(32) Yadav, G. G.; Susoreny, J. A.; Zhang, G.; Yang, H.; Wu, Y. Nanostructure-Based Thermoelectric Conversion: An Insight into the Feasibility and Sustainability for Large-Scale Deployment. Nanoscale **2011**, *3*, 3555-3562.

(33) Zhang, J.; Song, L.; Pedersen, S. H.; Yin, H.; Hung, L. T.; Iversen, B. B. Discovery of High-Performance Low-Cost n-Type Mg_3Sb_2-Based Thermoelectric Materials with Multi-Valley Conduction Bands. *Nat. Commun.* **2017**, *8*, 13901.

(34) Amatya, R.; Ram, R. J. Trend for Thermoelectric Materials and Their Earth Abundance. *J. Electron. Mater.* **2012**, *41*, 1011-1019.

(35) Abundance in Earth's Crust. Web Elements.com. (The University of Sheffield and WebElements Ltd., 1993–2010 http://www.webelements.com).

(36) Grønvold, F.; Stølen, S.; Westrum, E. F.; Galeas, C. G. Thermodynamics of Copper Sulfides III. Heat Capacities and Thermodynamic Properties of $Cu_{1.75}S$, $Cu_{1.80}S$, and $Cu_{1.85}S$ from 5 to about 700 K. *J. Chem. Thermodyn.* **1987**, *19*, 1305-1324.

(37) Zevalkink, A.; Toberer, E. S.; Zeier, W. G.; Flage-Larsen, E.; Snyder, G. J. Ca_3AlSb_3: An Inexpensive, Non-Toxic Thermoelectric Material for Waste Heat Recovery. *Energy Environ. Sci.* **2011**, *4*, 510-518.

(38) Miller, S. A.; Gorai, P.; Aydemir, U.; Mason, T. O.; Stevanović, V.; Toberer, E. S.; Snyder, G. J. SnO as a Potential Oxide Thermoelectric Candidate. *J. Mater. Chem. C* **2017**, *5*, 8854-8861.

(39) Lee, M. H.; Kim, K.-R.; Rhyee, J.-S.; Park, S.-D.; Snyder, G. J. High Thermoelectric Figure-of-Merit in Sb_2Te_3/Ag_2Te Bulk Composites as Pb-Free p-Type Thermoelectric Materials. *J. Mater. Chem. C* **2015**, *3*, 10494-10499.

(40) Jood, P.; Ohta, M. Hierarchical Architecturing for Layered Thermoelectric Sulfides and Chalcogenides. *Materials* **2015**, *8*, 1124-1149.

(41) Lee, M.-J.; Ahn, J.-H.; Sung, J. H.; Heo, H.; Jeon, S. G.; Lee, W.; Song, J. Y.; Hong, K.-H.; Choi, B.; Lee, S.-H.; Jo, M.-H. Thermoelectric Materials by using Two-Dimensional Materials with Negative Correlation between Electrical and Thermal Conductivity. *Nat. Comm.* **2016**, *7*, 12011.

(42) Mansour, B. A. *Phys. Stat. Soli.* A Electrical and Thermoelectric Properties of In and Cd Doped $Cu_{1.8}S$. **1993**, *136*, 153-159.

(43) Lou, Y.; Samia, A. C. S.; Cowen, J.; Banger, K.; Chen, X.; Lee, H.; Burda, C. Evaluation of the Photoinduced Electron Relaxation Dynamics of $Cu_{1.8}S$ Quantum Dots. *Phys. Chem. Chem. Phys.* **2003**, *5* (6), 1091–1095.Agarwal, K.; Mehta, B. R. *J. Appl. Phys.* **2014,** *116*, 083518.

(44) Grønvold, F.; Stølen, S.; Westrum, E. F.; Galeas, C. G. Thermodynamics of Copper Sulfides III. Heat Capacities and Thermodynamic Properties of $Cu_{1.75}S$, $Cu_{1.80}S$, and $Cu_{1.85}S$ from 5 to about 700 K. *J. Chem. Thermodyn.* **1987**, *19*, 1305-1324.

(45) Rabinal, M. H. K.; Mulla, R. Copper Sulfides: Earth Abundant and Low Cost Thermoelectric Materials. *Energy Technol.* **2018**.

(46) Qiu, P.; Zhu, Y.; Qin, Y.; Shi, X.; Chen, L. Electrical and Thermal Transports of Binary Copper Sulfides Cu_xS with x from 1.8 to 1.96. *APL Mater.* **2016**, *4*, 104805.

(47) Miller, T. A.; Wittenberg, J. S.; Wen, H.; Connor, S.; Cui, Y. Lindenberg, A.M. The Mechanism of Ultrafast Structural Switching in Superionic Copper (I) Sulphide Nanocrystals. *Nat. Comm.* **2013**, *4*, 1369.

(48) Ge, Z.-H.; Zhao, L.-D.; Wu, D.; Liu, X.; Zhang, B.-P.; Li, J.-F.; He, J. Low-Cost, Abundant Binary Sulfides as Promising Thermoelectric Materials. *Mater. Today* **2016**, *19*, 227-239.

(49) Ge, Z.-H.; Zhang, B.-P.; Chen, Y.-X.; Yu, Z.-X.; Liu, Y.; Li, J.-F. Synthesis and Transport Property of $Cu_{1.8}S$ as a Promising Thermoelectric Compound. *Chem. Commun.* **2011**, *47*, 12697-12699.

(50) Quintana-Ramirez, P. V.; Arenas-Arrocena, M. C.; Santos-Cruz, J.; Vega-González, M.; Martínez-Alvarez, O.; Castaño-Meneses, V. M.; Acosta-Torres, L. S.; de la Fuente-Hernández, J. Growth Evolution and Phase Transition from Chalcocite to Digenite in Nanocrystalline Copper Sulfide: Morphological, Optical and Electrical Properties. *Beilstein J. Nanotechnol.* **2014**, *5*, 1542-1552.

(51) Narjis, A.; Outzourhit, A.; Aberkouks, A.; El Hasnaoui, M.; Nkhaili, L. Structural and Thermoelectric Properties of Copper Sulphide Powders. *J. Semicond.* **2018**, *39*, 122001.

(52) Tang, Y.-Q.; Ge, Z.-H.; Feng, J. Synthesis and Thermoelectric Properties of Copper Sulfides via Solution Phase Methods and Spark Plasma Sintering. *Crystals* **2017**, *7*, 141.

(53) Singh, M.; Miyata, M.; Nishino, S.; Mott, D.; Koyano, M.; Maenosono, S. Chalcopyrite Nanoparticles as a Sustainable Thermoelectric Material. *Nanomaterials* **2015**, *5*, 1820-1830.

(54) Xie, H.; Su, X.; Yan, Y.; Liu, W.; Chen, L.; Fu, J.; Yang, J.; Uher, C.; Tang, X. Thermoelectric Performance of $CuFeS_{2+2x}$ Composites Prepared by Rapid Thermal Explosion. *NPG Asia Mater.* **2017**, *9*, e390.

(55) Li, Y.; Zhang, T.; Qin, Y.; Day, T.; Snyder, G. J.; Shi, X.; Chen, L. Thermoelectric Transport Properties of Diamond-Like $Cu_{1-x}Fe_{1+x}S_2$ Tetrahedral Compounds. *J. Appl. Phys.* **2014**, *116*, 203705.

(56) Xie, H.; Su, X.; Zheng, G.; Zhu, T.; Yin, K.; Yan, Y.; Uher, C.; Kanatzidis, M. G.; Tang, X. The Role of Zn in Chalcopyrite $CuFeS_2$: Enhanced Thermoelectric Properties of $Cu_{1-x}Zn_xFeS_2$ with In Situ Nanoprecipitates. *Adv. Energy Mater.* **2016**, *7*, 1601299.

(57) Tsujii, N.; Mori, T.; Isoda, Y. Phase Stability and Thermoelectric Properties of $CuFeS_2$-Based Magnetic Semiconductor. *J. Electron. Mater.* **2014**, *43*, 2371-2375.

(58) Barbier, T.; Berthebaud, D.; Frésard, R.; Lebedev, O. I.; Guilmeau, E.; Eyert, V.; Maignan, A. Structural and Thermoelectric Properties of n-Type Isocubanite $CuFe_2S_3$. *Inorg. Chem. Front.* **2017**, *4*, 424-432.

(59) Zhang, X.; Zhao, H.; Zhu, Y.; Yang, Y.; Jiang, D.; Chen, X.; Sun, J.; Luo, J.; Cai, B.; Fan, H. Facile Synthesis of Nano-Sized $CuFe_2S_3$: Morphology and Diverse Functional Tuning and Crystal Growth Mechanism Exploring. *Regen. Biomater.* **2017**, *4*, 223-231.

(60) Lyubutin, I.; Lin, C.-R.; Starchikov, S.; Siao, Y.-J.; Tseng, Y. Synthesis, Structural and Electronic Properties of Monodispersed Self-Organized Single Crystalline Nanobricks of Isocubanite $CuFe_2S_3$. *J. Solid State Chem.* **2015**, *221*, 184-190.

(61) Qiu, P.; Zhang, T.; Qiu, Y.; Shi, X.; Chen, L. Sulfide Bornite Thermoelectric Material: A Natural Mineral with Ultralow Thermal Conductivity. *Energy Environ. Sci.* **2014**, *7*, 4000-4006.

(62) Long, S. O. J.; Powell, A. V; Vaqueiro, P.; Hull, S. High Thermoelectric Performance of Bornite Through Control of the Cu(II) Content and Vacancy Concentration. *Chem. Mater.* **2018**, *30*, 456-464.

(63) Zhang, A.; Shen, X.; Zhang, Z.; Lu, X.; Yao, W.; Dai, J.; Xie, D.; Guo, L.; Wang, G.; Zhou, X. Large-Scale Colloidal Synthesis of Cu_5FeS_4 Compounds and Their Application in Thermoelectrics. *J. Mater. Chem.* C **2017**, *5*, 301–308.

(64) Grguric, B. A.; Putnis, A. Compositional Controls on Phase Transition Temperatures in Bornite: a DSC Study. *Can. Min. J.* **1998**, *36*, 215-227.

(65) Robie, R. A.; Seal, R. R.; Hemingway, B. S. Heat Capacity and Entropy of Bornite (Cu_5FeS_4) between 6 and 760 K and the Thermodynamic Properties of Phases in the System Cu-Fe-S. *Can. Min. J.* **1994**, *32*, 945-956.

(66) Austin, I. G.; Goodman, C. H. L.; Pengelly, A. E. New Semiconductors with the Chalcopyrite Structure. *J. Electrochem. Soc.* **1956**, *103*, 609-610.

(67) Liang, D.; Ma, R.; Jiao, S.; Pang, G.; Feng, S. A Facile Synthetic Approach for Copper Iron Sulfide Nanocrystals with Enhanced Thermoelectric Performance. *Nanoscale* **2012**, *4*, 6265-6268.

(68) Slack, G. A. The Thermal Conductivity of Nonmetallic Crystals. *Solid State Phys.* **1979,** *34*, 1-71.

(69) Wang, Y.; Huang, H.; Ruan, X. Decomposition of Coherent and Incoherent Phonon Conduction in Superlattices and Random Multilayers. *Phys. Rev. B* **2014**, *90*, 165406.

(70) Kanatzidis, M. G. Nanostructured Thermoelectrics: The New Paradigm? *Chem. Mater.* **2009**, *22*, 648-659.

(71) Nikam, A. V.; Prasad, B. L. V.; Kulkarni, A. A. Wet Chemical Synthesis of Metal Oxide Nanoparticles: A Review. *Cryst. Eng. Comm.* **2018**, *20*, 5091-5107.

Chapter 2: Colloid Chemical Approach to Fabricate Cu-Fe-S Thermoelectric Materials using Cu-Fe-S Nanoparticles as Building Blocks

2.1 Abstract

Earth abundant, inexpensive, less-toxic and interesting TE properties of Cu-Fe-S bulk systems have led us to investigate Cu-Fe-S system fabricated using colloid chemical approach. Fabrication of Cu-Fe-S NPs using colloid chemical approach using single precursors was done and the samples were further characterized for TE properties. In this chapter, different Cu-Fe-S NPs were synthesized by changing the input feeding ratio of copper and iron precursors. The advantage in this process is straight forward fabrication of Cu-Fe-S pellet samples without doing any ligand exchange and special treatment such as annealing or PECS. Thiourea was used as sulfur source and capping ligand because chain length of thiourea (one carbon) is much smaller than other sulfur sources such as dodecanethiol which has 12 carbons. All the pelletized samples were characterized in terms of structure, composition, morphology and Seebeck values (at room temperature). All pelletized samples revealed p-type conductivity. Reported results will give more clarity to design and fabricate Cu-Fe-S NP system for TE applications.

2.2 Introduction

In the field of energy materials, nanotechnology has already found many uses. NPs and the related nano-fabrication techniques have been used in catalysts for fuel cells[1], in solar panels as the light collecting component[2], for hydrogen production[3] and storage[4], as well as a host of other applications. More recently nanotechnology has been used in TE materials, which has the potential to greatly enhance our current energy production efficiency. TE materials rely on the Seebeck and Peltier effects to convert an electric current to a heat gradient, or vice versa. By utilizing these phenomena, TE materials can be used to generate electricity from nearly any heat source, for example an automobile engine, in steam turbine electricity generation, or even

direct geothermal energy. Till now though, TE materials have not found widespread use because of their inherently low energy conversion efficiency, described by the dimensionless figure of merit, *ZT*. In recent years, however, new techniques revolving around nanotechnology have been developed that have opened up the doors to improving the *ZT* value. Techniques such as nanostructuring allow suppression of the thermal conductivity, which is a useful tool to enhance *ZT*. While this development has been exciting in light of the improved efficiency values, there are still many challenges left to address from the aspect of material sustainability. The very best TE materials available today (i.e. Bi_2Te_3, $BiSbTe_3$, PdTe, etc) contain either rare or toxic elements that limit their practical application[5-8]. Tellurium is one such element that is present in nearly all of the high efficiency TE materials because of its beneficial electronic band properties[8,9], but the element is extremely rare in the earth making these materials increasingly expensive. With this in mind, new sustainable TE materials must be sought out that do not rely on rare or toxic elements. To accomplish this, the nanotechnology techniques that have been pioneered in enhancing the TE efficiency of the traditional materials should now be applied to sustainable materials systems to elucidate and identify new techniques for optimizing TE properties through the material characteristics such as particle size, shape, composition, structure or interparticle properties[8]. In this work, we developed a synthetic approach toward NPs composed of copper, iron and sulfur, which is attractive because of the abundant nature of the constituent elements. Apart from this abundant nature, the Cu-Fe-S system is chosen for its structural properties which can prove to be beneficial for good TE characteristics[10,11].

The colloid chemical approach used allows control of the nanoparticle composition by changing the metallic feeding ratio. Cu_2S (and its related materials) is a widely studied semiconductor material[12-15], and the particles can be created in a straightforward thermolysis reaction.[16,17] The resulting particle characteristics are studied using techniques such as TEM,

XRD and ICP-OES, then the material is processed into a solid pellet to characterize the Seebeck value of the material. The processing of the sample for Seebeck measurement does not include any ligand exchange or thermal treatment of the NPs, which is highly beneficial since it preserves the true nanoparticle size. This fundamental difference for our materials provides a great contrast to the past studies on the TE materials composed of chalcopyrite. It is also important to note that the Seebeck value for bulk chalcopyrite is n-type, which is in contrast to our measured value showing p-type conductivity. While doping of the chalcopyrite material can be used to control the type of conduction providing further merits to this sustainable nanoparticle system for TEs.

2.3 Materials

List of the chemicals used for the fabrication of Cu-Fe-S NPs is shown in Table 2.1. All the chemicals have been used as received without further purification.

Table 2.1. List of the chemicals, their chemical formula or abbreviation, and purity %.

Chemicals	Chemical Formula / Abbreviation	Purity %
Copper nitrate hydrate	$Cu(NO_3)_2 \cdot xH_2O$	99.9
Iron sulfate heptahydrate	$FeSO_4 \cdot 7H_2O$	99.9
Tetraethylene glycol	$OH(CH_2CH_2O)_3CH_2CH_2OH$ / TEG	99.9
Thiourea	$SC(NH_2)_2$	99.0
Methanol	CH_3OH	99.8
Ethanol	C_2H_5OH	99.5

2.4 Experimental

Synthetic Technique for Cu-Fe-S Nanoparticles

Cu-Fe-S NPs were synthesized using a modified polyol method. A total of 10 millimoles of $Cu(NO_3)_2 \cdot xH_2O$ and $FeSO_4 \cdot 7H_2O$ precursors were used. The molar feeding ratio of copper and iron precursors was varied as shown in Table 2.2 for a total of 4 samples. Pure iron sulfide NPs were not prepared because the synthetic conditions used could not lead to the formation of iron sulfide NPs. In a typical synthesis, first the copper precursor, 200 mL of TEG as solvent and 12 millimoles of thiourea were added into a three neck round-bottom flask. One of the flask necks was used for monitoring the reaction temperature by thermocouple probe, another neck was fitted with a gas trap and condenser to catch volatile materials during the synthesis and the final neck was used for injecting reactants and for bubbling argon through the reaction solution. The reaction mixture was stirred at 600 rpm using a magnetic stirring bar with argon bubbling and was kept at room temperature for 5 minutes to remove the air. After that, the flask was heated to 240 °C. When the temperature of the reaction flask reached 170 °C a stock solution containing iron precursor dissolved in 10 ml of methanol was injected into it. The methanol quickly evaporated and was caught in the gas trap. After the reaction temperature reached 240 °C and was maintained at 240 °C for one hour. The solution color changed from light grey to black, indicating the starting of formation of NPs. After the reaction, the heating mantle was removed and the reaction mixture was cooled down to room temperature. General synthetic technique for Cu-Fe-S NPs is shown in Scheme 2.1.

The reaction mixture was centrifuged at 5000 rpm for 10 minutes and supernatant was removed. In this case, we expect the NPs to be coated in thiourea, which would make the particles soluble in polar solvents. After this first washing, the particles were further purified by washing with a methanol. The particles were dispersed in 50 ml of methanol with the help of sonication. The mixture was then centrifuged at 5000 rpm for 10 minutes. The supernatant was removed and this process of washing was repeated thrice. The resulting NPs were dried and used for subsequent characterization.

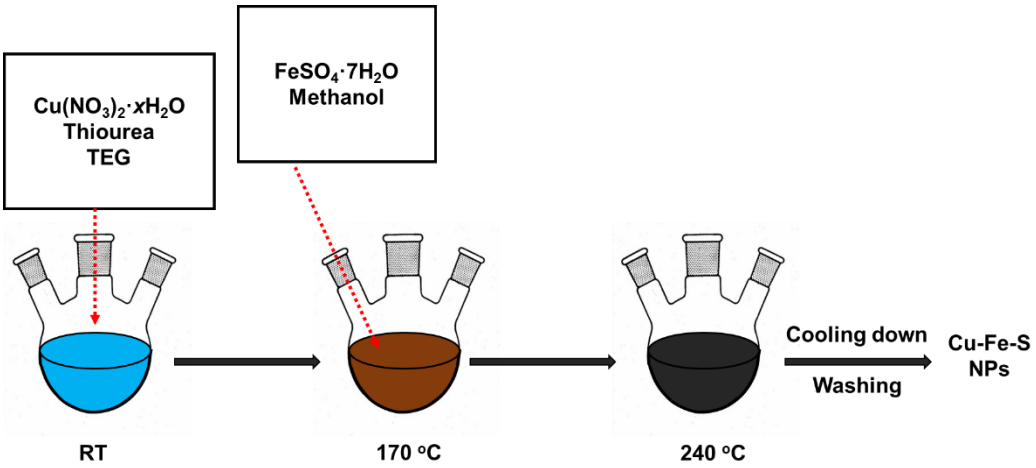

Scheme 2.1. General synthetic scheme for Cu-Fe-S NPs system.

Table 2.2. Input molar ratio of metallic precursors for the Cu-Fe-S NPs system.

Sample	Copper nitrate (mmol)	Iron sulfate (mmol)	Cu:Fe (mol %)
Sample_10/0	10	0	100:00
Sample_7/3	7	3	70:30
Sample_1/1	5	5	50:50
Sample_1/3	3	7	30:70
Sample_0/10	0	10	0:100

2.5 Characterization Techniques

After synthesizing the NPs, next step is to characterize the NPs using various characterization techniques. A wide range of instruments were used in the characterization of the NPs studied here. The crystalline properties of the samples were analyzed by XRD with a Rigaku Miniflex instrument, Cu K_α radiation (λ= 0.15418 nm) at 30 kV and 15 mA over a 2θ range of 20-70°. TEM characterization was performed using a Hitachi H-7100 and H-7650 operating at 100 kV. Samples were prepared by drop-casting in a dilute solution of NPs in methanol/ toluene

solution onto a Cu TEM grid (from Ted Pella). Sample composition was studied using inductively coupled plasma-optical emission spectroscopy (ICP-OES) using a Shimadzu ICPS-7000 instrument. Energy dispersive X-ray spectroscopy (EDS) data for these samples were collected using a Hitachi H-7650. The accelerating voltage of the electron beam was 100 kV. Data for multiple regions of the Cu-Fe-S NP system was collected. Further these NPs samples were subjected to TE properties measurements.

In order to measure the *S* of these materials, they must first be processed into a solid pellet. The NPs were dried in vacuum and then each sample was pelletized using a hydraulic pellet press. Each sample was pressed with a pressure of 40 MPa for 5 h and pellets with a nominal thickness of ~5 mm and a 10 mm diameter were obtained as shown in Figure 2.1. The pellet was cut into a square piece using a wire cutter, after this procedure the samples were ready for *S* measurement.

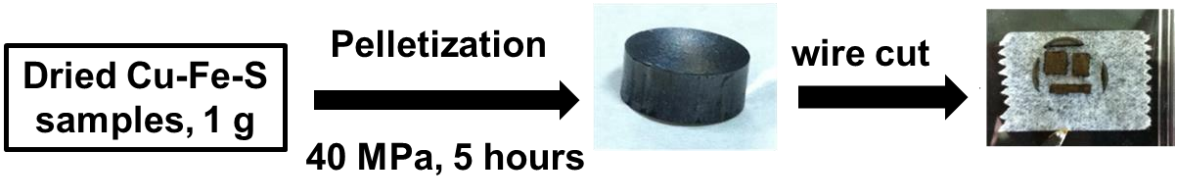

Figure 2.1. Schematic illustration of pelletization and sample cutting using for σ and *S* measurement using diamond wire cutter.

The Seebeck measurement was conducted twice for each sample using different pieces of pellet. The pellet piece was fixed onto a glass plate using grease. Two thermocouples (consisting of copper and constantan wires) were fixed onto each side of the pellet using gold paste. The other end of the thermocouple wires were immersed in ice bath to create a reliable reference for temperature (0 °C) and then went on to be attached to a nano-voltmeter to measure the voltage difference between the thermocouples when a heat gradient is created within the pellet. One side of the pellet was heated by contact with a hot soldering gun and the resulting

temperature and voltage changes were recorded. The resulting plots of change in temperature versus the TE voltage reveal the *S* by taking the slope of the fit line of data.

The *S* for each sample was measured twice in Cu-Fe-S NP system was analyzed at room temperature on a homemade Peltier device[3] as shown in Figure 2.2.

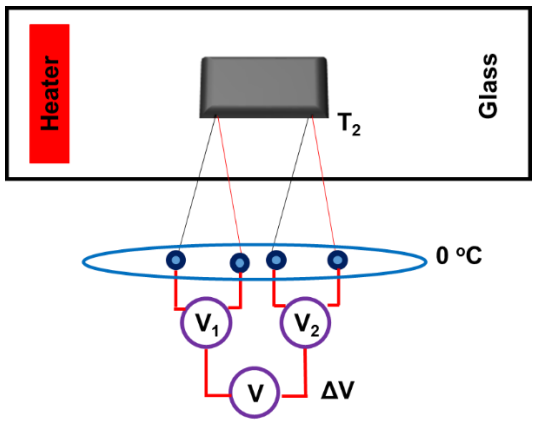

Figure 2.2. Schematic illustration of set up for thermoelectric voltage measurement.

2.6 Results and Discussion

2.6.1 Morphology and Crystal Structure

After the synthesis, a dispersion of NPs in methanol was drop-cast on a carbon coated copper micro-grid and was analyzed using TEM. Figure 2.3 shows the resulting representative TEM image of sample_10/0. For Sample_10/0, (metallic feeding ratio 100% Cu) the particles appear to be spherical in shape with a size of 25.1 ± 2.5 nm and in some places spiky morphology was observed.[17] In this case the particles are lying on the TEM grid face down. Along with spherical shape particles some areas on the TEM grid are showing spiky morphology of the particles.

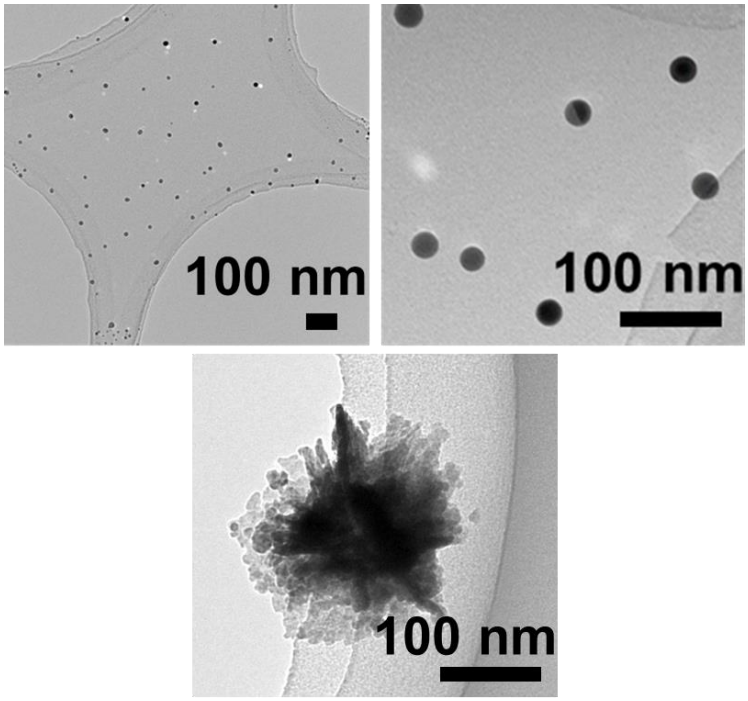

Figure 2.3. TEM image of sample_10/0

For sample_7/3 (metallic feeding ratio of 70% Cu, 30% Fe) however, the particle morphology remains spiky. Some rod-like features can be observed in the image embedded in large clumps. Moving to sample_1/1 (metallic feeding ratio of 50% Cu, 50% Fe) and sample_1/3 (metallic feeding ratio of 30% Cu, 70% Fe), the rods become more pronounced and seem to have a central focal point for each cluster. This central point may be the originating nucleation point for each cluster of particles as shown in Figure 2.4. The clumpy material itself may in fact be sheets of nanoparticle material, which would be consistent with the morphology observed for the parent copper sulfide NP material.[18,19]

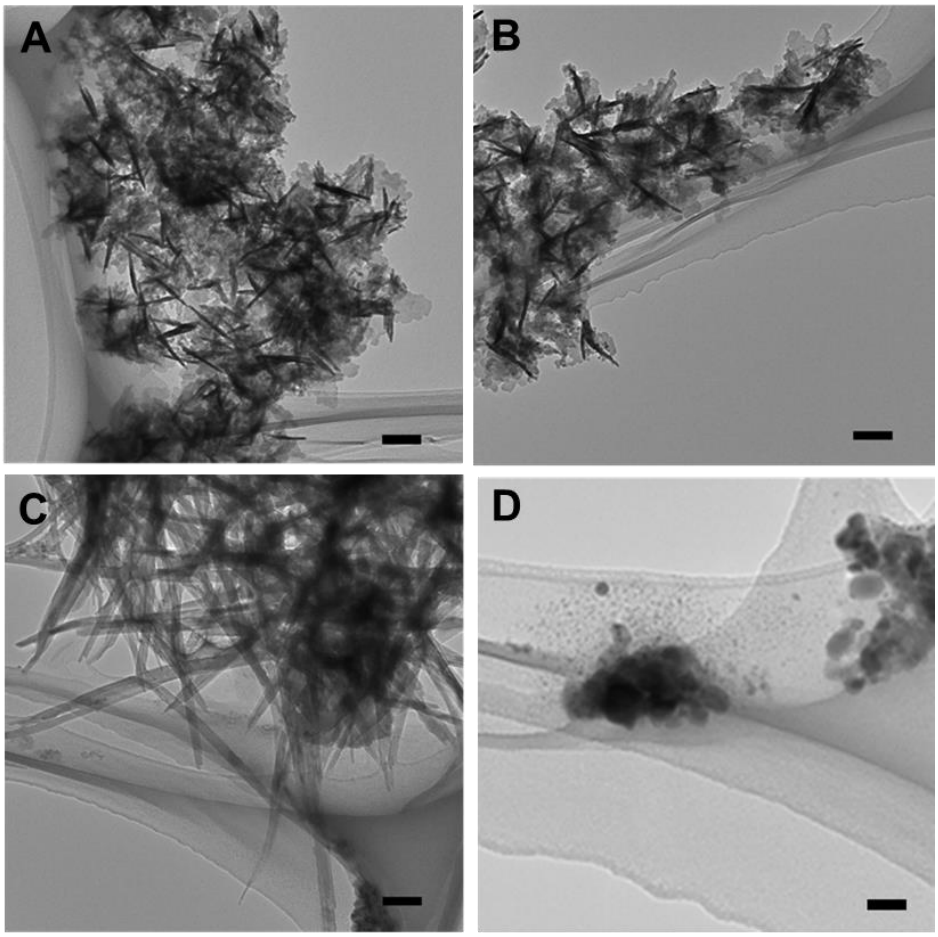

Figure 2.4. TEM images of NPs (A) sample_7/3, (B) sample_1/1, (C) sample_1/3, and (D) sample_0/10. All scale represents 100 nm.

Origin of this spiky morphology of these particles is due to the use of type of the sulfur source in the synthesis. It was reported that morphology depends on the rate of release of sulfide ions into the reaction mixture.

Fabrication of copper-thiourea aqueous has already been studied to obtain copper sulfide NPs and morphology of these copper sulfide nanomaterials have been studied in the presence of different sulfur sources such as sodium sulfide (Na_2S), thioacetamide ($SC(CH_3)(NH_2)$), and $SC(NH_2)_2$ separately in ethylene glycol by Li and coworkers. Ref For growth process of crystals, it includes nucleation stage followed by growth stage. Formation of crystallographic phase of the seed formed during the synthesis is responsible for the resulting morphology of

the particles. Nucleating stage also depends on the nature of the reactant and surrounding medium of the particles.

Presence of different sulfur sources have great impact on final morphology of the particles. Different sulfur sources have different release rate of S^{2-} ions. Na_2S easily dissociates into sodium (Na^{2+}) ions and sulfide (S^{2-}) ions in the presence of ethylene glycol and formation of copper sulfide nuclei occurs very rapidly. Because of high concentration of S^{2-} copper sulfide nuclei grow isotropically. In case of $SC(CH_3)(NH_2)$, S^{2-} are readily released but concentration of S^{2-} is little lower than in Na_2S. Thus, results in weak anisotropic growth.

In case of $SC(NH_2)_2$, because of strong complex between Cu^{2+}, $SC(NH_2)_2$, and ethylene glycol. This strong complex formation leads to lesser amount of S^{2-} in the reaction solution resulting in the anisotropic growth of copper sulfide particles.[17]

This phenomenon is possible in our studies as well where NPs are obtained in the presence of $SC(NH_2)_2$ in TEG. Because of strong complex formation between Cu^{2+}, $SC(NH_2)_2$, and TEG, insufficient amount of S^{2-} in the reaction solution gives much time to grow NPs in particular direction owing anisotropic growth of the NPs.

The NPs were next analyzed with XRD to study the crystalline characteristics of the NPs. Figure 2.5 shows the resulting XRD patterns produced for each sample in the analysis. For sample_10/0, a clear pattern is obtained that matches cubic phase *di*[20], consistent with the expected result. However, for sample_7/3, non-symmetrical peaks are obtained, particularly the primary peak matches with the location for the 660 line for cubic $Cu_{1.39}S$[20] and has a shoulder matching with the 400 line for tetragonal $Cu_{5.43}Fe_{1.08}S_4$.[20] The results indicate a mixture of these two phases for sample_7/3. For sample_1/1, the peaks align closely to the reference locations for tetragonal *cp*[20], which is consistent with the metallic feeding ratio used for this sample. The asymmetry observed will be discussed in Rietveld refinement of sample_1/1. Finally, for sample_1/3, the observed peaks match the reference for tetragonal *cp*

and cubic *cb*.[20] The XRD pattern does not match with the input amount of precursors. The XRD pattern shows mixture of both tetragonal *cp* and cubic *cb*. It is confirmed that Sample_1/3 is a mixture of *cp* and more of iron. Presence of mixture in sample_1/3 can also be analyzed using EDS analysis as shown in the Figure 2.11. In the low angle region however, many low intensity and relatively sharp features are observed. These do not quantitatively meet the criteria to be considered peaks, and may arise as a result of organic impurities in the particles or could be due to unreacted precursors. These features do not match any known oxides of copper or iron. As a last qualitative observation, in general the broad peaks observed in sample_7/3, sample_1/1, and sample_1/3 show that the particles possess a smaller grain size when compared to sample_10/0. This is contrary to the visual inspection of the TEM images but could be due to the clumpy material in sample_7/3, sample_1/1, and sample_1/3 being composed of very thin sheets, which would lead to the observed peak broadening. In general, we observe a systematic shift from the cubic phase of *di* to tetragonal *cp* as the metallic feeding ratio of iron is increased.

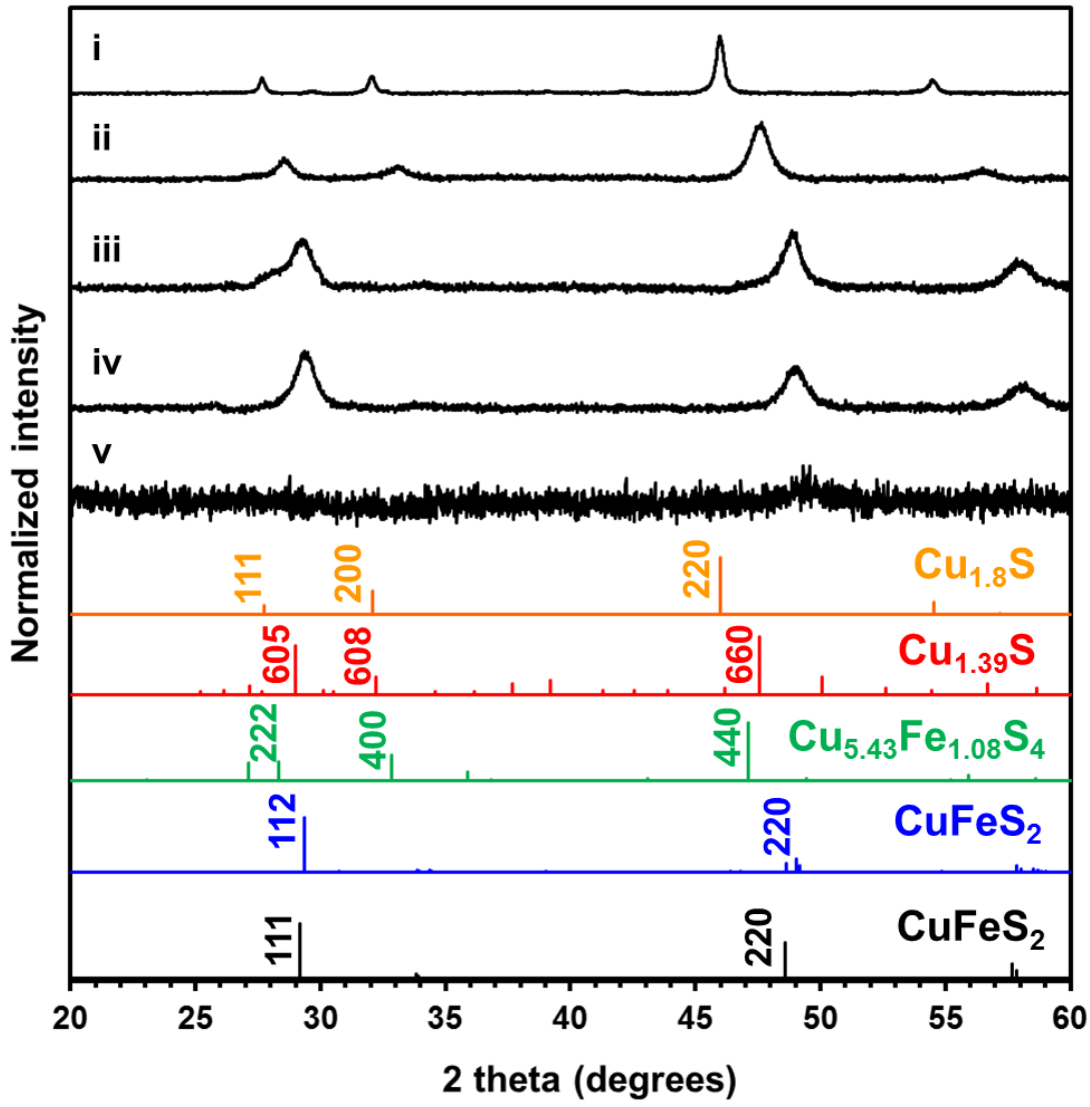

Figure 2.5. XRD patterns of NPs (i) sample_10/0, (ii) sample_7/3, (iii) sample_1/1, (iv) sample_1/3, and (v) sample_0/10.[21]

The Rietveld analysis of Sample_7/3 was not possible because of unavailability CIF file of phase $Cu_{1.39}S$ but for Sample_1/1 and Sample_1/3 was done using FULLPROF software as shown in Figure 2.6. In Sample_1/1, *cp* is the major phase observed whereas *nu* is the minor phase observed. *cb* was observed as main phase in Sample_1/3 with *vol* % of 55 % along with minor *cp* phase with *vol* % of 45 %. The χ^2 value is 15.0 and 10.9 is observed for Sample_1/1 and Sample_1/3 respectively, which is quite high to be considered as good fit. This high χ^2 value is probably because of low signal to noise ratio.

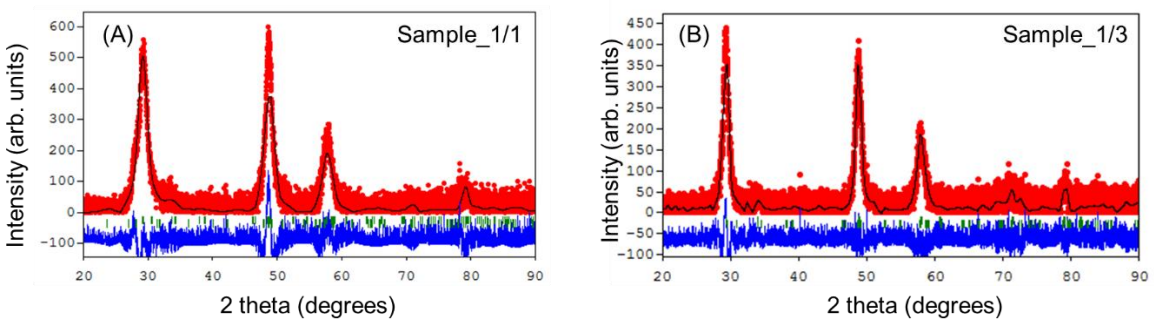

Figure 2.6. Rietveld refinement of the powder XRD pattern of (A) Sample_1/1, and (B) Sample_1/3. The experimental patterns are shown as red circles and the calculated patterns are shown as black lines. The χ^2 value is 15.0 and 10.9 respectively. The Bragg reflection positions are shown as short green bars below the diffraction patterns. The blue lines represent the difference patterns.

Sampling experiments was also performed before and after injection of the iron precursor to investigate the type of particles formed before and after the injection of the iron precursor. Two sets of experiments were performed for sampling the particles before and after injection of iron precursor. In the first set of the experiment, when the temperature reached 170 ^{o}C, 5 ml of reaction mixture was taken out immediately to check morphology and crystal structure of the particles formed. Figure 2.7 shows the morphology of the particles formed before the injection of iron precursor. Two kinds of morphologies were observed during the TEM investigation. One with spiky morphology and second, small spherical particles can be seen.

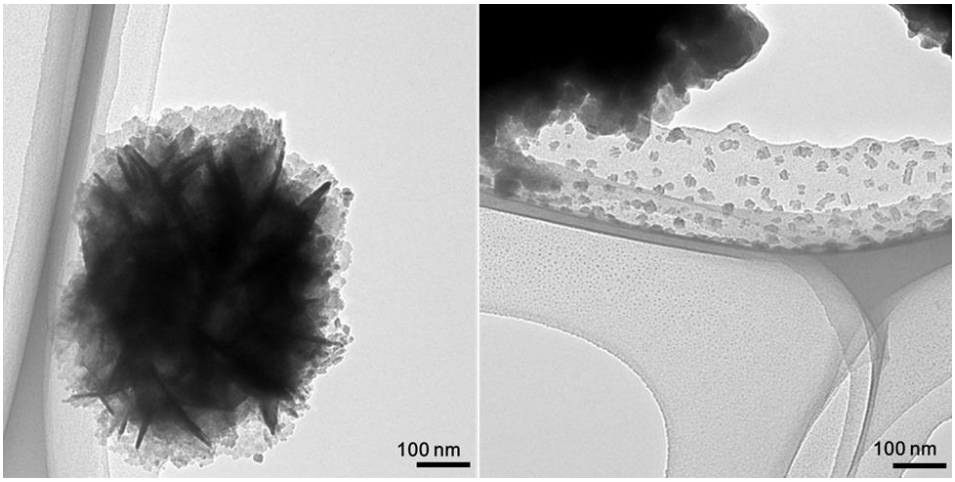

Figure 2.7. TEM image of the NPs sampled before the injection of iron precursor.

These NPs were analyzed using XRD to investigate the crystal structure of the NPs formed. It was found that NPs formed are composed of beta-CuSCN (beta-copper thiocyanate), and CuS (covellite, *co*) as shown in Figure 2.8.

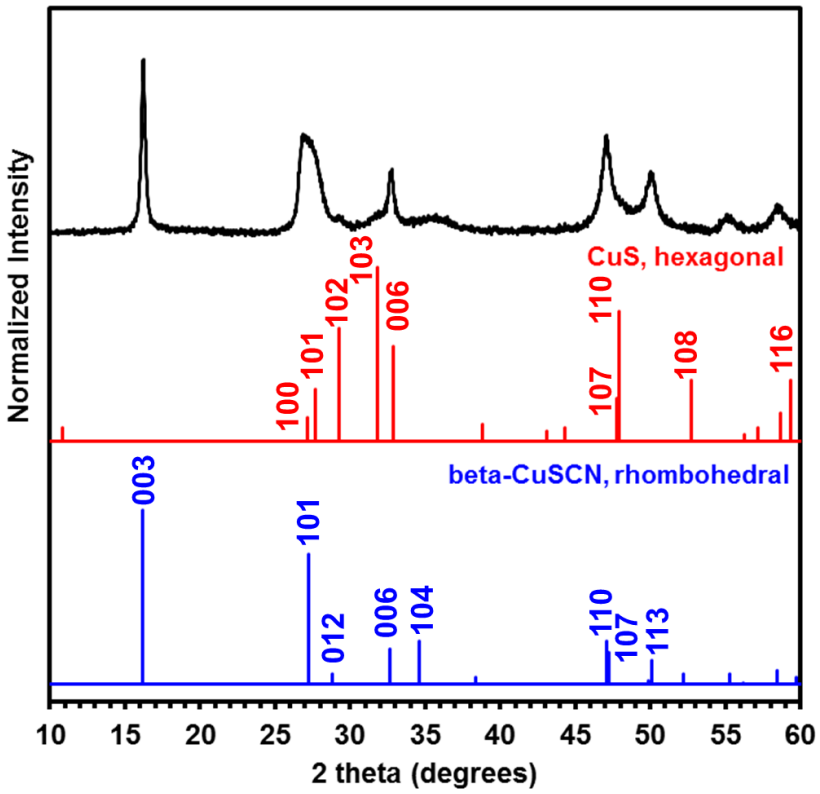

Figure 2.8. XRD of the NPs sampled before the injection of iron precursor.[20]

In the second set of the experiment, when the temperature reached 170 ^{o}C and iron precursor was injected, 5 ml of reaction mixture was taken out immediately to check morphology and crystal structure of the particles formed. Figure 2.9 shows the morphology of the particles formed after the injection of iron precursor. Spiky morphology was observed even after the injection of the iron precursors. No small spherical particles were observed in this case.

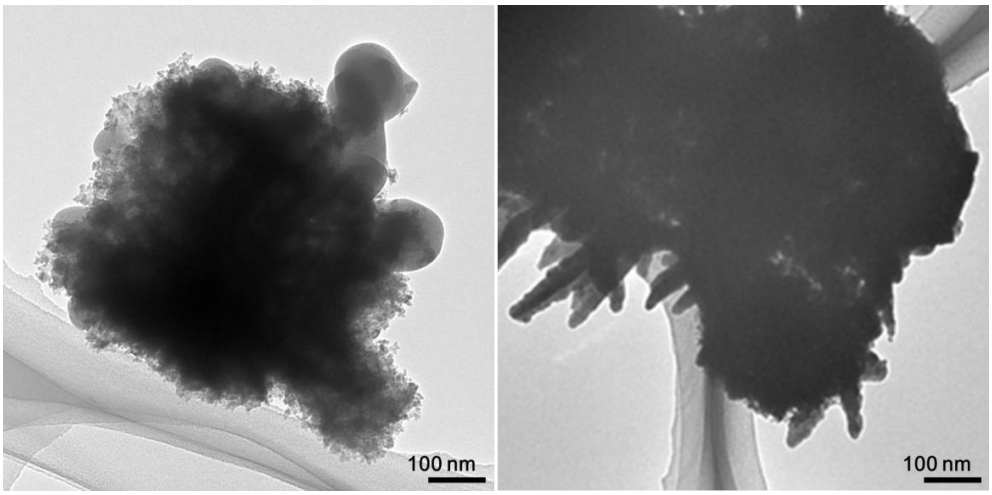

Figure 2.9. TEM image of the NPs sampled after the injection of iron precursor.

These NPs were analyzed using XRD to investigate the crystal structure of the NPs formed. It was found that NPs formed are composed of beta-CuSCN (beta-copper thiocyanate), and Cu_5FeS_4 (*bn*) as shown in Figure 2.10.

In conclusion it was observed that Fe did not reduce immediately after injection at 170 ^{o}C and took time to reduce during the course of the reaction.

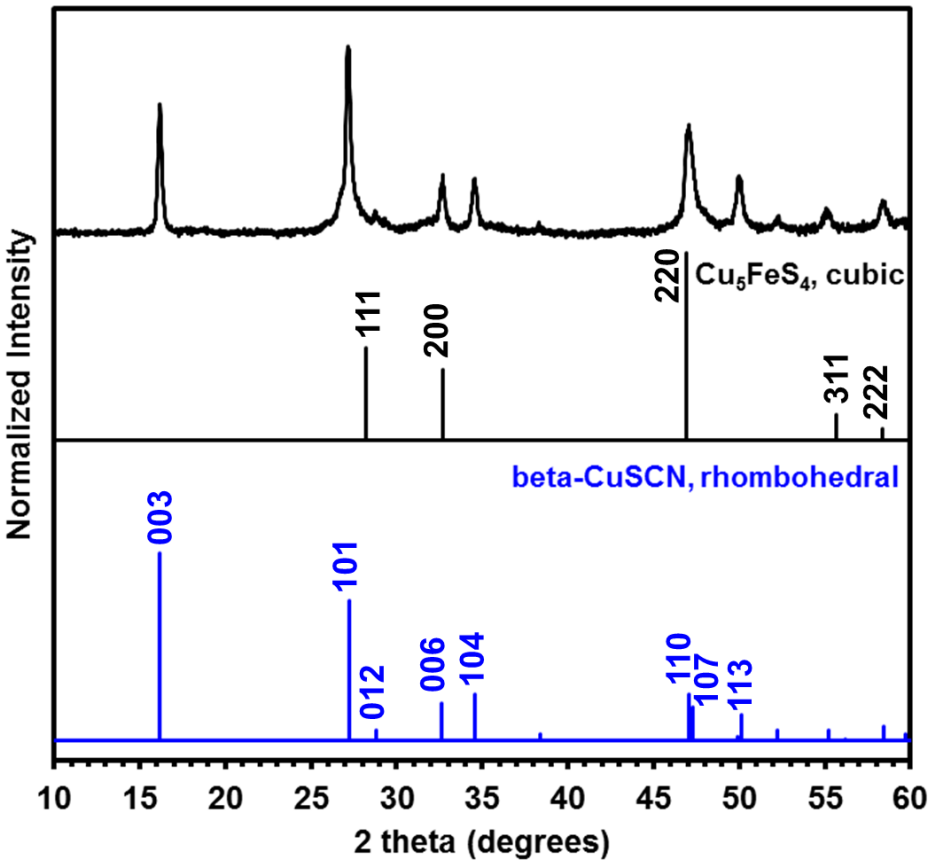

Figure 2.10. XRD of the NPs sampled before the injection of iron precursor.[20]

2.6.2 Compositional Analysis

To gain an understanding of the material composition, ICP-OES was performed for each sample. Nanoparticle (0.5 mg) samples were dissolved in 1 mL of aqua-regia, and then were diluted with distilled water to a volume of 50 mL to achieve a total dilution of about 10 ppm concentration. Calibration curves for copper and iron were created by using ICP standard solutions of each metal at 2, 4, 6, 8 and 10 ppm. The samples were analyzed, and the calibration curves were used to calculate the nanoparticle compositions. The material atomic compositions are shown in Table 2.3. In addition, the nanoparticle compositions were measured using EDS (which is integrated with the TEM technique). The samples, which were cast onto carbon coated copper micro grids for TEM, were used in the EDS analysis. Several areas were selected in each grid which included several NPs. The composition from these areas was averaged.

These results are also shown in Table 2.3. While the composition for most samples matches closely with the observed XRD patterns, sample_1/3 appears to contain an excess amount of iron (the XRD pattern matches closely with that of the CuFeS2 material while the composition shows a content of about 49% iron). To investigate why the metallic feeding ratio of sample_1/3 does not seem consistent with the apparent composition or crystal structure observed with XRD we analyzed the composition of several different areas using EDS. In sample_1/3 there are two different types of particle observed, one consisting of the nano rods (Area 1) and separate areas that appear dark and clumpy (Area 2). We independently analyzed the composition of these areas and found that the composition is different for these two types of particles. The nanorods (Area 1) have a composition consistent with the crystal structure observed in XRD (51% Cu and 49% Fe) while the clumpy particles (Area 2) contain much more iron (20% Cu and 80% Fe). Based on these results, we believe that the iron rich areas are amorphous in nature, which is why it is not observed in the XRD pattern. This would also explain where the excess iron in the feeding ratio ends up. Additional data on the EDS composition analysis for sample_1/3 is provided in the Figure 2.11.

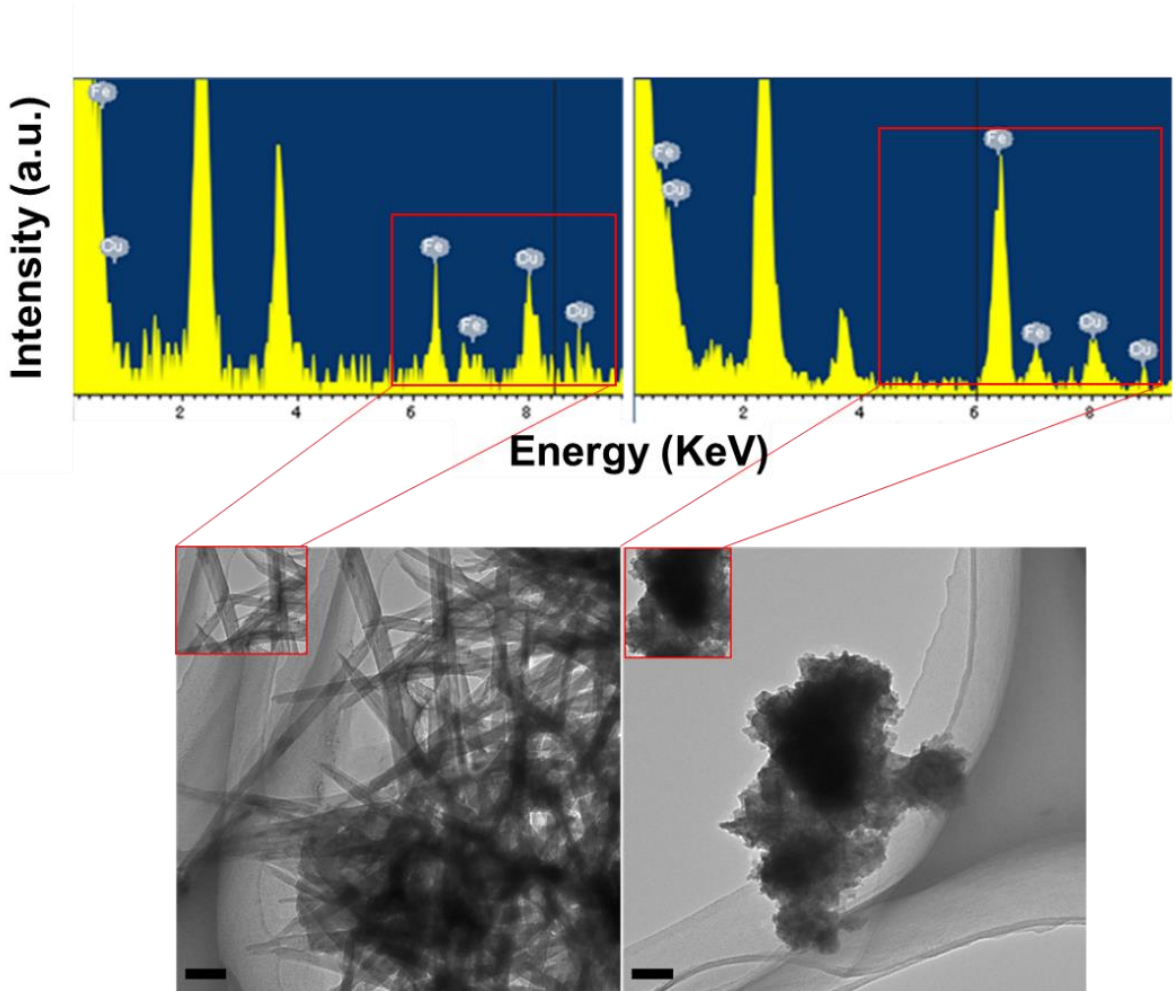

Figure 2.11. EDS and TEM (above and below) images of sample_1/3. Inset TEM image rod like shape (left) and aggregated part (right). Scale bar is 100 nm.

Table 2.3. ICP-OES and EDS determined atomic compositions for nanoparticle samples.

Sample	Cu:Fe Input (mol %)	ICP-OES		EDS (%)		
		Cu (%)	Fe (%)	Cu (%)	Fe (%)	
Sample_7/3	70:30	77	23	82 ± 3	18 ± 3	
Sample_1/1	50:50	54	46	54 ± 1	46 ± 1	
Sample_1/3	30:70	36	64	51 ± 8	49 ± 8	Area 1
				20 ± 5	80 ± 5	Area 2

Chemical composition of the sampled NPs before and after was also investigated using SEM-EDS. It was found that atomic % of copper and iron after injection of iron precursor was 91 % and 9 %. Low iron atomic percent is may be due to removal of iron content during washing of the sampled NPs after iron precursor injection because iron precursor is soluble in methanol and is removed during washing.

2.6.3 Thermoelectric Properties

By using the TE voltage plots as shown in Figure 2.12, the *S* was calculated for each sample. We found that sample_10/0 (copper sulfide NPs) possesses average *S* of 22 µV/K, which is consistent with the reference value for closely related bulk materials such as *di* ($Cu_{1.8}S$) of about 10 µV/K.[21] For sample_7/3 the average *S* increases to 26 µV/K. The *S* then rises again for sample_1/1 to 43 µV/K and even higher for sample_1/3 at 203 µV/K. This trend is intriguing given the composition and crystalline properties of these materials. The *S* may remain the same however, if the crystalline phase is doped with a higher amount of iron in this case, since the *S* measurement is not very sensitive to the overall conductivity quality of the material. Although, we cannot rule out the possibility that the amorphous phase is contributing greatly to the *S*. Experimentally it is a great challenge to separate these two materials to definitively determine this, but a more controlled synthesis of the materials could reveal additional information, which is a part of our ongoing investigations.

All the samples show p-type conductivity, indicating that the major carrier in these semiconducting materials is holes, which is consistent with copper sulfide materials, but contrasts with the n-type conductivity of bulk chalcopyrite.[22] For example, bulk $CuFeS_2$ prepared by a PECS technique has a maximum *S* of nearly −600 µV/K at 325 K and is n-type[22], contrary to our own material. However, for chalcopyrite NPs with a size of 6.4 nm, the *S* was reported to be over 800 µV/K and p-type.[10] The primary difference between the materials

analyzed in this reported study and our own study versus bulk chalcopyrite is the nano-sized dimension of the particles. The nano-scale size of the particles used to make the TE material causes several effects. First, there is a very high degree of particle surface interfaces, and two the small particle size leads to the observation of quantum confinement effects.[10] The very high degree of interparticle surface area can affect the *S* by creating a unique local surface composition, for example by being sulfur rich or sulfur deficient.[10] However, the quantum confinement effect may prove to have an even larger impact on the *S* (and other properties) because it will directly alter the electronic properties of the NPs themselves, which is responsible for governing not only *S*, but σ as well. While we cannot isolate these phenomena at this time, our results are consistent with past literature reports, and are the objective of part of our ongoing studies on this unique class of sustainable energy material.

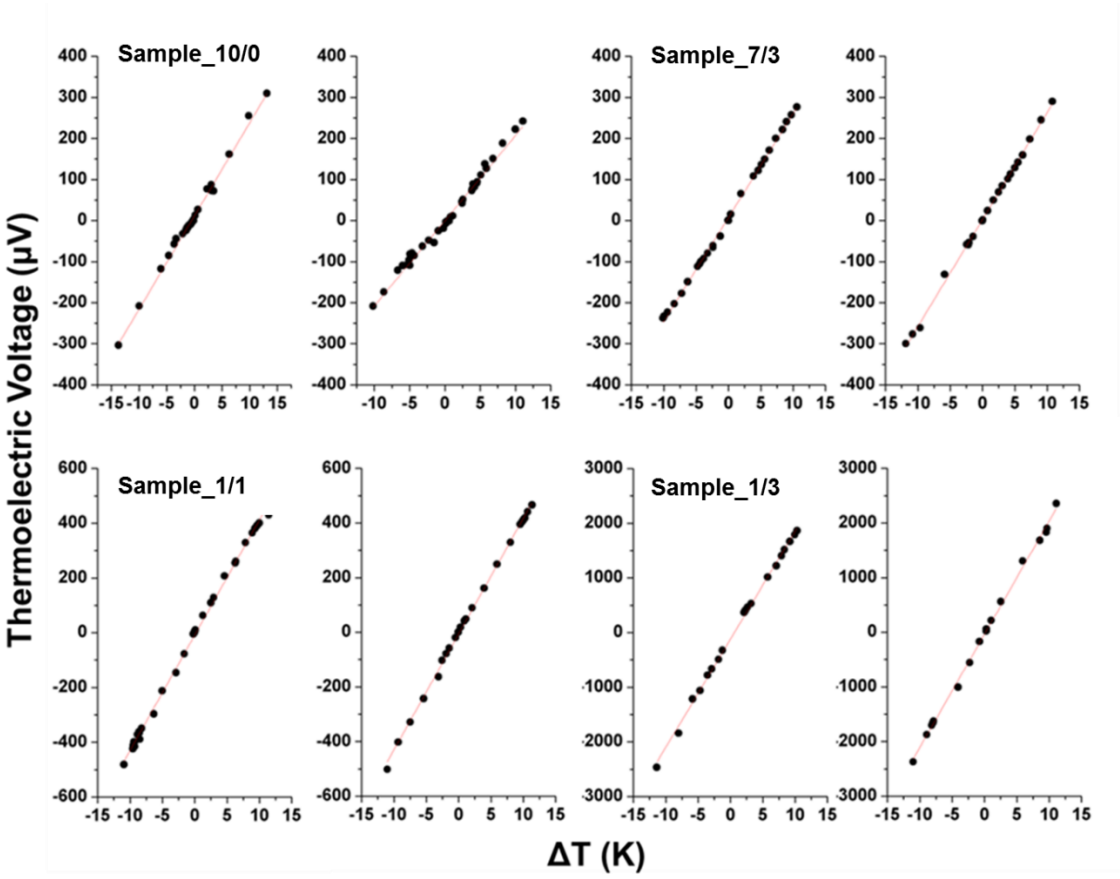

Figure 2.12. Seebeck measurement plots of all the samples

One of samples, sample_1/1 was analyzed using STEM-HAADF as shown in the Figure 2.13 which is clearly showing that sample_1/1 is not very dense. Voids can be seen in the STEM-HAADF image which is not suitable for σ measurements of the pelletized samples.

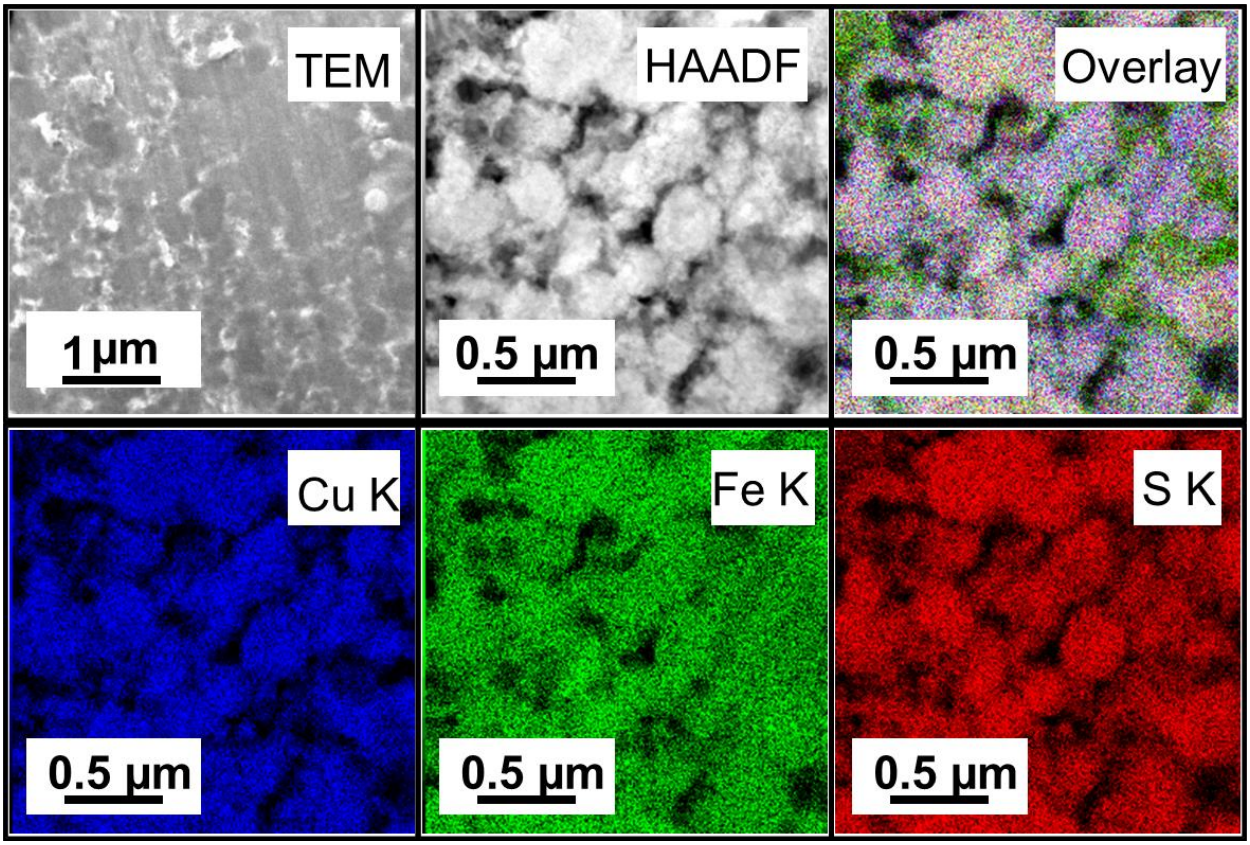

Figure 2.13. STEM-HAADF and elemental mapping images for sample_1/1

This synthetic protocol is not suitable for fabricating Cu-Fe-S NP system, as it is difficult to control the composition, size and shape of the NPs. Thus new synthetic technique has to be devised in which shape, size and composition can be controlled.

2.7 Conclusions

In conclusion, we have reported the synthesis and characterization of a sustainable chalcopyrite based NPs system for low temperature TE. XRD analysis for these samples shows

that the NPs exhibit a phase transition from cubic to tetragonal as the amount of iron is increased in the particles. Compositional analysis shows that the particles contain a composition representative of the feeding ratio, proving that the particle composition can be reliably controlled. The straightforward pellet preparation used in this study allows for the true nanoparticle size to be retained in the TE materials. Finally, the room temperature *S* was measured for each sample and was found to be p-type for each with a maximum value of 203 μV/K for the highest iron content, which is attributed to the high degree of interparticle interfaces and quantum confinement effects arising from the nanoparticle size. The results give insight and provide information into how NPs preparation and processing techniques can be harnessed to create TE materials with tunable and enhanced characteristics.

References

(1) Yaldagard, M.; Jahanshahi, M.; Seghatoleslami, N., Carbonaceous Nanostructured Support Materials for Low Temperature Fuel Cell Electrocatalysts—A Review. *World J. Nano Sci. Eng.* **2013**, *3*, 121-153.

(2) Guo, C. F.; Sun, T.; Cao, F.; Liu, Q.; Ren, Z. Metallic Nanostructures for Light Trapping in Energy-Harvesting Devices. *Light Sci. Appl.* **2014**, *3*, e161.

(3) Okada, T.; Saiki, T.; Taniguchi, S.; Ueda, T.; Nakamura, K.; Nishikawa, Y.; Iida, Y. Hydrogen Production Using Reduced Iron Nanoparticles by Laser Ablation in Liquids. *ISRN Renew. Energy* **2013**, *2013*.

(4) Kishore, S.; Nelson, J. A.; Adair, J. H.; Eklund, P. C. Hydrogen Storage in Spherical and Platelet Palladium Nanoparticles. *J. Alloy Compd.* **2005**, *389*, 234-242.

(5) Zhang, Y.; Wang, H.; Kraemer, S.; Shi, Y.; Zhang, F.; Snedaker, M.; Ding, K.; Moskovits, M.; Snyder, G. J.; Stucky, G. D. Surfactant-Free Synthesis of Bi_2Te_3−Te Micro−Nano Heterostructure with Enhanced Thermoelectric Figure of Merit. *ACS Nano* **2011**, *4*, 3158-3165.

(6) Poudel, B.; Hao, Q.; Ma, Y.; Lan, Y.; Minnich, A.; Yu, B.; Yan, X.; Wang, D.; Muto, A.; Vashaee, D. High-Thermoelectric Performance of Nanostructured Bismuth Antimony Telluride Bulk Alloys. *Science* **2008**, *320*, 634-638.

(7) Heremans, J. P.; Jovovic, V.; Toberer, E. S.; Saramat, A.; Kurosaki, K.; Charoenphakdee, A.; Yamanaka, S.; Snyder, G. J. Enhancement of Thermoelectric Efficiency in PbTe by Distortion of the Electronic Density of States. *Science* **2008**, *321*, 554-557.

(8) Gonçalves, A. P.; Godart, C. New Promising Bulk Thermoelectrics: Intermetallics, Pnictides and Chalcogenides. *Eur. Phys. J. B* **2014**, *87*.

(9) Zhao, L.-D.; Hao, S.; Lo, S.-H.; Wu, C.-I.; Zhou, X.; Lee, Y.; Li, H.; Biswas, K.; Hogan, T. P.; Uher, C. High Thermoelectric Performance via Hierarchical Compositionally Alloyed Nanostructures. *J. Am. Chem. Soc.* **2013**, *135*, 7364-7370.

(10) Liang, D.; Ma, R.; Jiao, S.; Pang, G.; Feng, S. A Facile Synthetic Approach for Copper Iron Sulfide Nanocrystals with Enhanced Thermoelectric Performance. *Nanoscale* **2012**, *4*, 6265-6268.

(11) Ge, Z.-H.; Zhang, B.-P.; Chen, Y.-X.; Yu, Z.-X.; Liu, Y.; Li, J.-F. Synthesis and Transport Property of $Cu_{1.8}S$ as a Promising Thermoelectric Compound. *Chem. Commun*. **2011**, *47*, 12697-12699.

(12) Mott, D.; Yin, J.; Engelhard, M.; Loukrakpam, R.; Chang, P.; Miller, G.; Bae, I.-T.; Das, N. C.; Wang, C.; Luo, J. From Ultrafine Thiolate-Capped Copper Nanoclusters toward Copper Sulfide Nanodiscs: A Thermally Activated Evolution Route. *Chem. Mater*. **2010**, *22*, 261-271.

(13) Li, S.; Wang, H. Z.; Xu, W. W.; Si, H. L.; Tao, X. J.; Lou, S.; Du, Z.; Li, L. S. Synthesis and Assembly of Monodisperse Spherical Cu_2S Nanocrystals. *J. Colloid Interf. Sci*. **2009**, *330*, 483-487.

(14) Suekuni, K.; Tomizawa, Y.; Ozaki, T.; Koyano, M. Systematic Study of Electronic and Magnetic Properties for $Cu_{12-X}Tm_xSb_4S_{13}$ (TM = Mn, Fe, Co, Ni, and Zn) Tetrahedrite. *J. Appl. Phys*. **2014**, *115*.

(15) Sigman, M. B.; Ghezelbash, A.; Hanrath, T.; Saunders, A. E.; Lee, F.; Korgel, B. A. Solventless Synthesis of Monodisperse Cu_2S Nanorods, Nanodisks, and Nanoplatelets. *J. Am. Chem. Soc*. **2003**, *125*, 16050-16057.

(16) Zhuang, Z.; Peng, Q.; Zhang, B.; Li, Y. Controllable Synthesis of Cu_2S Nanocrystals and Their Assembly into a Superlattice. *J. Am. Chem. Soc*. **2008**, *130*, 10482-10483.

(17) Li, F.; Wu, J.; Qin, Q.; Li, Z.; Huang, X. Controllable Synthesis, Optical and Photocatalytic Properties of CuS Nanomaterials with Hierarchical Structures. *Powder Technol.* **2010**, *198*, 267-274.

(18) Kumar, P.; Gusain, M.; Kumar, P. S.; Uma, S.; Nagarajan, R. A Simple One Pot Synthesis of Cubic Cu_5FeS_4. *RSC Adv*. **2014**, *4*, 52633-52636.

(19) Kumar, P.; Uma, S.; Nagarajan, R. Precursor Driven One Pot Synthesis of Wurtzite and Chalcopyrite $CuFeS_2$. *Chem. Comm*. **2013**, *49*, 7316-7318.

(20) Reference pattern accessed from the International Centre for Diffraction Data database 2013, card number 00-001-0842 for tetragonal $CuFeS_2$, card number 01-073-1667 for cubic Cu_5FeS_4, card number 01-081-1378 for cubic $CuFe_2S_3$ and card number 00-004-0861 for cubic $Cu_{1.8}S$, card number 00-029-0581 for rhombohedral beta-CuSCN, card number 00-036-0380 for hexagonal $Cu_{39}S_{28}$.

(21) Mansour, B.A. Electrical and Thermoelectric Properties of In and Cd Doped $Cu_{1.8}S$. *Phys. Status Solidi A* **1993**, *136*, 153-159.

(22) Li, J.; Tan, Q.; Li, J. F. Synthesis and Property Evaluation of $CuFeS_{2-x}$ as Earth-Abundant and Environmentally-Friendly Thermoelectric Materials. *J. Alloy Compd.* **2013**, *551*, 143-149.

Chapter 3: Colloid Chemical Approach for Fabricating Cu-Fe-S Nanobulk Thermoelectric Materials by Blending Cu_2S and FeS Nanoparticles as Building Blocks

3.1 Abstract

In the previous chapter it was found that it was very difficult to control the shape, size and composition of Cu-Fe-S NPs fabricated using polyol method. For this synthetic method for fabrication of Cu-Fe-S NPs has been changed to have better control over shape, size and composition. In the literature, $CuFeS_2$ TE material has been fabricated using Cu, Fe and S powders by rapid thermal explosion method in which all the elemental powder are ignited at once. During the process, formation of Cu_2S was observed which further reacts with Fe and S powders to give $CuFeS_2$ material. With this idea, colloidal chemical method was employed fabrication of Cu-Fe-S nanobulk material using liquid blend of different volume ratios of copper sulfide and iron sulfide nanoparticles which on further sintering using PECS to give bulk nanomaterial with ingrown nanoinclusions.

3.2 Introduction

A significant amount of energy is lost as waste heat, and thus tremendous effort has been devoted to develop efficient energy harvesting and conversion technologies. TE generators are one of the most promising devices to recycle waste heat because of their beneficial properties, such as light weight, no moving parts, and low noise.[1,2] TE generators are typically composed of p- and n-type semiconductors (thermoelectric materials). The performance of a TE material is quantified by the dimensionless figure of merit: $ZT = \sigma S^2 T/\kappa$. For practical energy harvesting applications, enhancing the ZT values of both p- and n-type TE materials composed of earth-abundant low-toxic elements below ~600 K is a major challenge.[3]

It has been reported that composite TE materials with nanoinclusions (or nanoprecipitates) are promising to enhance the *ZT* value because they exhibit significantly reduced κ_{lat} while maintaining their electrical transport properties and/or enhanced thermoelectric power factor (PF = σS^2) by three-dimensional modulation doping. For example, the κ_{lat} values of Na-doped PbTe–PbS,[4] Na-doped PbTe–SrTe[5] and Na-doped PbTe–MgTe[6] TE materials are effectively reduced because these systems are not only nanostructured but also have nanoprecipitates (PbS, SrTe or MgTe) embedded throughout the PbTe matrix. Chen and co-workers[7] demonstrated that the PF of a uniform p-type $Si_{86}Ge_{14}B_{1.5}$ sample can be significantly enhanced by the three-dimensional modulation-doping approach. Modulation doping is widely used in thin-film semiconductors to increase the σ value by increasing the carrier mobility μ because of spatial separation of the charge carriers from the dopants.[7] They fabricated modulation-doped $Si_{86}Ge_{14}B_{1.5}$ samples composed of two types of nanograins (doped Si nanograins and intrinsic $Si_{80}Ge_{20}$ grains). The charge carriers can separate from the doped Si nanograins and move into the undoped $Si_{80}Ge_{20}$ grains, which results in enhanced mobility of the carriers compared with uniform doping or normal doping owing to the reduction in ionized impurity scattering. Consequently, the σ of the two-phase composite can exceed those of the individual components, leading to a higher PF. He and co-workers[8] reported that the *ZT* value of the p-type BiCuSeO system can be improved by three-dimensional modulation doping. They fabricated a modulation-doped $Bi_{0.875}Ba_{0.125}CuSeO$ sample in which heavily doped $Bi_{0.75}Ba_{0.25}CuSeO$ nanograins are incorporated into an undoped BiCuSeO matrix. Comparing the carrier concentration *n* and μ values of modulation-doped $Bi_{0.875}Ba_{0.125}CuSeO$ with those of uniformly doped $Bi_{0.875}Ba_{0.125}CuSeO$, they found that the carriers preferentially transport in the undoped BiCuSeO region in the modulation-doped sample, resulting in higher μ compared with the uniformly doped sample even though the *n* values of both samples are almost identical. In normal doping or uniform doping the charge carriers are uniformly embodied in a material

and have high charge carrier scattering leading to low carrier mobility of charge carriers where as in modulation doping the dopants are non-uniformly distributed throughout the material. Because of the fermi level imbalance between host and guest material, the charge carriers are separated from the dopants leading to high carrier mobility because of low charge carrier scattering or ionized impurity scattering.[8]

Recently, to improve the *ZT* value of $Cu_2Sn_{1-x}Zn_xS_3$ nanobulk materials, we fabricated blended $Cu_2Sn_{1-x}Zn_xS_3$ nanobulk materials by sintering a mixture of chemically synthesized $Cu_2Sn_{0.85}Zn_{0.15}S_3$ (high σ and high κ) and $Cu_2Sn_{0.9}Zn_{0.1}S_3$ (low σ and low κ) nanoparticles as dense bulk materials by the PECS technique using $Cu_2Sn_{0.85}Zn_{0.15}S_3$ as the host material and $Cu_2Sn_{0.9}Zn_{0.1}S_3$ as nanoinclusions.[9] By blending these two heterogeneous (but nearly identical) nanoparticles in a weight fraction of 9:1 to fabricate a nanobulk material, the resulting pellet has *ZT* = 0.64 at 670 K, which is 1.7 and 1.9 times higher than the *ZT* values of the pristine $Cu_2Sn_{0.85}Zn_{0.15}S_3$ and $Cu_2Sn_{0.9}Zn_{0.1}S_3$ nanobulk materials, respectively.

Cu–Fe–S semiconductors, including *cp*,[10–14] *cb*,[15–17] and *bn*,[18–20] are earth-abundant low-toxicity thermoelectric materials. In addition, the Cu–Fe–S system can be either a p- or n-type semiconductor depending on the composition.[14,15,19] Despite their promising properties, such as low band gap energies and relatively high *S* values, the *ZT* values of Cu–Fe–S semiconductors are not very high, mainly because of their low PF values (0.38 mW mK^{-2} at 625 K for *cp*,[11] 0.48 mW mK^{-2} at 663 K for *cb*,[15] and 0.23 mW mK^{-2} at 663 K for *bn*[20]). Moreover, Cu–Fe–S thermoelectric materials are mostly synthesized by vacuum melting or mechanical alloying, which are high-energy time-consuming processes. In addition, multiscale defect engineering and interfacial modification to enhance the PF and κ_{lat} are inherently difficult for Cu–Fe–S materials using these processes.

In this study, we fabricated Cu–Fe–S nanobulk TE materials by sintering a mixture of chemically synthesized Cu_2S and FeS nanoparticles into dense bulk materials by the PECS

technique. Cu_2S and FeS nanoparticles were blended in the liquid phase to form a homogeneous mixture. The n- and p-type of the resulting Cu–Fe–S nanobulk material can be readily tuned by changing the volume ratio of the Cu_2S and FeS nanoparticles. Therefore, p- and n-type TE materials can be individually prepared by just changing the Cu_2S/FeS blending ratio. In addition, the spontaneously formed minor phases in the nanobulk material can act as nanoinclusions to effectively enhance the *ZT* value of the Cu–Fe–S TE material.

3.3 Materials

List of the chemicals used for the fabrication of Cu-Fe-S nanobulk samples is shown in Table 3.1. All the chemicals have been used as received without further purification.

Table 3.1. List of the chemicals, their chemical formula or abbreviation, and purity %.

Chemicals	Chemical Formula / Abbreviation	Purity %
Copper acetyl acetonate	$Cu(C_5H_7O_2)_2$ / $Cu(acac)_2$	99.9
Iron acetyl acetonate	$Fe(C_5H_7O_2)_3$ / $Fe(acac)_3$	99.9
1-Dodecanethiol	$CH_3(CH_2)_{11}SH$ / DDT	98.0
Thiourea	$SC(NH_2)_2$	99.0
Oleylamine	$C_{18}H_{35}NH_2$ / OAM	70.0
Methanol	CH_3OH	99.8
Ethanol	C_2H_5OH	99.5
Toluene	C_7H_8	99.5
Hexane	C_6H_{14}	96.0

3.4 Experimental

3.4.1 Synthetic Technique for Cu_2S and FeS Nanoparticles

Cu_2S NPs were synthesized with a heat-up method. Briefly, 40 mmol of $Cu(acac)_2$ and 240 mL of DDT were put into a three-necked flask equipped with a dry Ar inlet/outlet, trap sphere, condenser, heating mantle, thermometer, and magnetic stirrer. First, the reaction mixture was stirred with Ar bubbling at room temperature for 5 min. Then the temperature was increased to 80 ºC and kept for 30 min with Ar bubbling to remove volatile matter and dissolve $Cu(acac)_2$. Subsequently, the reaction temperature was further raised to 220 ºC and kept for 2 h. After the reaction, the mixture was cooled to room temperature (crude Cu_2S). General synthetic technique for copper sulfide NPs is shown in Scheme 3.1.

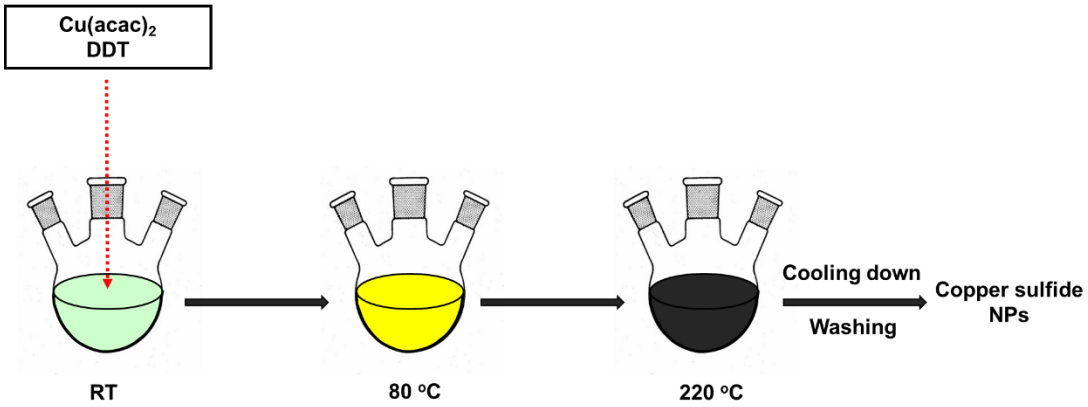

Scheme 3.1. General synthetic scheme for Cu_2S NPs.

FeS NPs were also synthesized in the same manner as the case of Cu_2S nanoparticles. 20 mmol of $Fe(acac)_3$, 40 mL of DDT and 80 mL of OAM were put into a three-necked flask, and then, the reaction mixture was stirred with Ar bubbling at room temperature for 5 min. Immediately after that, the temperature was increased to 80 ºC and kept for 30 min with Ar bubbling to remove volatile matter and dissolve $Fe(acac)_3$. Subsequently, the reaction temperature was further raised to 220 ºC and kept for 2 h. After the reaction, the mixture was

cooled to room temperature (crude FeS). General synthetic technique for iron sulfide NPs is shown in Scheme 3.2.

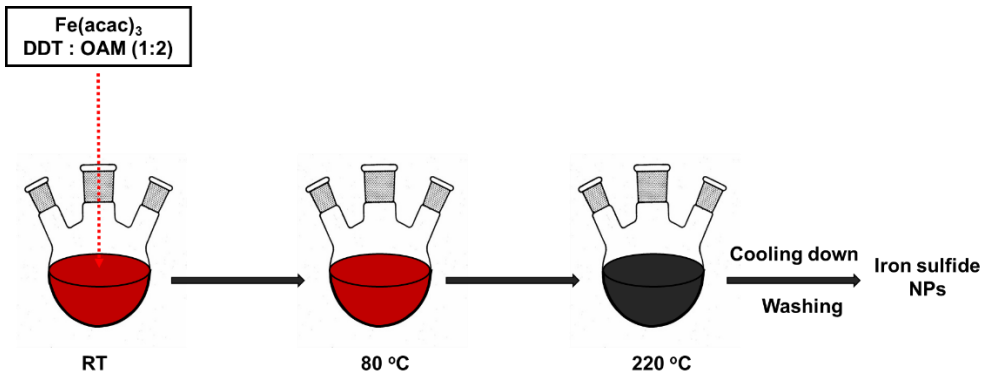

Scheme 3.2. General synthetic scheme for FeS NPs.

3.4.2 Preparation of Blended Powders

To prepare the powder for making a pellet, crude Cu_2S and crude FeS were mixed so as to the volume ratio between Cu_2S and FeS NPs (V_{Cu_2S}/V_{FeS}) in the powder becomes to be a desired value. Table 3.2 shows the relation between V_{Cu_2S}/V_{FeS} and the weight fractions of Cu_2S (φ) and FeS ($1-\varphi$) in the powder. In the present study, 6 powder samples with different V_{Cu_2S}/V_{FeS}=100/0, 90/10, 75/25, 50/50, 25/75 and 0/100 were prepared. These powder samples are referred to as Powder_10/0, Powder_9/1, Powder_3/1, Powder_1/1, Powder_1/3, and Powder_0/10, respectively (Table 3.2).

Table 3.2. Relation between V_{Cu_2S}/V_{FeS} and the weight fractions of Cu_2S (φ) and FeS ($1-\varphi$).

Sample name	V_{Cu_2S}/V_{FeS}	φ	$1-\varphi$
Powder_10/0	100/0	1.00	0
Powder_9/1	90/10	0.91	0.09
Powder_3/1	75/25	0.78	0.22
Powder_1/1	50/50	0.55	0.45
Powder_1/3	25/75	0.29	0.71
Powder_0/10	0/100	0	1.00

3.4.3 Ligand exchange of FeS and Cu_2S Nanoparticles

1.0 g of the powder was dispersed in 66 mL of toluene in a conical flask. In another flask, 2.7 g of thiourea was dissolved in 106 mL of methanol. Then, the methanol solution of thiourea was poured into the toluene dispersion of the NPs followed by sonication for 1 h. After the sonication, the NPs were separated from the mixture by centrifugation at 5000 rpm for 3 min. Then, the NPs were first washed by the following process: redispersion in hexane, centrifugation, and supernatant removal. Subsequently, 12 mL of methanol was added to the precipitates and the dispersion was sonicated for 10 min. After the sonication, the NPs were separated from the mixture by centrifugation at 5000 rpm for 5 min. Then, the NPs were washed four times by repeating the following purification cycle: redispersion in methanol, centrifugation, and supernatant removal to completely remove excess thiourea. Finally, 20 mL of toluene was added to the NPs followed by centrifugation at 5000 rpm for 10 min. The resulting powder sample was dried under vacuum.

3.5 Characterization Techniques

After synthesizing the NPs, next step is to characterize the NPs using various characterization techniques. A wide range of instruments were used in the characterization of the NPs studied here. The crystalline properties of the samples were analyzed by XRD with a Rigaku Miniflex instrument, Cu K_α radiation (λ= 0.15418 nm) at 30 kV and 15 mA over a 2θ range of 20-60°. TEM characterization was performed using a Hitachi H-7100 and H-7650 operating at 100 kV. Samples were prepared by drop-casting in a dilute solution of NPs in methanol/ toluene solution onto a Cu TEM grid (from Ted Pella). Sample composition was studied using inductively coupled plasma-optical emission spectroscopy (ICP-OES) using a Shimadzu ICPS-

7000 instrument. The accelerating voltage of the electron beam was 100 kV. Further these NPs samples were subjected to TE properties measurements.

After ligand exchange, the blended NPs were pelletized into a solid disk with a diameter of 10 mm and a thickness of 2–3 mm using a PECS machine (Sinterland LABOX-100) under the following conditions: atmosphere, vacuum; temperature, 450 °C; pressure, 30 MPa; and sintering time, 5 min. κ is measured using a technique called laser flash analysis (LFA) and *S*, electrical resistivity (ρ) is measured using ZEM-3 instrument.

3.6 Results and Discussion

3.6.1 Morphology and Crystal Structure

TEM images of the powder samples are shown in Figure 3.1. Both the Cu_2S (Powder_10/0, Figure 3.1a) and FeS (Powder_0/10, Figure 3.1f) nanoparticles are relatively uniform in size with a hexagonal platelet-like morphology. It is well known that Cu_2S nanoparticles have a hexagonal disk shape and are relatively stable at high temperatures.[21–23] For the FeS nanoparticles, some of the nanoparticles are standing up and others are lying down on the TEM grid (Figure 3.1f). The mean diameter and thickness of the Cu_2S nanoplatelets were calculated to be 15.1 ± 0.7 nm and 2.8 ± 0.4 nm, respectively. The average diameter and thickness of the FeS nanoplatelets were calculated to be 134.9 ± 24.1 nm and 13.5 ± 5.4 nm, respectively. The TEM images of the Powder_9/1, Powder_3/1, Powder_1/1, and Powder_1/3 blended samples show that the Cu_2S and FeS nanoplatelets are mixed to form blended powders.

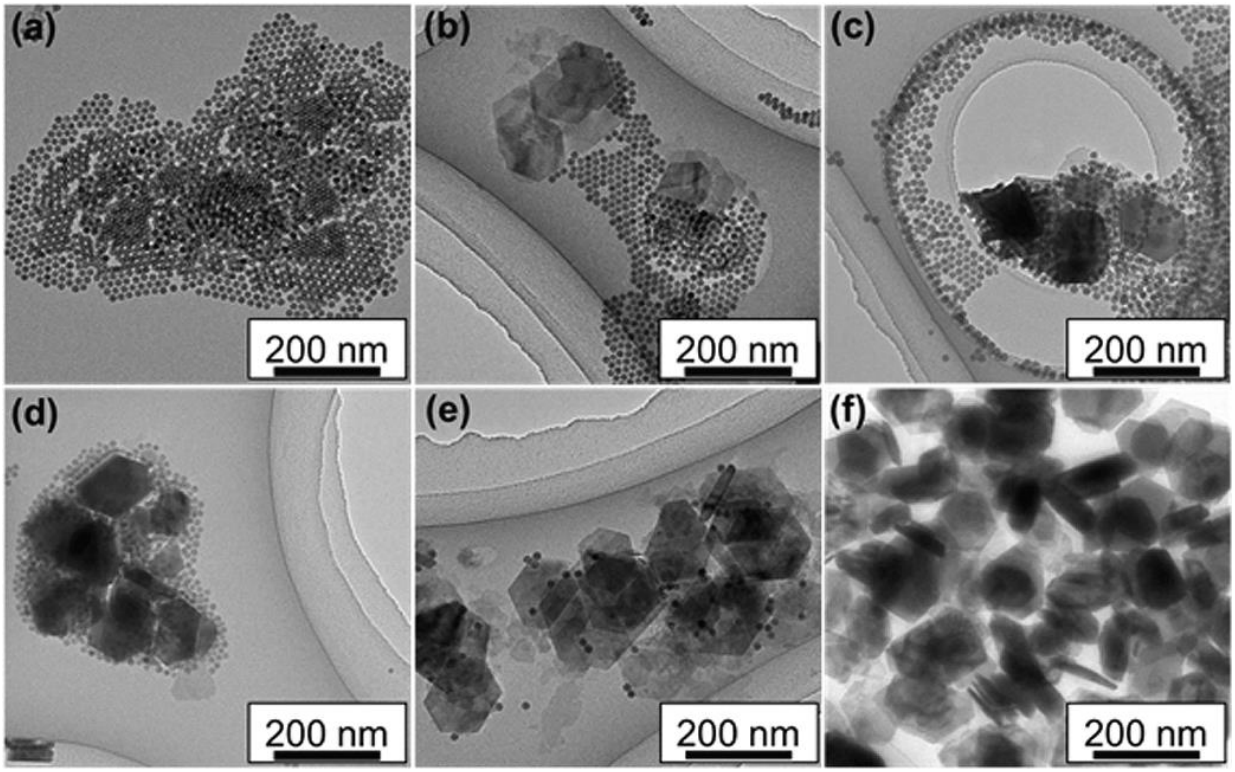

Figure 3.1. TEM images of (a) Powder_10/0, (b) Powder_9/1, (c) Powder_3/1, (d) Powder_1/1, (e) Powder_1/3, and (f) Powder_0/10 recorded before ligand exchange.

The XRD patterns of Powder_10/0, Powder_9/1, Powder_3/1, Powder_1/1, Powder_1/3, and Powder_0/10 recorded after ligand exchange are shown in Figure 3.2. The XRD patterns of Powder_10/0 and Powder_0/10 agree well with those of *cc* and troilite (*tr*, FeS), respectively. The relative intensity ratio of the XRD peaks of *cc* to *tr* systematically decreases with decreasing V_{Cu_2S}/V_{FeS}. The mean crystalline sizes (D_{XRD}) of *cc* and *tr* were calculated using Scherrer's equation based on the most intense diffraction peaks. The D_{XRD} values of Powder_10/0 and Powder_0/10 are 14 and 18 nm, respectively.

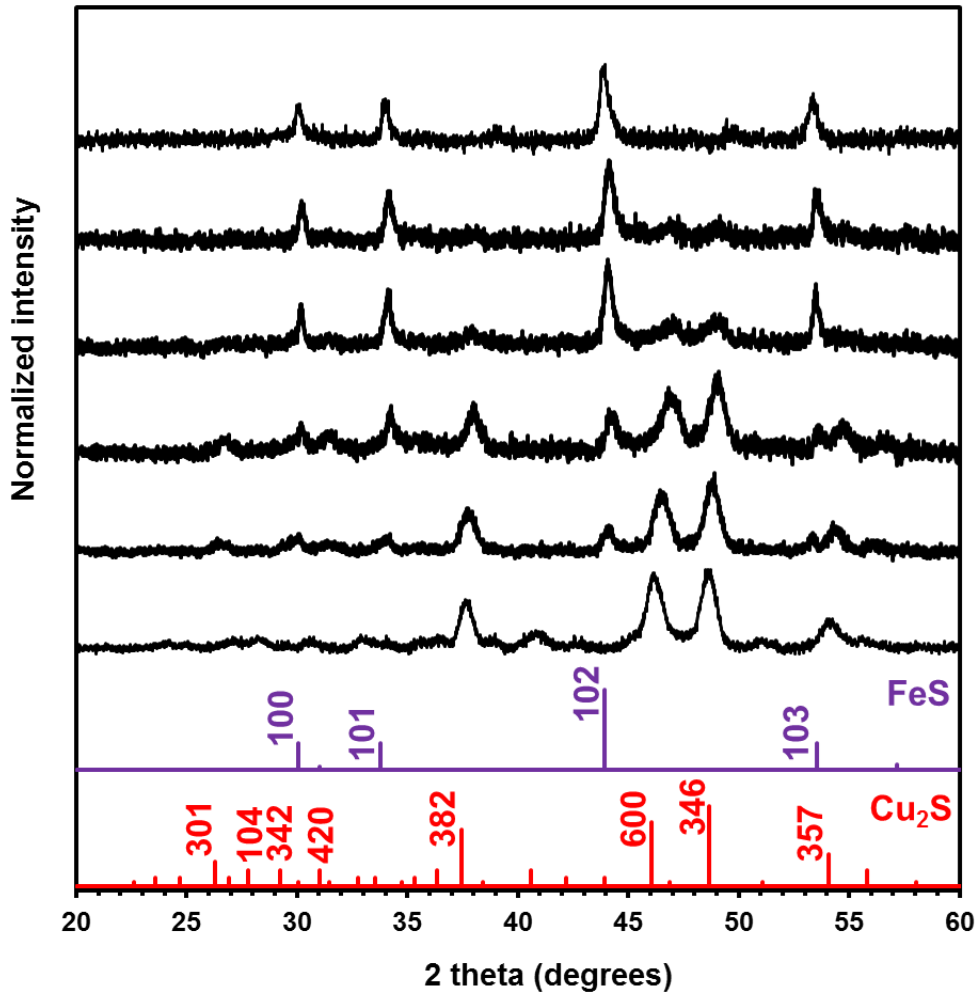

Figure 3.2. XRD patterns of Powder_10/0, Powder_9/1, Powder_3/1, Powder_1/1, Powder_1/3, and Powder_0/10 (from bottom to top). The red and purple lines correspond to the reference XRD patterns of chalcocite (Cu_2S, JCPDS PDF No. 00-009-0328) and troilite (FeS, JCPDS PDF No. 00-001-1247), respectively.

The XRD patterns of Pellet_10/0, Pellet_9/1, Pellet_3/1, Pellet_1/1, Pellet_1/3, and Pellet_0/10 recorded after the thermoelectric measurements are shown in Figure 3.3. The crystalline structure of Pellet_10/0 is *di*, which is a stable phase of the Cu–S system. During sintering by PECS, the *cc* phase becomes unstable and changes to the more stable *di* phase.[24] Cu_2S is a superionic conductor and shows a superionic phase transition above 689 K.[23,25] Therefore, excess Cu could have precipitated at the surface of the pellet during sintering at high temperature (>700 K), but it would have been removed during polishing.[23] For Pellet_0/10, the

crystalline structure is iron-deficient monoclinic pyrrhotite (*m-po*, Fe_7S_8) with a small amount of iron oxide. The existence of iron oxide is verified by peaks at $2\theta = 35.4°$ and 56.9°, which correspond to the XRD peaks of the (311) and (511) planes of iron oxide, respectively (Figure 3.3).

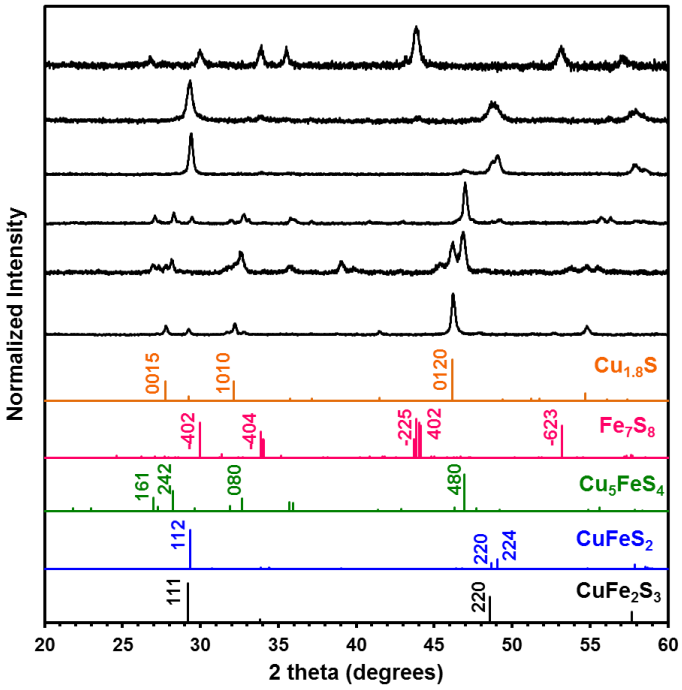

Figure 3.3. XRD patterns of Pellet_10/0, Pellet_9/1, Pellet_3/1, Pellet_1/1, Pellet_1/3, and Pellet_0/10 (from bottom to top). The reference XRD patterns of isocubanite ($CuFe_2S_3$, JCPDS PDF No. 01-081-1378), tetragonal chalcopyrite ($CuFeS_2$, JCPDS PDF No. 01-073-9964), bornite (Cu_5FeS_4, JCPDS PDF No. 00-042-1405), monoclinic pyrrhotite (Fe_7S_8, JCPDS PDF No. 01-074-7398), and digenite (Cu_9S_5, JCPDS PDF No. 00-047-1748) are shown by black, blue, green, pink, and orange lines, respectively.

To perform quantitative phase-composition analysis of the blended samples, Rietveld refinement of the XRD patterns of Pellet_9/1, Pellet_3/1, Pellet_1/1, and Pellet_1/3 was performed using the FullPROF program.[26] The Rietveld-refined XRD patterns are shown in Figure 3.4. Pellet_9/1 is a mixture of *bn*, nukundamite [*nu*, $(Cu,Fe)_4S_4$], *di*, roxbyite (*ro*, $Cu_{29}S_{16}$), and a small amount of CuO (Table 3.3). The volume percentages of the *bn*, *nu*, *di*,

ro, and CuO phases were calculated to be 89.0%, 8.9%, 1.1%, 0.1%, and 0.9%, respectively. For Pellet_3/1, *bn* is the main phase with some minor phases, such as *nu* and covellite (*co*, CuS) (Table 3.3). For Pellet_1/1, the main phase is *cp* and the secondary phase is *bn* (Table 3.3). The volume percentages of the *cp* and *bn* phases are 90% and 10%, respectively. For Pellet_1/3, the main phase is *cp* with the *m-po* secondary phase (Table 3.3). The volume percentages of the *cp* and *m-po* phases are 92% and 8%, respectively.

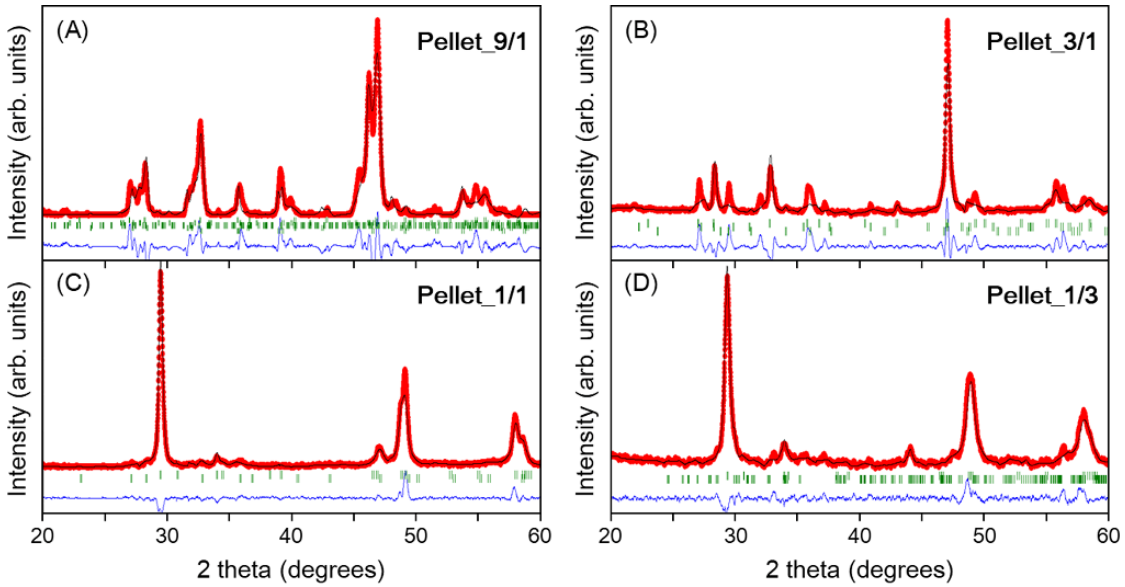

Figure 3.4. Rietveld refinement of the powder XRD patterns of (A) Pellet_9/1, (B) Pellet_3/1, (C) Pellet_1/1, and (D) Pellet_1/3. The experimental patterns are shown as red circles and the calculated patterns are shown as black lines. The χ^2 values are 3.87, 3.88, 2.08 and 1.19 for Pellet_9/1, Pellet_3/1, Pellet_1/1, and Pellet_1/3, respectively. The Bragg reflection positions are shown as short green bars below the diffraction patterns. The blue lines represent the difference patterns.

Table 3.3. Volume percentages of the phases determined by Rietveld analysis.

Pellet name	Main phase (vol %)	Minor/secondary phases (vol %)
Pellet_10/0	*di* (100)	–
Pellet_9/1	*bn* (89.0)	*nu* (8.9) + *di* (1.1) + *ro* (0.1) + CuO (0.9)
Pellet_3/1	*bn* (90.1)	*nu* (7.7) + *co* (2.2)
Pellet_1/1	*cp* (90)	*bn* (10)
Pellet_1/3	*cp* (92)	*m-po* (8)

Pellet_0/10	*m-po* (91)	Fe_3O_4 (9)

The D_{XRD} values of the main phases in Pellet_10/0, Pellet_9/1, Pellet_3/1, Pellet_1/1, Pellet_1/3, and Pellet_0/10 were calculated to be 18, 6, 9, 10, 18, and 18 nm, respectively. Interestingly, the Cu–Fe–S phases, such as *bn* and *cp*, have smaller D_{XRD} values than the Cu_2S and FeS nanoparticles, whereas the D_{XRD} values of the Cu–S (*di*) and Fe–S (*m-po*) phases are approximately the same as those of the Cu_2S and FeS nanoparticles, respectively. The mean crystalline size did not change much after PECS because of the fast heating and cooling rate. This advantage of PECS provides limited grain growth rate. The PECS technique is rapid densification technique which involves joules heating effect in the particles on application of electric DC pulse across the sample which causes diffusion of the atoms enhancing the growth of the particles. But due to short hold time and rapid cooling, this diffusion process is hampered and the grain growth is diminished. All of the crystalline phases in the samples are listed in Table 3.4.

Table 3.4. Crystal phases in the samples.

Chemical formula	Mineral name	Abbreviation	Type of carrier (bulk crystal)
Cu_2S	chalcocite	*cc*	P[27]
$Cu_{29}S_{16}$	roxbyite	*ro*	P[28]
Cu_9S_5	digenite	*di*	P[29]
CuS	covellite	*co*	P[30]
Cu_5FeS_4	bornite	*bn*	P[18] (n at low temperature)
$CuFeS_2$	chalcopyrite	*cp*	n[11]
$(Cu,Fe)_4S_4$	nukundamite	*nu*	N/A
Fe_7S_8	monoclinic pyrrhotite	*m-po*	P[31] (n at low temperature)

FeS	troilite	*tr*	P^{32} (metallic when $T > 420$ K)

XPS analysis for all the pellets are done to investigate phases present other than the crystalline phases which are not observed in the XRD are shown in Figure 3.5. Deconvolution of the Cu 2p, Fe 2p and S 2p are done using Gaussian-Lorentzian mixed function in XPSPEAK41 software. The Cu 2p spectra was deconvoluted with four different species: Cu^0, Cu^+, Cu^{2+} and satellite peak, the Fe 2p spectra was deconvoluted with five different species: Fe^0, Fe^{2+}, Fe^{3+} surface component and satellite peak.

In Pellet_10/0 (Figure 3.5 a), two XPS spectras Cu 2p and S 2p are shown. $Cu_{1.8}S$ as the main phase was observed in XRD pattern of this sample as shown in Table 3.3 and also confirmed from the Cu^+, Cu^{2+} and low binding energy value of 161.3 eV and 162.5 which correspond to S $2p_{3/2}$ and S $2p_{1/2}$ respectively. Presence of metallic Cu in the form of Cu^0 and SO_4^{2-} (~168 eV) species due to surface oxidation were also observed. These phases are probably amorphous in nature and could not be observed in XRD analysis.

Pellet_9/1 (Figure 3.5 b), three XPS spectras are Cu 2p, Fe2p and S 2p are shown. *bn* as the main phase along with the secondary phases such as *nu*, *di*, *ro*, CuO. *bn* ($Cu_4^+Cu^{2+}Fe^{2+}S_4$) has Cu^+, Cu^{2+}, Fe^{2+}, *nu* ($Cu_2^{2+}Fe_2^{2+}S_4$) has Cu^{2+}, Fe^{2+} species, *di* and *ro* has Cu^+, Cu^{2+} presence of all these species in the XPS spectra confirms the presence of *bn*, *di*, *nu* and CuO. Presence of Cu^0 and Fe^0 are also detected which was not observed in the XRD pattern of this sample and is probably in amorphous form. Pellet_3/1 (Figure 3.5 c), three XPS spectras are Cu 2p, Fe2p and S 2p are shown. *bn* as the main phase along with the secondary phases such as *nu*, *co*. *bn* has Cu^+, Cu^{2+}, Fe^{2+} and presence of all these species in the XPS spectra confirms the presence of *bn* and also *nu* and *co*. Presence of Cu^0 and Fe^0 are also detected which was not observed in the XRD pattern of this sample and is probably in amorphous form.

In Pellet_1/1 and Pellet_1/3, (Figure 3.5 d and e respectively) surface oxidation of S due to SO_4^{2-} species (~168 eV) was observed which was detected during XRD. In both the samples *cp* as the main phase was observed and Cu^{+}, Cu^{2+}, Fe^{2+}, Fe^{3+} species confirms the presence of *cp* and *bn* well in Pellet_1/1 and *m-po* in Pellet_1/3. Presence of Cu^0 and Fe^0 are also detected. In Pellet_0/10 (Figure 3.5 e), surface oxidation of S due to SO_4^{2-} species (~168 eV) was observed which was detected during XRD. Presence of Fe^0 was observed. Presence of Fe^{2+}, Fe^{3+} species corresponds to the main phase *m-po* and Fe_3O_4.

In addition, it is somehow difficult to differentiate between Cu^0 and Cu^{1+} because their binding energies are almost identical (~932 eV). So presence of Cu^0 species is doubtful. So without the presence of Cu^0 species atomic % of each species calculated from respective areas are shown for all the pellets in Table 3.5 and theoretical ratio of each species in all the samples are shown in Table 3.6. Theoretical ratio of each chemical species is calculated on the basis of the phases present in the respective pellet samples.

Table 3.5 XPS composition of each species (atomic %).

Pellet name	**Cu^{+}**	**Cu^{2+}**	**Fe^0**	**Fe^{2+}**	**Fe^{3+}**
Pellet_10/0	75	25			
Pellet_9/1	82	18	29	24	47
Pellet_3/1	79	21	12	42	46
Pellet_1/1	76	24	14	39	47
Pellet_1/3	93	7	18	47	35
Pellet_0/10			27	57	16

Table 3.6. Theoretical % of chemical species in all the samples.

	Cu^{+}	Cu^{2+}	Fe^{2+}	Fe^{3+}
Pellet_10/0	89	11	--	--
Pellet_9/1	85	15	67	33
Pellet_3/1	63	37	67	33
Pellet_1/1	100	--	--	100
Pellet_1/3	100	--	63	37
Pellet_0/10	--	--	60	40

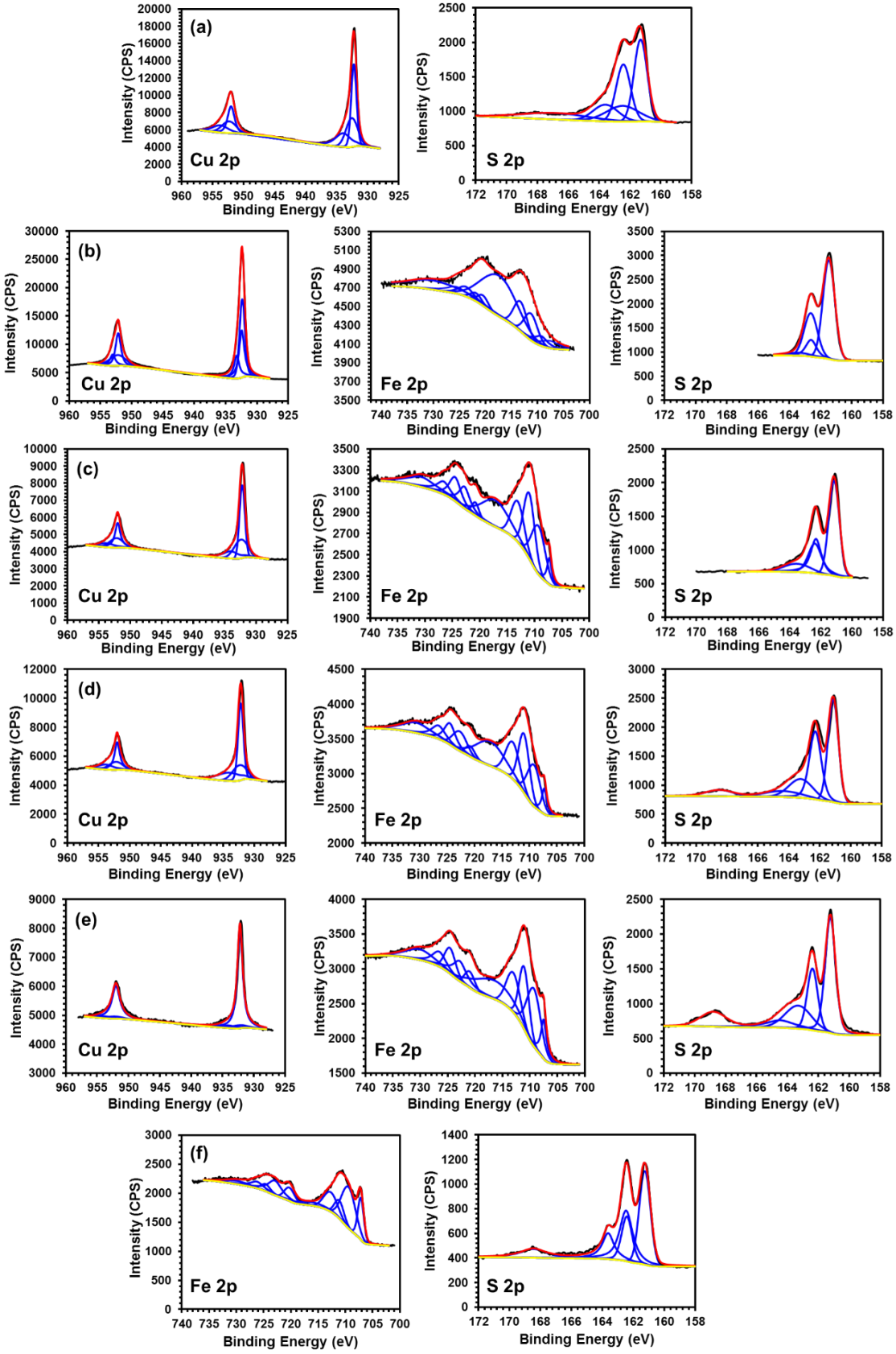

Figure 3.5. XPS patterns of (a) Pellet_10/0, (b) Pellet_9/1, (c) Pellet_3/1, (d) Pellet_1/1, (e) Pellet_1/3, and (f) Pellet_0/10.

3.6.2 Compositional Analysis.

The average composition of each sample was determined by ICP-OES [hereafter referred to as $(Cu/Fe)_{ICP}$]. The theoretical Cu/Fe atomic ratio in the sample [$(Cu/Fe)_{calc}$] was calculated from the V_{Cu_2S}/V_{FeS} value. For the pellets, cross-sectional HAADF-STEM and EDS elemental mapping analyses were also performed, as shown in Figure 3.5. The average Cu/Fe values calculated from EDS and quantitative Rietveld phase analysis are hereafter referred to as $(Cu/Fe)_{EDS}$ and $(Cu/Fe)_{XRD}$, respectively. The $(Cu/Fe)_{calc}$, $(Cu/Fe)_{ICP}$, $(Cu/Fe)_{EDS}$ and $(Cu/Fe)_{XRD}$ values agree relatively well (Table 3.6), indicating that the pellets are macroscopically homogeneous.

The internal nanostructures of the pelletized samples are characterized by the cross sectional TEM and STEM-HAADF as shown in Figure 3.7. It is clear that the microscopic compositional non-uniformity increases with decreasing V_{Cu_2S}/V_{FeS} (Figure 3.6). Combined with the XRD analyses, this result can be interpreted as follows: For Pellet_9/1 and Pellet_3/1, even though they are a mixture of several phases (Table 3.3), the compositional non-uniformity is not very pronounced because the Fe content in the pellet is relatively low and the mean size of the Cu_2S nanoplatelets is small (15 nm). Pellet_1/1 is a mixture of *cp* and *bn* and Pellet_1/3 is a mixture of *cp* and *m-po* (Table 3.3). Because the mean size of the FeS nanoplatelets (135 nm) is much larger than that of the Cu_2S nanoplatelets, the compositional inhomogeneity in the resulting pellets increases with decreasing V_{Cu_2S}/V_{FeS}.

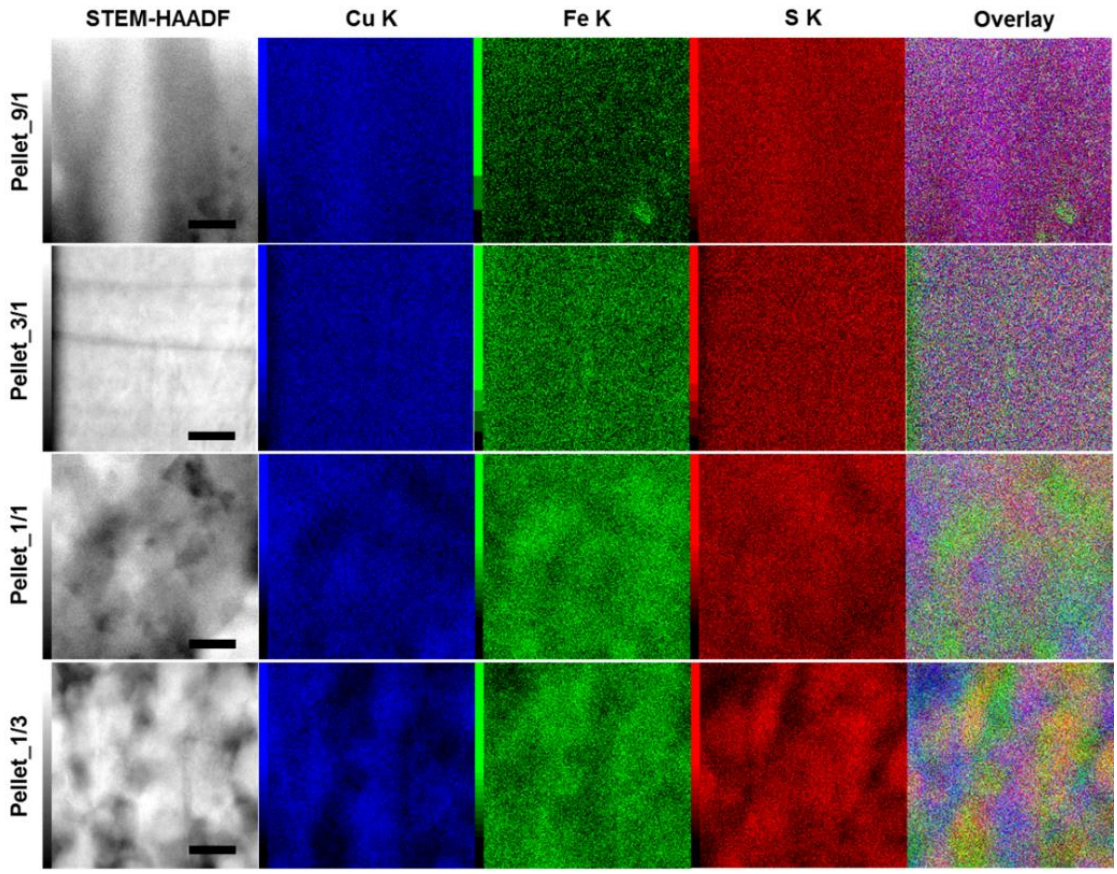

Figure 3.6. Cross-sectional HAADF-STEM and EDS elemental mapping images of Pellet_9/1, Pellet_3/1, Pellet_1/1, and Pellet_1/3 after the thermoelectric measurements (from top to bottom). The left column is the HAADF-STEM images, the second column from the left is the Cu K line, the middle column is the Fe K line, the second column from the right is the S K line, and the right column is the overlay. The scale bar is 30 nm.

Table 3.7. Cu/Fe atomic ratios in the blended samples.

Sample name	$(Cu/Fe)_{calc}$	$(Cu/Fe)_{ICP}$	$(Cu/Fe)_{EDS}$	$(Cu/Fe)_{XRD}$
Pellet_9/1	92/8	89/11	93(±6)/7(±6)	84/16
Pellet_3/1	80/20	80/20	79(±1)/21(±1)	84/16
Pellet_1/1	55/45	55/45	60(±2)/40(±2)	54/46
Pellet_1/3	30/70	30/70	40(±2)/60(±2)	46/54

It has been reported that PECS has the potential to form preferential crystal orientation perpendicular to the pressing axis[33] and/or compositional gradient along the pressing axis[34,35] which lead to the anisotropy of the transport properties. Because κ was measured for the pellet in the cross-plane direction while S and σ were measured in the in-plane direction, the isotropy

and homogeneity of the pellet is essential. In the cases of the blended samples, it is unlikely that the preferential orientation occurs during PECS, because *bn* and *cp* are cubic and tetragonal crystal systems, respectively, and the grain growth was suppressed as mentioned above. To find out if the compositional gradient along the pressing axis is formed, the composition of both surfaces of the pellet was measured by SEM-EDS. EDS spectra were obtained from eight randomly selected regions within one side of the pellet. Since no significant differences in the composition of both sides were detected, it is confirmed that the pellets were compositionally isotropic.

3.6.3 Thermoelectric Properties

The temperature dependence of the σ, S, PF, κ, κ_{lat}, and ZT values of all the pellets is shown in Figure 3.7. It should be noted that we measured the S and σ values during both the heating and cooling cycles, and the values are the same in both cycles, as shown in Figures 3.8 and 3.9. Therefore, only the values during the heating cycle are shown in Figure 3.7.

Thermogravimetric analysis (TGA) of thiourea capped nanoparticles were also done which shows that thiourea start to degrade above 140 ^{o}C into ammonium thiocyanate (NH_4SCN), NH_3, H_2S and carbodiimide (NH=C=NH) as shown in Figure 3.10. The melting point of thiourea is 184.5 ^{o}C.[36]

Pellet_10/0 shows very similar TE properties to those of non-nanostructured *di*, which is known to be a p-type degenerate semiconductor.[37] However, the σ value is significantly lower than that of non-nanostructured *di* (22,5000 S/m),[29] presumably because the relative density of the pellet is low and/or the Cu/S ratio in Pellet_10/0 is slightly larger than 1.8.[38]

For Pellet_9/1, the ZT value reaches 0.55 at 663 K, which is about 45% higher than that of non-nanostructured *bn* (ZT = 0.38 at 663 K),[18] even though the main phase is *bn* (Table 3.3). The κ value is almost the same as that of non-nanostructured *bn*. It is known that *bn* has intrinsic

ultralow κ (0.3 W m^{-1} K^{-1}). Therefore, the nanostructuring does not lead to a further reduction of κ_{lat}. In the present study, the *ZT* value of *bn* is increased to 0.55 (at 663 K) by increasing the PF while maintaining ultralow κ. Pellet_3/1 shows similar TE properties to those of non-nanostructured stoichiometric *bn*,[18,19] probably because the fraction of the *bn* phase in Pellet_3/1 is very high (Table 3.3) and the *bn* phase could be nearly stoichiometric. One possible reason for the enhanced figure of merit of Pellet_9/1 is the off-stoichiometry of the *bn* phase and the resulting higher PF. It has been reported that the *S* value of the stoichiometric *bn* phase is very large, while the σ value is relatively low (ca. 5.0 S m^{-1} at 300 K) because of its low carrier concentration (1.7 × 10^{16} cm^{-3} at 300 K). However, the σ value can be greatly enhanced by tuning the off-stoichiometry. In fact, slightly off-stoichiometric *bn* with richer Cu and poorer Fe contents ($Cu_{5.04}Fe_{0.96}S_4$) has a 2–3 orders of magnitude higher σ value than that of stoichiometric *bn* by creating more hole carriers, while the *S* value of slightly off-stoichiometric *bn* is as high as that of stoichiometric *bn*. As a result, the *ZT* value of $Cu_{5.04}Fe_{0.96}S_4$ reaches 0.5 at 663 K.[18] However, even if that is the case, the off-stoichiometry of the *bn* phase in Pellet_9/1 is small because no significant shift of the XRD peaks was observed for the *bn* phase in Pellet_9/1.

Another possible reason for the enhanced *ZT* of Pellet_9/1 is three-dimensional modulation doping.[7,8,39] It is possible that the carriers diffuse from the *di* and/or other minor phases (high *n*) to the *bn* phase (low *n*) in Pellet_9/1. For example, the *n* values have been reported to be 4.5 × 10^{20} to 3.0 × 10^{21} cm^{-3} for *di*[40] and 3.3 × 10^{21} cm^{-3} for *ro*.[28] The Fermi level of pristine *bn* is thought to be located between the conduction and valence bands, while it exists in the valence band for *di*. Since *bn* is an intrinsic semiconductor (undoped) and for intrinsic semiconductors the Fermi level lies in between the conduction band and valence band[41] whereas *di* is p-type semiconductor and for p-type semiconductors, the Fermi level lies within the valence band[42]. This Fermi level imbalance between *bn* and *di* can lead to modulation doping. After performing

Hall measurement for Pellet_9/1, the n is 3.1×10^{21} cm^{-3} at 300 Kwhich is much higher than reported for pristine *bn* (1.7×10^{16} cm^{-3} at 300 K).[18]

Pellet_1/1 and Pellet_1/3 show n-type semiconductor behavior. This is consistent with the fact that the main phase in these pellets is *cp*, which is an n-type semiconductor. It has been reported that the carrier concentration of $Cu_{1-x}Fe_{1+x}S_2$ can be tuned within a wide range by varying x. For example, $n = 0.34 \times 10^{20}$ cm^{-3} when $x = 0$, while $n = 7.02 \times 10^{20}$ cm^{-3} when $x = 0.1$.[12] Therefore, both the S and σ values can vary widely even if the XRD pattern remains virtually unchanged. The ZT values of Pellet_1/1 and Pellet_1/3 were calculated to be 0.06 and 0.08 (at 663 K), respectively. These values are less than half of the ZT value of non-nanostructured *cp* (ZT = 0.18 at 663 K).[12] This is presumably because of the existence of another phase (*bn* or *m-po*) and/or nanostructuring decreasing not only κ_{lat} but also σ, resulting in lower PF. Note that the κ value of non-nanostructured $Cu_{1-x}Fe_{1+x}S_2$ is as high as 1–2 W m^{-1} K^{-1}.[12] Pellet_0/10 shows metallic behavior, as expected from the carrier transport properties of *m-po*.[31] It is evident in Figure 3.6e, where κ_{lat} of Pellet_0/10 exhibits the classical $1/T$ dependence caused by Umklapp scattering, while the characteristic $1/T$ dependence of κ_{lat} disappears in the cases of the blended samples (Pellet_9/1, Pellet_3/1, Pellet_1/1 and Pellet_1/3) supporting the fact that the phonon scattering is dominated by defect scattering.

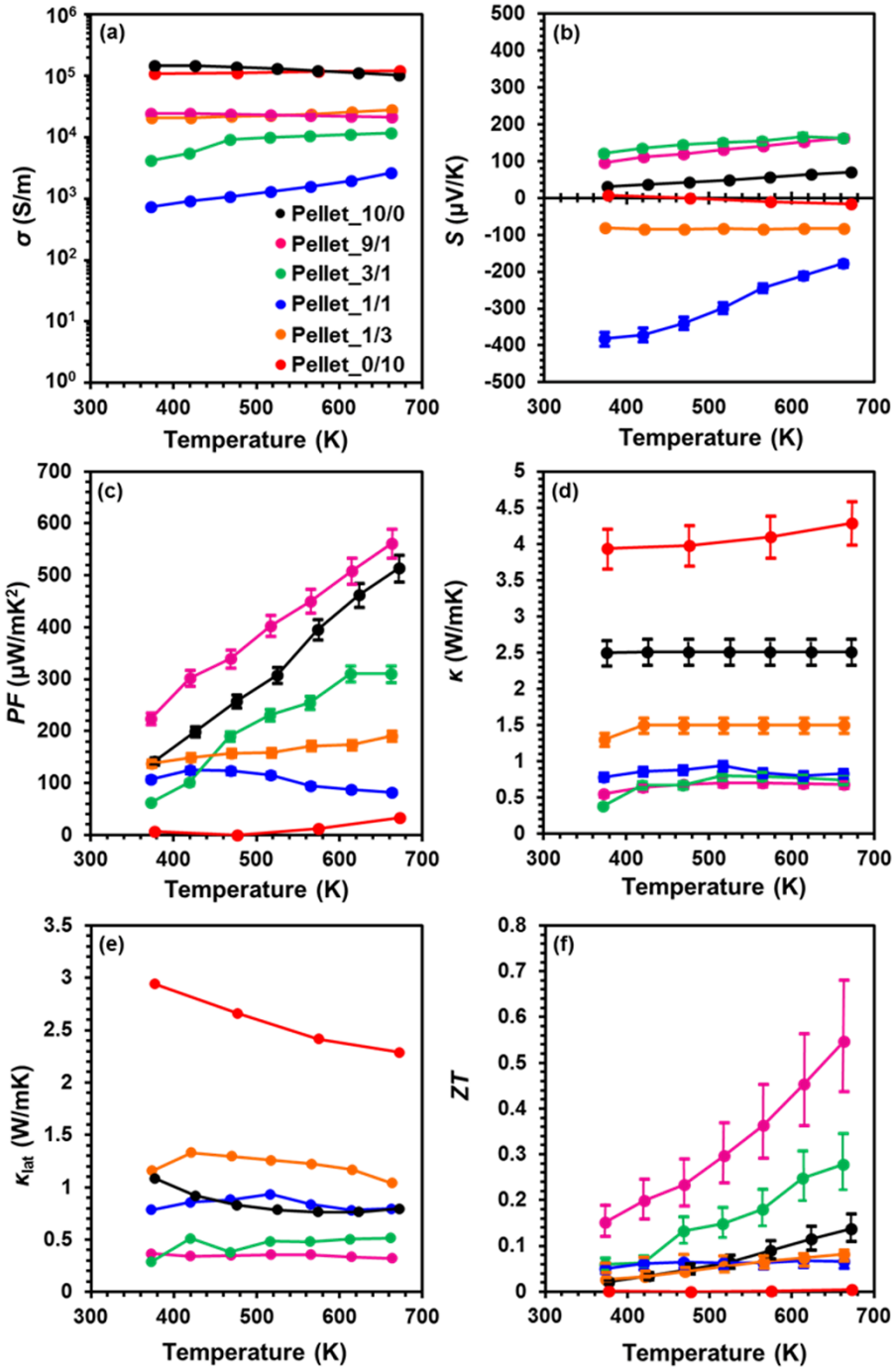

Figure 3.7. Temperature dependence of the (a) σ, (b) S, (c) PF, (d) κ, (e) κ_{lat}, and (f) ZT values for all of the pellets. Black, pink, green, blue, orange, and red are the data for Pellet_10/0, Pellet_9/1, Pellet_3/1, Pellet_1/1, Pellet_1/3, and Pellet_0/10, respectively. It should be noted that we measured the S and σ values during both the heating and cooling cycles and the values were the same. Therefore, only the values during the heating cycle are shown here.

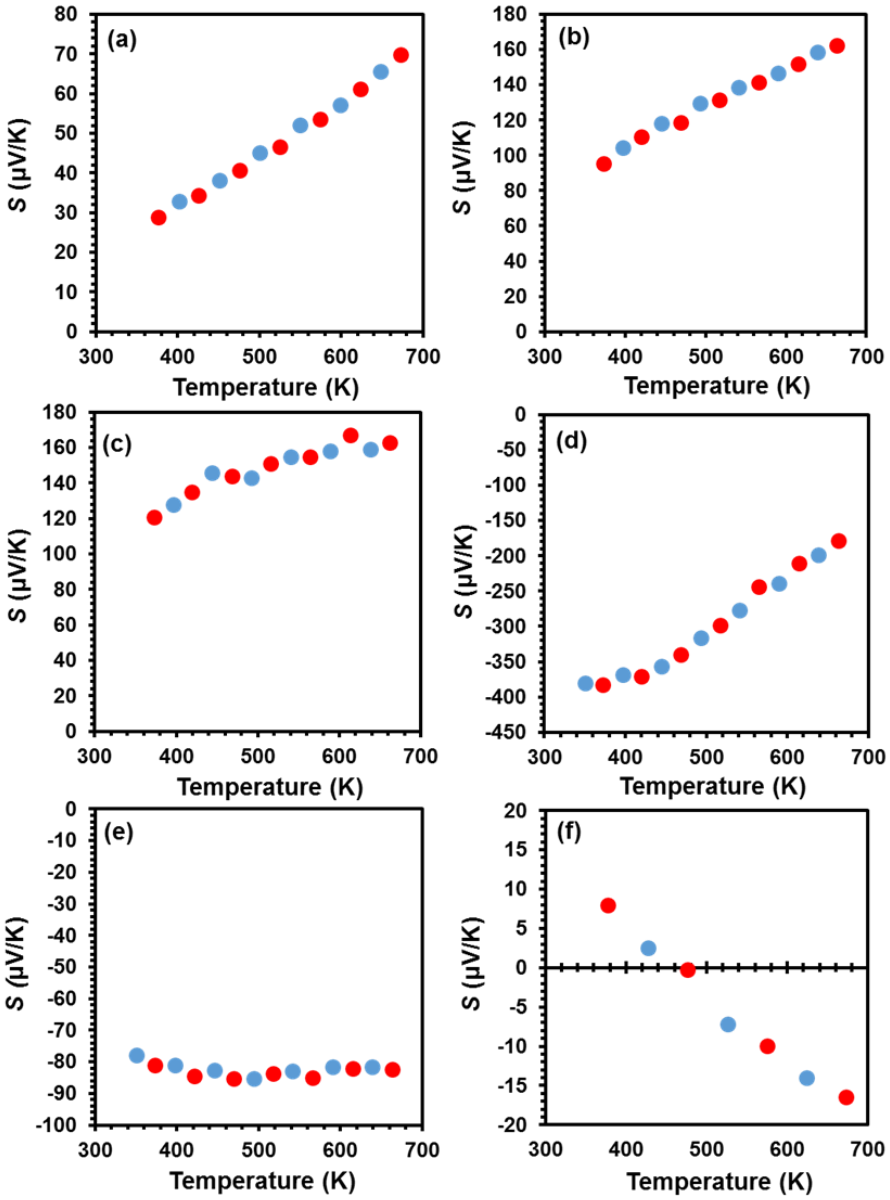

Figure 3.8. *S* of (a) Pellet_10/0, (b) Pellet_9/1, (c) Pellet_3/1, (d) Pellet_1/1, (e) Pellet_1/3 and (f) Pellet_0/10. Red and blue circles represent data measured in heating and cooling cycles, respectively.

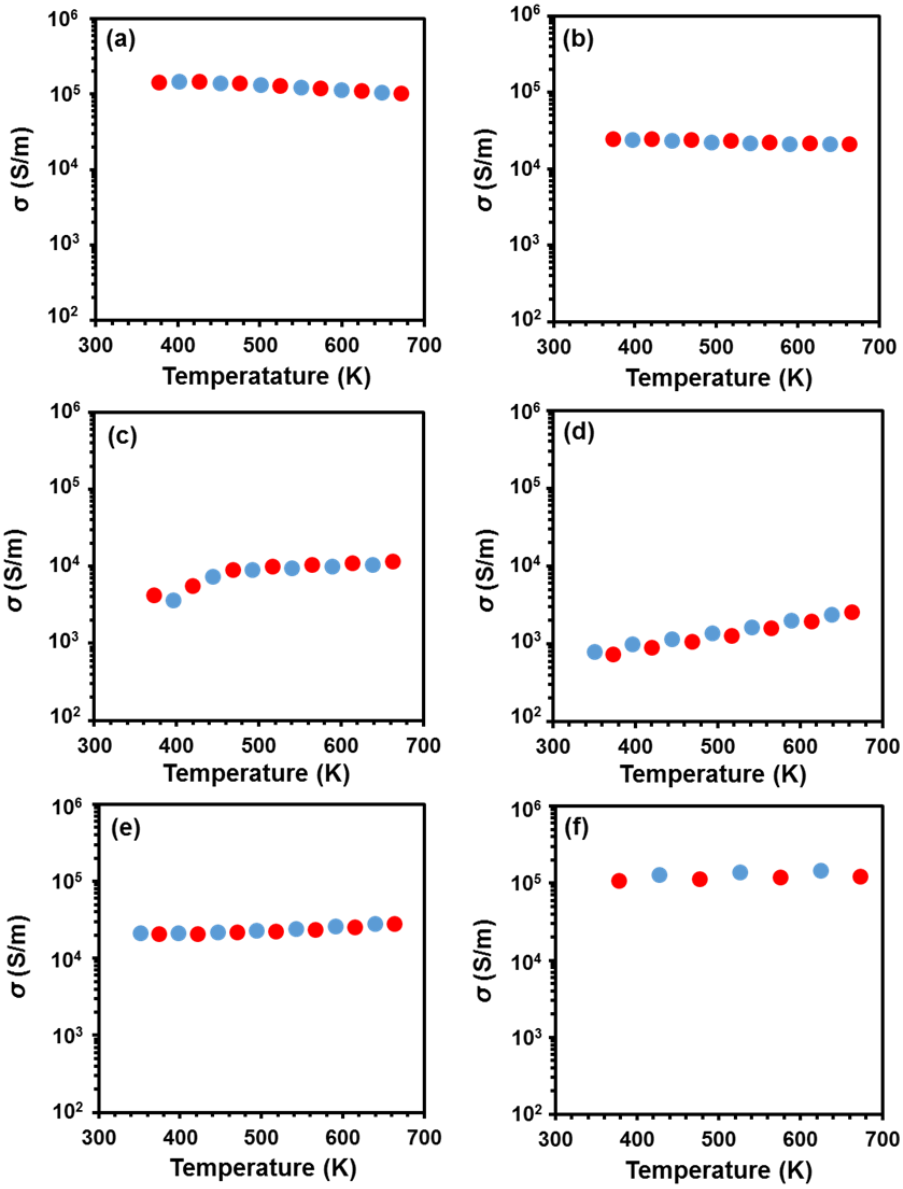

Figure 3.9. σ of (a) Pellet_10/0, (b) Pellet_9/1, (c) Pellet_3/1, (d) Pellet_1/1, (e) Pellet_1/3 and (f) Pellet_0/10. Red and blue circles represent data measured in heating and cooling cycles, respectively.

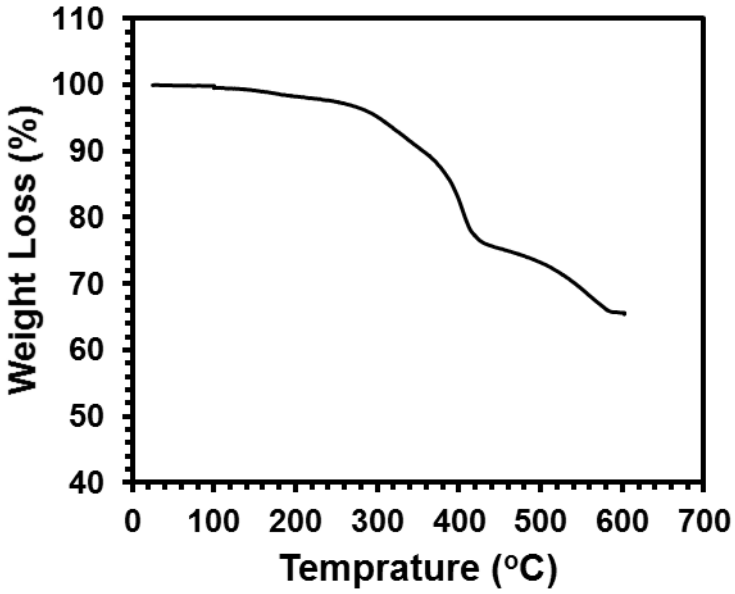

Figure 3.10. TGA of thiourea capped NPs.

The TE properties plotted as a function of the Cu atomic percentage in the pellets are shown in Figure 3.11. The thermoelectric properties drastically change by varying V_{Cu_2S}/V_{FeS}. Both p- and n-type nanostructured thermoelectric materials can be fabricated by just changing the V_{Cu_2S}/V_{FeS} ratio with the same starting materials and using the same synthesis process. In addition, we succeeded in significantly improving the *ZT* value of Pellet_9/1, in which *bn* and other copper sulfide phases coexist, compared with pristine *bn*, possibly because of the off-stoichiometric effect and/or the modulation doping effect. In future work, we will perform temperature-dependent Hall effect measurements in combination with high-resolution three-dimensional electron backscatter diffraction tomography to clarify the mechanism of the enhancement of the *ZT* value.

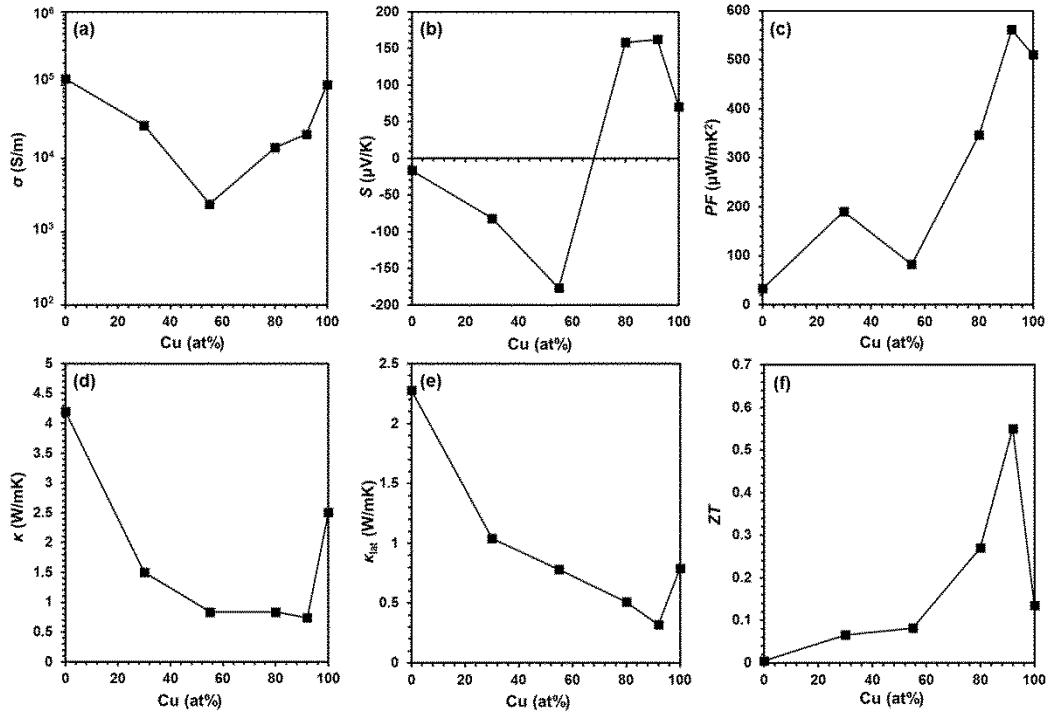

Figure 3.11. (a) σ, (b) S, (c) PF, (d) κ, (e) κ_{lat}, and (f) ZT plotted as a function of the Cu atomic percentage in the pellet. The values recorded at 663 K are plotted.

The TE properties of the nanostructured pelletized samples and bulk materials are compared with each other at 663 K as shown in Table 3.8 and 3.9. In case of Pellet_10/0, κ_{lat} values is lower than the bulk sample because of phonon scattering.

Table 3.8. Experimental values of σ, S, κ_{lat}, and ZT for all the samples at 663K.

Sample	σ (S/m)	S (μV/K)	κ_{lat} (W/mK)	ZT
Pellet_10/0	102039	70.00	0.8	0.13
Pellet_9/1	21317	162.00	0.3	0.55
Pellet_3/1	12266	163.00	0.5	0.27
Pellet_1/1	2611	-177.80	0.8	0.06
Pellet_1/3	28193	-82.25	1.0	0.08
Pellet_0/10	122002	-16.48	2.3	0.005

Table 3.9. Reference values of σ, S, κ_{lat}, and ZT for bulk materials at 663K.[43, 18, 12]

Bulk Material	σ (S/m)	S (μV/K)	κ_{lat} (W/mK)	ZT
$Cu_{1.8}S$	100000	70.00	1.5	0.12
Cu_5FeS_4	7500	200.00	0.3	0.38
$CuFeS_2$	4900	-350.00	1.5	0.18

3.7 Conclusions

The Cu–Fe–S system contains environmentally benign and abundant elements, and it potentially has good TE properties in a medium temperature range. However, the low figure of merit and the difficulty of producing Cu–Fe–S TE materials limit their practical applications. Therefore, it is imperative to develop rapid low-cost methods to fabricate high-performance Cu–Fe–S TE materials. In this study, we demonstrated a facile, rapid, and low-cost method for fabricating Cu–Fe–S TE materials based on colloid chemistry. In this method, chemically synthesized Cu_2S and FeS nanoparticles are mixed and then sintered by the PECS technique. During sintering, phase changes occur, resulting in multiphase nanocomposites. By varying the ratio of Cu_2S to FeS, the type of carrier (p- or n-type) can be readily controlled. In addition, the phonon scattering is dominated by defect scattering in the cases of blended samples. In particular, with a blending ratio of Cu_2S/FeS = 9/1, a nanocomposite mainly consisting of *bn* along with some minor phases is produced. It is known that *bn* is a promising TE material because of its intrinsic ultralow κ (0.3 W m^{-1} K^{-1}). However, the ZT value of stoichiometric *bn* has been reported to be about 0.38 (at 663 K) owing to its low PF. In the present study, the ZT value of *bn* is increased to 0.55 (at 663 K) by increasing the PF while maintaining ultralow κ.

References

(1) Zheng, X. F.; Liu, C. X.; Yan, Y. Y. A Review of Thermoelectric Research-Recent Developments and Potentials for Sustainable and Renewable Energy Applications. *Renew. Sustain. Energy Rev.* **2014**, *32*, 486-503.

(2) LeBlanc, S. Thermoelectric Generators: Linking Material Properties and Systems Engineering for Waste Heat Recovery Applications. *Sustain. Mater. Technol.* **2014**, *1–2*, 26-35.

(3) Ge, Z.-H.; Zhao, L.-D.; Wu, D.; Liu, X.; Zhang, B.-P.; Li, J.-F.; He, J. Low-Cost, Abundant Binary Sulfides as Promising Thermoelectric Materials. *Mater. Today* **2016**, *19*, 227-239.

(4) Girard, S. N.; He, J.; Zhou, X.; Shoemaker, D.; Jaworski, C. M.; Uher, C.; Dravid, V. P.; Heremans, J. P.; Kanatzidis, M. G. High Performance Na-Doped PbTe–PbS Thermoelectric Materials: Electronic Density of States Modification and Shape-Controlled Nanostructures. *J. Am. Chem. Soc.* **2011**, *133*, 16588-16597.

(5) Biswas, K.; He, J.; Blum, I. D.; Wu, C.-I.; Hogan, T. P.; Seidman, D. N.; Dravid, V. P.; Kanatzidis, M. G. High-Performance Bulk Thermoelectrics with All-Scale Hierarchical Architectures. *Nature* **2012**, *489*, 414-418.

(6) Ohta, M.; Biswas, K.; Lo, S.-H.; He, J.; Chung, D. Y.; Dravid, V. P.; Kanatzidis, M. G. Enhancement of Thermoelectric Figure of Merit by the Insertion of MgTe Nanostructures in p-type PbTe Doped with Na_2Te. *Adv. Energy Mater.* **2012**, *2*, 1117-1123.

(7) Zebarjadi, M.; Joshi, G.; Zhu, G.; Yu, B.; Minnich, A.; Lan, Y.; Wang, X.; Dresselhaus, M.; Ren, Z.; Chen, G. Power Factor Enhancement by Modulation Doping in Bulk Nanocomposites. *Nano Lett.* **2011**, *11*, 2225-2230.

(8) Pei, Y.-L.; Wu, H.; Wu, D.; Zheng, F.; He, J. High Thermoelectric Performance

Realized in a BiCuSeO System by Improving Carrier Mobility Through 3D Modulation Doping. *J. Am. Chem. Soc.* **2014**, *136*, 13902-13908.

(9) Zhou, W.; Dwivedi, P.; Shijimaya, C.; Ito, M.; Higashimine, K.; Nakada, T.; Takahashi, M.; Mott, D.; Miyata, M.; Ohta, M.; Miwa, H; Akatsuka, T; Maenosono, S. Enhancement of the Thermoelectric Figure of Merit in Blended $Cu_2Sn_{1-x}Zn_xS_3$ Nanobulk Materials. *ACS Appl. Nano Mater.* **2018**, *1*, 4819-4827.

(10) Singh, M.; Miyata, M.; Nishino, S.; Mott, D.; Koyano, M.; Maenosono, S. Chalcopyrite Nanoparticles as a Sustainable Thermoelectric Material. *Nanomaterials* **2015**, *5*, 1820-1830.

(11) Xie, H.; Su, X.; Yan, Y.; Liu, W.; Chen, L.; Fu, J.; Yang, J.; Uher, C.; Tang, X. Thermoelectric Performance of $CuFeS_{2+2x}$ Composites Prepared by Rapid Thermal Explosion. *NPG Asia Mater.* **2017**, *9*, e390.

(12) Li, Y.; Zhang, T.; Qin, Y.; Day, T.; Snyder, G. J.; Shi, X.; Chen, L. Thermoelectric Transport Properties of Diamond-Like $Cu_{1-x}Fe_{1+x}S_2$ Tetrahedral Compounds. *J. Appl. Phys.* **2014**, *116*, 203705.

(13) Xie, H.; Su, X.; Zheng, G.; Zhu, T.; Yin, K.; Yan, Y.; Uher, C.; Kanatzidis, M. G.; Tang, X. The Role of Zn in Chalcopyrite $CuFeS_2$: Enhanced Thermoelectric Properties of $Cu_{1-x}Zn_xFeS_2$ with In Situ Nanoprecipitates. *Adv. Energy Mater.* **2016**, *7*, 1601299.

(14) Tsujii, N.; Mori, T.; Isoda, Y. Phase Stability and Thermoelectric Properties of $CuFeS_2$-Based Magnetic Semiconductor. *J. Electron. Mater.* **2014**, *43*, 2371-2375.

(15) Barbier, T.; Berthebaud, D.; Frésard, R.; Lebedev, O. I.; Guilmeau, E.; Eyert, V.; Maignan, A. Structural and Thermoelectric Properties of n-Type Isocubanite $CuFe_2S_3$. *Inorg. Chem. Front.* **2017**, *4*, 424-432.

(16) Zhang, X.; Zhao, H.; Zhu, Y.; Yang, Y.; Jiang, D.; Chen, X.; Sun, J.; Luo, J.; Cai, B.; Fan, H. Facile Synthesis of Nano-Sized $CuFe_2S_3$: Morphology and Diverse Functional

Tuning and Crystal Growth Mechanism Exploring. *Regen. Biomater.* **2017**, *4*, 223–231.

(17) Lyubutin, I.; Lin, C.-R.; Starchikov, S.; Siao, Y.-J.; Tseng, Y. Synthesis, Structural and Electronic Properties of Monodispersed Self-Organized Single Crystalline Nanobricks of Isocubanite $CuFe_2S_3$. *J. Solid State Chem.* **2015**, *221*, 184-190.

(18) Qiu, P.; Zhang, T.; Qiu, Y.; Shi, X.; Chen, L. Sulfide Bornite Thermoelectric Material: A Natural Mineral with Ultralow Thermal Conductivity. *Energy Environ. Sci.* **2014**, *7*, 4000-4006.

(19) Long, S. O. J.; Powell, A. V; Vaqueiro, P.; Hull, S. High Thermoelectric Performance of Bornite Through Control of the Cu(II) Content and Vacancy Concentration. *Chem. Mater.* **2018**, *30*, 456-464.

(20) Zhang, A.; Shen, X.; Zhang, Z.; Lu, X.; Yao, W.; Dai, J.; Xie, D.; Guo, L.; Wang, G.; Zhou, X. Large-Scale Colloidal Synthesis of Cu_5FeS_4 Compounds and Their Application in Thermoelectrics. *J. Mater. Chem. C* **2017**, *5*, 301-308.

(21) Larsen, T. H.; Sigman, M.; Ghezelbash, A.; Doty, R. C.; Korgel, B. A. Solventless Synthesis of Monodisperse Cu_2S Nanorods, Nanodisks, and Nanoplatelets. *J. Am. Chem. Soc.* **2003**, *125*, 5638-5639.

(22) Shimose, H.; Singh, M.; Ahuja, D.; Zhao, W.; Shan, S.; Nishino, S.; Miyata, M.; Higashimine, K.; Mott, D.; Koyano, M.; Luo, J; Zhong, C. J.; Maenosono, S. Copper Sulfide–Zinc Sulfide Janus Nanoparticles and Their Seebeck Characteristics for Sustainable Thermoelectric Materials. *J. Phys. Chem. C* **2016**, *120*, 5869-5875.

(23) Tang, Y.-Q.; Ge, Z.-H.; Feng, J. Synthesis and Thermoelectric Properties of Copper Sulfides via Solution Phase Methods and Spark Plasma Sintering. *Crystals* **2017**, *7*, 141.

(24) Quintana-Ramirez, P. V.; Arenas-Arrocena, M. C.; Santos-Cruz, J.; Vega-González, M.; Martínez-Alvarez, O.; Castaño-Meneses, V. M.; Acosta-Torres, L. S.; de la Fuente-Hernández, J. Growth Evolution and Phase Transition from Chalcocite to Digenite in

Nanocrystalline Copper Sulfide: Morphological, Optical and Electrical Properties. *Beilstein J. Nanotechnol.* **2014**, *5*, 1542–1552.

(25) He, Y.; Day, T.; Zhang, T. S.; Liu, H. L.; Shi, X.; Chen, L. D.; Snyder, G. J. High Thermoelectric Performance in Non-Toxic Earth-Abundant Copper Sulfide. *Adv. Mater.* **2014**, *26*, 3974-3978.

(26) Rodríguez-Carvajal, J. Recent Advances in Magnetic Structure Determination by Neutron Powder Diffraction. *Physica B* **1993**, *192*, 55-69.

(27) Wu, C.-Y.; Pan, Z.-Q.; Liu, Z.; Wang, Y.-Y.; Liang, F.-X.; Yu, Y.-Q.; Wang, L.; Luo, L.-B. Controllable Synthesis of P-Type Cu_2S Nanowires for Self-Driven NIR Photodetector Application. *J. Nanoparticle Res.* **2017**, *19*, 35.

(28) Caldwell, A. H.; Ha, D. H.; Ding, X.; Robinson, R. D. Analytical Modelling of Localized Surface Plasmon Resonance in Heterostructure Copper Sulfide Nanocrystals. *J. Chem. Phys.* **2014**, *141*, 164125.

(29) Ge, Z.-H.; Zhang, B.-P.; Chen, Y.-X.; Yu, Z.-X.; Liu, Y.; Li, J.-F. Synthesis and Transport Property of $Cu_{1.8}S$ as a Promising Thermoelectric Compound. *Chem. Commun.* **2011**, *47* (47), 12697-12699.

(30) Tarachand; Hussain, S.; Lalla, N. P.; Kuo, Y.-K.; Lakhani, A.; Sathe, V. G.; Deshpande, U.; Okram, G. S. Thermoelectric Properties of Ag-Doped CuS Nanocomposites Synthesized by a Facile Polyol Method. *Phys. Chem. Chem. Phys.* **2018**, *20*, 5926-5935.

(31) Pearce, C. I.; Pattrick, R. A. D.; Vaughan, D. J. Electrical and Magnetic Properties of Sulfides. *Rev. Mineral. Geochemistry* **2006**, *61*, 127-180.

(32) Gosselin, J. R.; Townsend, M. G.; Tremblay, R. J. Electric Anomalies at the Phase Transition in FeS. *Solid State Commun.* **1976**, *19*, 799-803.

(33) Melnikov, A. A.; Tabachkova, N. Y.; Kichik, S. A.; Marakushev, I. S.; Koryakin, A. N.; Ponomarev, V. F. Influence of Temperature During Spark Plasma Sintering

Compaction of Melt-Spun *p*-$Bi_{0.5}Sb_{1.5}Te_3$. *J. Electron. Mater.* **2015**, *44*, 1517–1523.

(34) Yin, H.; Christensen, M.; Lock, N.; Iversen, B. B. Zn Migration During Spark Plasma Sintering of Thermoelectric Zn_4Sb_3. *Appl. Phys. Lett.* **2012**, *101*, 043901.

(35) Yin, H.; Blichfeld, A. B.; Christensen, M.; Iversen, B. B. Fast Direct Synthesis and Compaction of Homogenous Phase-Pure Thermoelectric Zn_4Sb_3. *ACS Appl. Mater. Interfaces* **2014**, *6*, 10542-10548.

(36) Wang, Z. D.; Yoshida, M.; George, B. Theoretical Study on the Thermal Decomposition of Thiourea. *Comput. Theor. Chem.* **2013**, *1017*, 91–98.

(37) Peng, Z.; Li, S.; Weng, M.; Zhang, M.; Xin, C.; Du, Z.; Zheng, J; Pan, F. First-Principles Study of Cu_9S_5: A Novel p-Type Conductive Semiconductor. *J. Phys. Chem. C* **2017,** *121*, 23317-23323.

(38) Okamoto, K.; Kawai, S. Electrical Conduction and Phase Transition of Copper Sulfides. *Jpn. J. Appl. Phys.* **1973**, *12*, 1130-1138.

(39) Yu, B.; Zebarjadi, M.; Wang, H; Lukas, K.; Wang, H.; Wang, D.; Opeil, C.; Dresselhaus, M.; Chen, G.; Ren, Z. Enhancement of Thermoelectric Properties by Modulation-Doping in Silicon Germanium Alloy Nanocomposite. *Nano Lett.* **2012**, *12*, 2077-2082.

(40) Parreira, P.; Lavareda, G.; Amaral, A.; Botelho do Rego, A. M.; Conde, O.; Valente, J.; Nunes, F.; Nunes de Carvalho, C. Transparent p-Type Cu_xS Thin Films. *J. Alloys Compd.* **2011**, *509*, 5099-5104.

(41) Sil, S.; Dey, A.; Datta, J.; Das, M.; Jana, R.; Halder, S.; Dhar, J.; Sanyal, D.; Ray, P. P. Analysis of Interfaces in Bornite (Cu_5FeS_4) Fabricated Schottky Diode Using Impedance Spectroscopy Method and its Photosensitive Behavior. *Mater. Res. Bull.* **2018**, *106*, 337-345.

(42) Peng, Z.; Li, S.; Weng, M.; Zhang, M.; Xin, C.; Du, Z.; Zheng, J. First-Principles Study

of Cu_9S_5: A Novel p-Type Conductive Semiconductor. *J. Phys. Chem. C.* **2017**, *121*, 23317-23323.

(43) Qiu, P.; Zhu, Y.; Qin, Y.; Shi, X.; Chen, L. Electrical and Thermal Transports of Binary Copper Sulfides Cu_xS with *x* from 1.8 to 1.96. *APL Mater.* **2016**, *4*, 104805.

Chapter 4: Relation between Structure and Thermoelectric Properties of Cu-Fe-S Thermoelectric Materials

4.1 Abstract

Cu-Fe-S system has been studied as TE material and their TE properties are dependent on the crystal phase of the system. This chapter provides an insight on TE properties of various Cu-Fe-S nanobulk materials fabricated in chapter 3 by mixing Cu_2S and FeS in different ratios and comparing with the reported Cu-Fe-S TE bulk materials on the basis of crystal phase of the Cu-Fe-S systems.

4.2 Relation between Structure and Thermoelectric Properties of Fabricated Pellets

4.2.1 Pellet_9/1 and Pellet_3/1

Pellet_9/1 and Pellet_3/1 are fabricated by mixing Cu_2S and FeS in liquid state in 90:10 and 75:25 (V/V) respectively, followed by densification using PECS and TE measurements. After TE measurements, intergrown nanopahases were observed in XRD as shown in Table 3.3. XRD was done for Pellet_9/1 which shows that *bn* was the main phase along with the intergrown phases such as *di*, *nu*, *ro*, and CuO. In case of Pellet_3/1, the *bn* as the main phase was observed along with intergrown phases *nu,* and *co.* These intergrown phases certainly affect the thermoelectric properties of the resulting material. The structural relation of TE properties of the Pellet_9/1 and Pellet_3/1 will be discussed.

Electrical Conductivity

Both the samples show semiconducting behavior. σ of Pellet_9/1 is much higher than the reported *bn*[1] material (5.0 S m^{-1} at 300 K) but can enhanced by tuning the off-stoichiometry because low thermal activation energy (E_a) values of *bn* (0.16 and 0.27 eV for low orthorhombic phase (at 300 K) and high cubic phase (at 620 K) as shown in Figure 4.1 suggests that σ can be easily tuned. It is reported that the σ of off-stoichiometric $Cu_{5.02}Fe_{0.98}S_4$ has 2-3 orders of higher σ than the stoichiometric *bn* (Cu_5FeS_4). It is because; Fe^{3+} valence state is higher than that of Cu^+ in *bn*.[2] Thus, off stoichiometric *bn* can generate more hole carriers (3.9×10^{19} cm^{-3} for $Cu_{5.02}Fe_{0.98}S_4$ at 300 K).[1] Another possible reason for enhanced σ to those reported for non-nanostructured stoichiometric *bn*, is modulation doping because of the presence of high charge carrier (*n*) phases such *di*, *nu* and, *ro*. It is possible that charge carriers diffuses from high *n* (4.5×10^{20} to 3.0×10^{21} cm^{-3} for *di*[3] and 3.3×10^{21} cm^{-3} for *ro*[4].) to low *n* (1.7×10^{16} cm^{-3}) in *bn*.[1] This diffusion occurs because of the fermi level imbalance between pristine *bn* and *di*. Fermi level lies in the valence band in case of *di* where as it lies in between in case of pristine *bn*. From the Hall measurement of Pellet_9/1, it was confirmed that the *n* (3.1×10^{21} cm^{-3}) is 5 orders higher than the pristine *bn* which is the possible case of modulation doping.

σ of Pellet_3/1 shows similar value to those of non-nanostructured non-stoichiometric ($Cu_{5.04}Fe_{0.96}S_4$) *bn*. it is probably because the volume fraction of *bn* is comparatively higher than in Pellet_9/1 as shown in Table 3.3 in the last chapter and there is possibility of slight non-stoichiometry. Comparison of σ of Pellet_9/1 and Pellet_3/1 with stoichiometric and non-stoichiometric *bn* is shown in Figure 4.2.

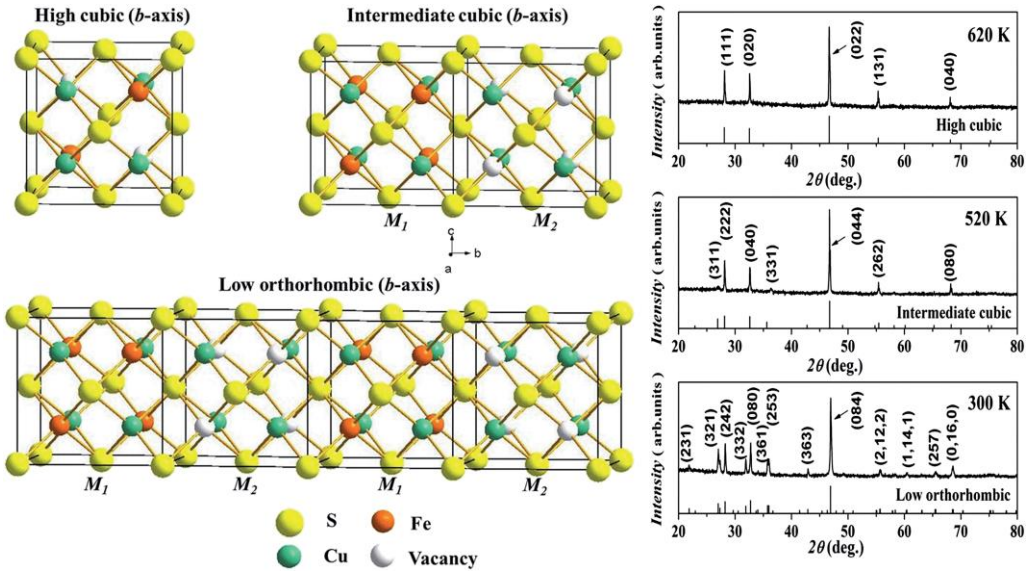

Figure 4.1 Crystal structures along the *b*-axis for the high cubic phase, intermediate cubic phase and, low orthorhombic phase and of *bn*. The XRD diffraction patterns of *bn* collected at 300, 520, and 620 K.[1]

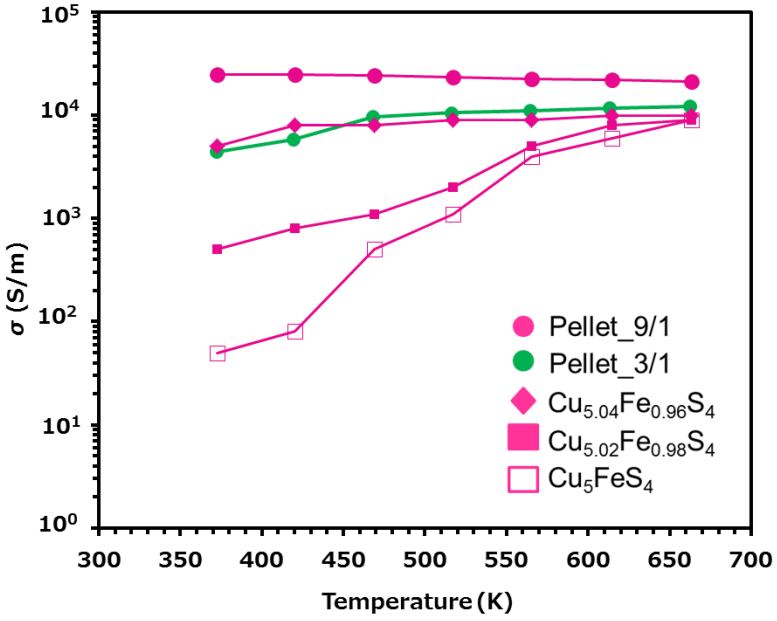

Figure 4.2 Comparison of σ of Pellet_9/1 and Pellet_3/1 with non-nanostructured stoichiometric and non-stoichiometric *bn*[1].

Seebeck Coefficient

The *S* value of Pellet_9/1 and Pellet_3/1 is nearly matching with the reported *S* value of pristine *bn* as shown Figure 4.3. Both the samples show p-type conducting behavior for all temperature range whereas pristine *bn* shows n-type semiconducting behavior at low temperatures and changes to p-type behavior above about 450 K.[1]

Both the pellets show p-type conductivity even below 450 K, this is probably because intergrown phases such as *di*, *nu* and, *ro* are p-type semiconducting materials.

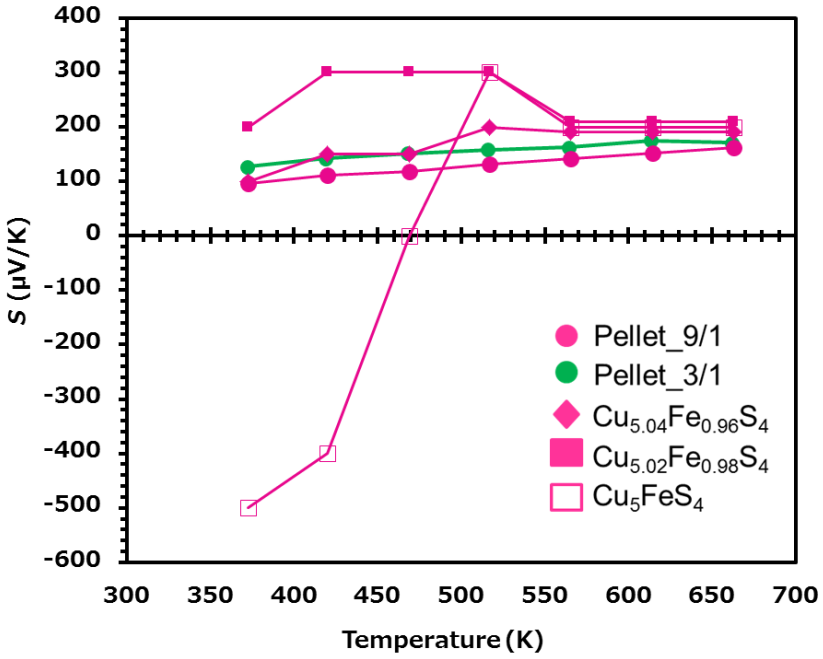

Figure 4.3 Comparison of *S* of Pellet_9/1 and Pellet_3/1 with non-nanostructured stoichiometric and non-stoichiometric *bn*[1].

Thermal Conductivity

It is reported that three *bn* samples *i.e.* one stoichiometric and two non-stoichiometric samples show abnormally ultra-low κ. Stoichiometric *bn* shows ultra- low κ_{lat} value of 0.2-0.4 W/mK[1] from 372-663 K and even in case of non-stoichiometric *bn* samples low κ_{lat} is maintained because of strain fluctuation between Cu and Fe in *bn* as shown in Figure 4.4.

Because of the highly disordered arrangement of Cu, Fe and vacancies in the high cubic phase of *bn* as shown in Figure 4.1, it disrupts the heat transfer by means of phonons and thus, responsible for low κ_{lat}. MFP in *bn* is 0.23 nm at 300 K which is very close to the shortest atomic distance between Cu/Fe and S atoms in *bn* of 0.2369 nm. This shows that κ_{lat} is close to the minimum κ for this *bn* material.[5] Thus, *bn* as the main phase in both Pellet_9/1 and Pellet_3/1 is responsible for the low κ_{lat} of both the samples as show in in Figure 4.4.

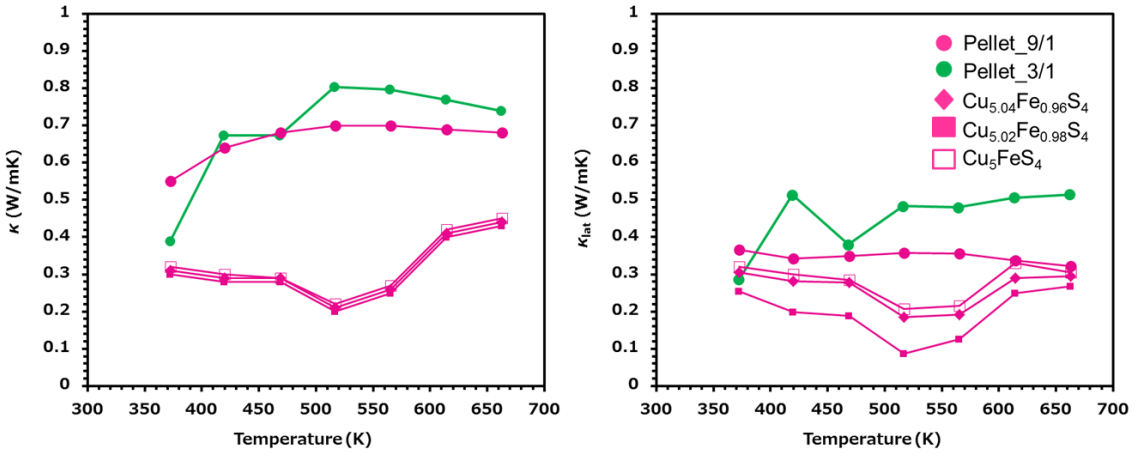

Figure 4.4 Comparison of κ and κ_{lat} of Pellet_9/1 and Pellet_3/1 with non-nanostructured stoichiometric and non-stoichiometric *bn*[1].

ZT

For Pellet_9/1 shows the highest *ZT* value of 0.55 at 663 K if compared to all the samples and is 45 % times higher than the reported non-nanostructured *bn* (*ZT* = 0.38 at 663 K),[1] as shown in Figure 4.5 even though the main phase is *bn* (Table 3.3). The reason for this high *ZT* value is the formation of Cu_5FeS_4 phase which has low thermal conductivity of 0.4 W/mK irrespective of its size along with high *PF*. Therefore, the nanostructuring does not lead to a further reduction of κ_{lat}.

ZT value in case of For Pellet_3/1, is slightly lower than the reported non-nanostructured *bn*, probably because the slightly high κ to those reported for non-nanostructured *bn*. Thus, slightly higher σ reduces the *ZT* in Pellet_3/1.

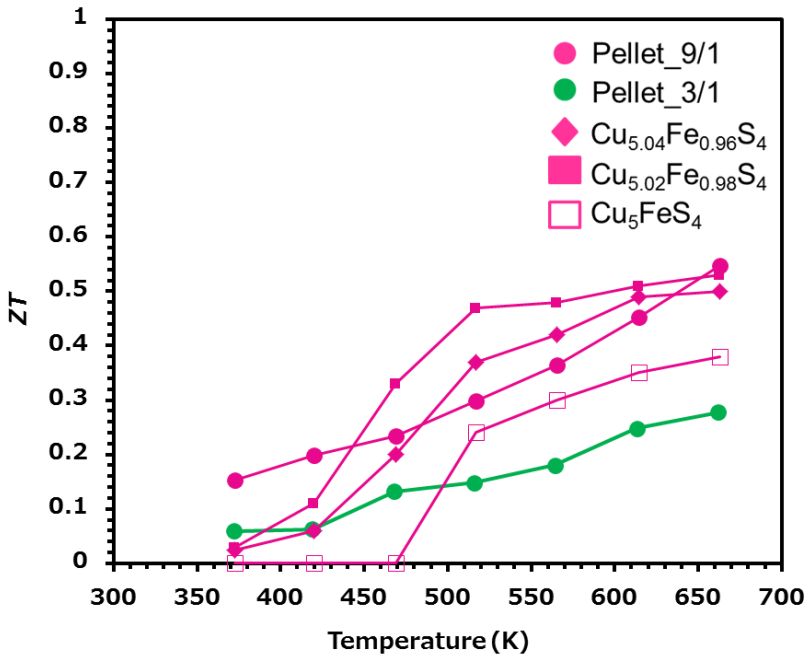

Figure 4.5 Comparison of *ZT* of Pellet_9/1 and Pellet_3/1 with non-nanostructured stoichiometric and non-stoichiometric *bn*[1].

4.2.2 Pellet_1/1 and Pellet_1/3

Pellet_1/1 and Pellet_1/3 are fabricated by mixing Cu_2S and FeS in liquid state in 50:50 and 25:75 (V/V) respectively, followed by densification using PECS and TE measurements. After TE measurements, intergrown nanopahases were observed in XRD as shown in Table 3.3. Both the pellets show *cp* as the main phase along with *bn* and *m-po* as the minor/secondary intergrown phases.

Electrical Conductivity

σ of Pellet_1/1 is compared with the non-nanostructured *cp* and it is lower than the reported value as shown in the Figure 4.6. It is because of the presence of another *bn* nano phase along with the main *cp* phase as shown in the Table 3.3 which may cause charge carrier scattering and thus, low electrical conductivity. Another possible reason for low σ is, decrease in charge carrier concentration in S deficient nanostructured *cp* materials.[6]

For Pellet_1/3, the σ is higher than the non-nanostructured *cp* because of the presence of *m-po* which has σ.

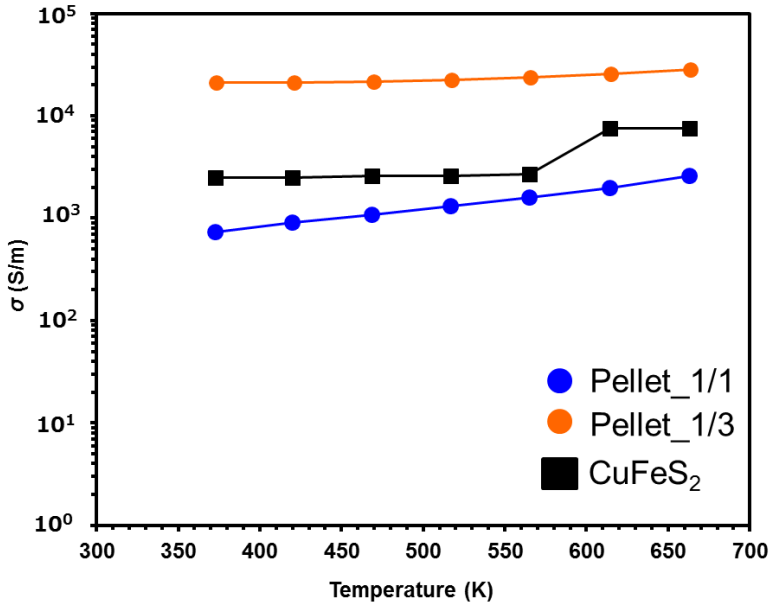

Figure 4.6 Comparison of σ of Pellet_1/1 and Pellet_1/3 with non-nanostructured *cp*[6].

Seebeck Coefficient

Presence of secondary phases affects the resulting *S* as well. In case of Pellet_1/1, the absolute *S* is lower than the reported non-nanostructured *cp*[6] because another phase *bn*

(secondary phase) has p-type conductivity and *cp* has n-type conductivity which reduces the overall *S* of the Pellet_1/1.

For Pellet_1/3, *S* is much lower than the the reported non-nanostructured *cp* because another phase *m-po* has *S* nearly zero. Thus, reducing overall *S* of the Pellet_1/3 as shown in Figure 4.7.

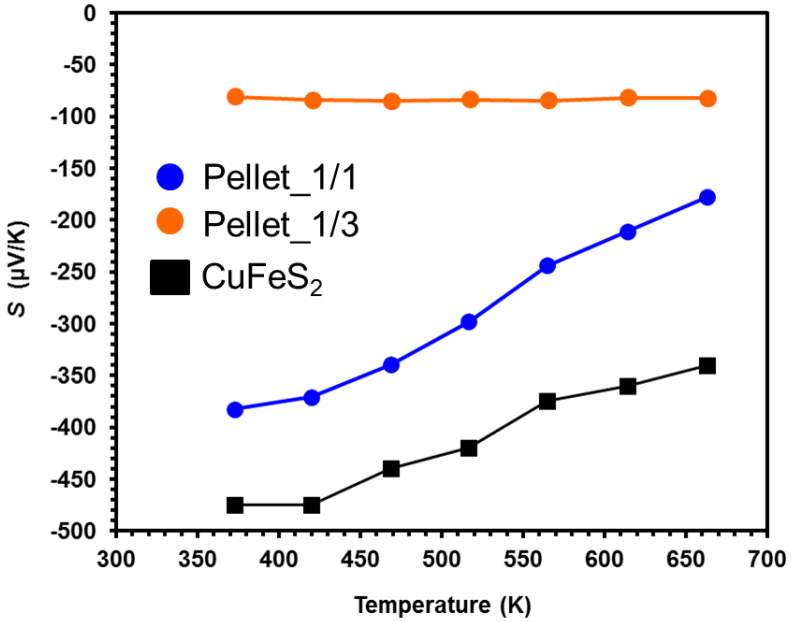

Figure 4.7 Comparison of *S* of Pellet_1/1 and Pellet_1/3 with non-nanostructured *cp*[6].

Thermal Conductivity

Both Pellet_1/1 and Pellet_1/3 show low κ as compared to those reported for non-nanostructured *cp*[6] as shown in Figure 4.8. Possible reason for low κ and κ_{lat} is presence of nanophases which causes effective phonon scattering. Another reason reported in the literature is that due to highly distorted structures at high temperatures due to strong Umklapp-scattering.[6]

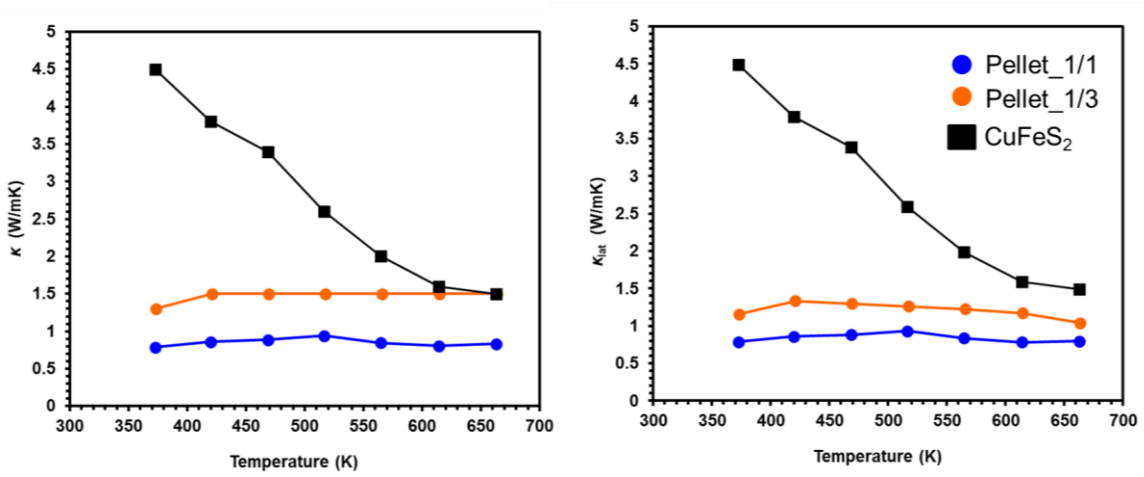

Figure 4.8 Comparison of κ and κ_{lat} of Pellet_1/1 and Pellet_1/3 with non-nanostructured *cp*[6].

ZT

The *ZT* plot of Pellet_1/1 and Pellet_1/3 at 663 K are shown in Figure 4.9, the calculated *ZT* value is 0.06 and 0.08 (at 663 K), respectively. These values are less than half of the *ZT* value of non-nanostructured *cp* (*ZT* = 0.18 at 663 K). [6] This is possibly because of the existence of another phase (*bn* or *m-po*) and/or nanostructuring decreasing not only κ_{lat} but also σ, resulting in lower PF.

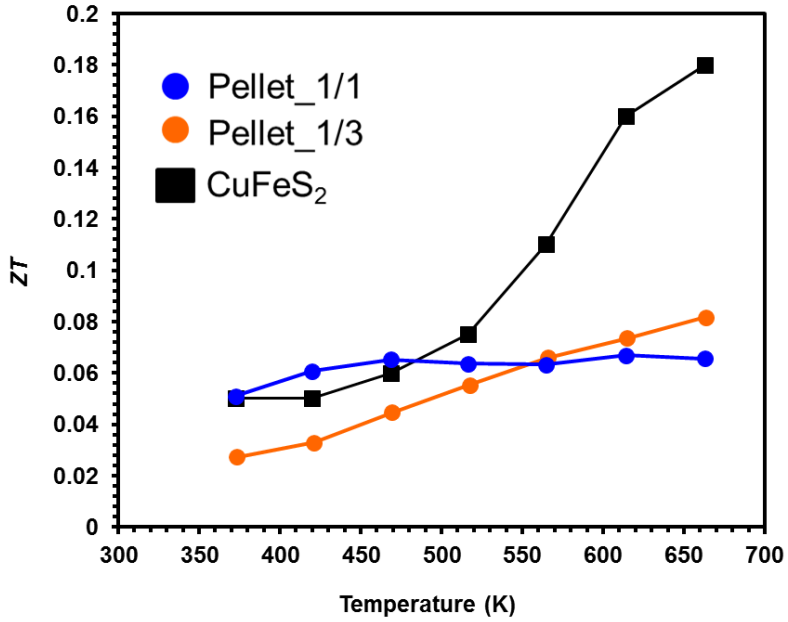

Figure 4.9 Comparison of *ZT* of Pellet_1/1 and Pellet_1/3 with non-nanostructured *cp*[6].

References

(1) Qiu, P.; Zhang, T.; Qiu, Y.; Shi, X.; Chen, L. Sulfide Bornite Thermoelectric Material: A Natural Mineral with Ultralow Thermal Conductivity. *Energy Environ. Sci.* **2014**, *7*, 4000-4006.

(2) Laan, G. van der; Pattrick, R. A. D.; Charnock, J. M. Grguric, B. A. Cu $L_{2,3}$ X-Ray Absorption and the Electronic Structure of Nonstoichiometric Cu_5FeS_4. *Phys. Rev. B: Condens. Matter Mater. Phys.* **2002**, *66*, 045104.

(3) Parreira, P.; Lavareda, G.; Amaral, A.; Botelho do Rego, A. M.; Conde, O.; Valente, J.; Nunes, F.; Nunes de Carvalho, C. Transparent p-Type Cu_xS Thin Films. *J. Alloys Compd.* **2011**, *509*, 5099-5104.

(4) Caldwell, A. H.; Ha, D. H.; Ding, X.; Robinson, R. D. Analytical Modelling of Localized Surface Plasmon Resonance in Heterostructure Copper Sulfide Nanocrystals. *J. Chem. Phys.* **2014**, *141*, 164125.

(5) Koto, K.; Morimoto, N. Superstructure Investigation of Bornite, Cu_5FeS_4, by the Modified Partial Patterson Function. *Acta Crystallogr., Sect. B: Struct. Crystallogr. Cryst. Chem.* **1975**, *31*, 2268.

(6) Li, Y.; Zhang, T.; Qin, Y.; Day, T.; Snyder, G. J.; Shi, X.; Chen, L. Thermoelectric Transport Properties of Diamond-Like $Cu_{1-x}Fe_{1+x}S_2$ Tetrahedral Compounds. *J. Appl. Phys.* **2014**, *116*, 203705.

Chapter 5: Conclusions and Future Prospects

5.1 Summary

In the final conclusions of this dissertation work entitled "Characterization of Sustainable Thermoelectric Materials Fabricated by using Chemically Synthesized Chalcopyrite NPs as Building Blocks" we fabricated sustainable TE nano material using wet chemical synthesis approach. Copper sulfide, iron sulfide, and Cu-Fe-S TE nanomaterials were fabricated using this synthetic technique as these materials are composed of earth abundant, less toxic and inexpensive elements which satisfies the objective of the material being sustainable.

This dissertation was outlined into five different chapters giving outlook about TE material and how sustainable materials are important for new class of TEs and how minimizing the dimensions of the materials can affect the TE properties of the material, detailed information for the experimental work and characterization techniques used in the analysis of Cu-Fe-S TE nanomaterial, detailed information for the one pot wet chemical synthesis of the Cu-Fe-S alloy TE material. Cu-Fe-S nanobulk system is fabricated using Cu_2S and FeS as building blocks.

In the beginning of this dissertation work, detailed introduction regarding the TE materials for energy harvesting was thoroughly discussed. Origin of the thermopower was briefly mentioned which eventually developed into the *ZT*. History of the state of the bulk material was also mentioned which achieved threshold *ZT* value by minimizing the dimensions of the material which has led in the enhancement of the *ZT* and materials with those values can be put into commercial purposes. But, being scarce in earth's crust, issues regarding toxicity and expensive are making these state of the art materials less sustainable for human use. An alternative to these materials need to be investigated soon. Chalcogenide and chalcopyrite type materials are now attracting more attention because of their sustainability (earth abundant, less toxic, and inexpensive). But these sustainable systems cannot match the efficiency of the state

of the art Bi_2Te_3, PbTe, SbTe TE material. Several approaches have been applied to the alternative materials to enhance the *ZT* value. One of the approaches is to minimizing the dimensions of the material into nano range using bottom-up/ wet chemical approach which opens the avenue for the easy formation of nanograins which can help scattering of phonons which eventually can reduce the lattice thermal conductivity and helps in enhancing the *ZT*. Nanostructuring in the system can be very promising in scattering heat carrying phonons and enhancing the *ZT*.

And my research objective in this dissertation clearly mentioned that sustainable Cu-Fe-S systems were fabricated using bottom up to gain better control, over size of the NPs which is useful in suppressing κ_L which hence can prove to be better in improving *ZT* and were characterized using various characterization techniques used are mentioned. Various characterization techniques that are used such as TEM, XRD, ICP-OES, STEM-HAADF and ZEM-3, LFA to measure the thermoelectric properties of the Cu-Fe-S systems (fabricated using bottom-up/ wet chemical approach).

In chapter 2 of this dissertation work, synthesis and characterization was reported for the sustainable chalcopyrite nanomaterial for the TE use at the low temperature. Various Cu-Fe-S system are synthesized using one pot bottom-up technique and XRD analysis for these samples shows that the NPs exhibit a phase transition from cubic to tetragonal as the amount of iron is increased in the particles. Compositional analysis shows that the particles contain a composition representative of the feeding ratio, proving that the particle composition can be reliably controlled. The straight forward pellet preparation is done using cold press method and further studies shows that the true nanoparticle size is retained in the TE materials. Finally, the room temperature *S* was measured for each sample. It was found that each sample is a P-type with a maximum value of 203 μV/K for the highest iron content. But due to difficulty in

controlling the shape, size and composition of the NPs new synthetic protocol for the fabrication of Cu-Fe-S system was designed.

Keeping the advantage of Cu-Fe-S system in mind and some challenges with controlling the shape, size and composition of the NP samples in case of chapter 2, Cu–Fe–S system is fabricated using environmentally benign and abundant elements (Cu_2S and FeS as building blocks) as a next attempt to fabricate Cu-Fe-S nanobulk TE material in chapter 3 and it potentially has good TE properties in a medium temperature range. However, the low *ZT* and the difficulty of producing Cu–Fe–S thermoelectric materials limit their practical applications. Therefore, it is imperative to develop rapid low-cost methods to fabricate high-performance Cu–Fe–S TE materials. In this study, we demonstrated a facile, rapid, and low-cost bottom-up method for fabricating Cu–Fe–S TE materials based on colloid chemistry. In this method, chemically synthesized Cu_2S and FeS NPs are mixed and then sintered by the PECS technique. During sintering, phase changes occur, resulting in multiphase nanocomposites. By varying the ratio of Cu_2S to FeS, the type of carrier (p- or n-type) can be readily controlled. In addition, the phonon scattering is dominated by defect scattering in the cases of blended samples. In particular, with a blending ratio of Cu_2S/FeS = 9/1, a nanocomposite mainly consisting of *bn* along with some minor phases is produced. It is known that *bn* is a promising TE material because of its intrinsic ultralow κ (0.3 W m^{-1} K^{-1}). However, the *ZT* value of stoichiometric *bn* has been reported to be about 0.38 (at 663 K) owing to its low PF. In the present study, the *ZT* value of *bn* is increased to 0.55 (at 663 K) by increasing the PF while maintaining ultralow κ.

In chapter 4, the structural relation of TE properties of different Cu-Fe-S system was discussed which leads us to more understanding of the TE behaviour of these system with the crystal structure.

In these above mentioned two chapters and from their conclusions it can be inferred that there is still enough room for the enhancements of *ZT* which will be discussed in the following future prospects section using the present results.

5.2 Future Prospects

My dissertation work is concluded with having the advantage of using Cu_2S and FeS nanomaterials as building blocks for the fabrication of Cu-Fe-S nanobulk TE system where p- to n-type conductivity can be varied just by changing the volume ratio of Cu_2S and FeS. There is lot more to explore in this particular research as maximum *ZT* value is still not optimized. In current research work maximum *ZT* of 0.55 at 663 K is achieved for 9:1 volume ratio of Cu_2S and FeS. In my future plan, I would like to take this research further by investigating other volume ratios of Cu_2S and FeS such as 9.5/0.5, 9.7/0.3 to obtain the optimized maximum *ZT* value. Though it is very challenging as the volume ratio reaches 100 % volume fraction (pure copper sulfide –$Cu_{1.8}S$) and *ZT* value seems to dip to 0.1 at 663 K.

It will be interesting to research further for n-type sustainable Cu-Fe-S nanobulk materials for future prospects because we know n-type sustainable TE materials are very rare. In the chapter 4 of this dissertation, we found that it is very easy to tune the p- to n-type conductivity just by changing the volume ratio of Cu_2S and FeS and n-type materials can be obtained by choosing the appropriate volume fraction of Cu_2S and FeS. Challenging thing will be optimizing the *ZT* value for these n-type material as *ZT* value for n-type Cu-Fe-S nanobulk material (0.06 at 663K for Pellet_1/1, and 0.08 at 663 K for Pellet_1/3) is less than the non-nanostructured n-type material, *cp* (0.18 at 663 K)[1], probably because of spontaneously intergrown phases along with *cp*. If the growth of spontaneously formed phases are controlled and PF can be enhanced by means of modulation doping, it will be possible to enhance the *ZT* value for these n-type TE materials.

References

(1) Li, Y.; Zhang, T.; Qin, Y.; Day, T.; Snyder, G. J.; Shi, X.; Chen, L. Thermoelectric Transport Properties of Diamond-like $Cu_{1-x}Fe_{1+x}S_2$ Tetrahedral Compounds. *J. Appl. Phys.* **2014**, *116*, 203705.